THESIS

ON QUASI-PERIODIC BAROCLINIC VARIABILITY IN THE EXTRATROPICAL CIRCULATION

Submitted by

Brian Crow

Department of Atmospheric Science

In partial fulfillment of the requirements

For the degree of Master of Science

Colorado State University

Fort Collins, Colorado

Fall 2016

Master's Committee:

Advisor: David W. J. Thompson

Elizabeth A. Barnes
Richard C. Aster

ABSTRACT

ON QUASI-PERIODIC BAROCLINIC VARIABILITY IN THE EXTRATROPICAL CIRCULATION

A number of recent studies have demonstrated that large-scale extratropical wave activity is characterized by quasi-periodic behavior on timescales of 20-30 days, particularly in the Southern Hemisphere. This phenomenon has been termed the Baroclinic Annular Mode (BAM), and is responsible for the modulation of eddy heat fluxes, eddy kinetic energy, and precipitation on large scales. However, the extent to which this periodic modulation is discernable or significant on smaller spatial scales had not yet been established.

Using data from the ECMWF Interim Reanalysis for the period 1979-2014, this study extensively examines the spatial structure of the BAM. Spectral analyses reveal the spatial limitations of the periodic behavior, while lag-correlation analyses reveal the patterns of propagation and development of anomalies that give rise to the observed periodicity. Periodic behavior is more robust in the Southern Hemisphere than in the Northern Hemisphere, but filtering out low wavenumbers from NH data helps clarify the BAM signal. Additionally, it is demonstrated that the BAM appears very differently in two relatively similar global climate models, suggesting further study is needed to determine how modern GCMs capture the BAM.

Supplementing our analyses of observed and modeled data is a simple two-way linear feedback model, which is utilized to demonstrate the principal mechanism underlying periodic behavior in the BAM. The model makes it apparent that the BAM can be modeled as a simple linear feedback between baroclinicity and eddy heat fluxes. The periodicity seen on larger scales is a product of differential advection rates affecting the development of spatially overlapping, out-of-phase anomalies. The large-scale nature of the periodic behavior, however, makes it difficult to draw conclusions about the potential utility of the BAM for weather analysts and forecasters, and the limitations of this study limit our ability to describe its role in the climate system. It is hoped that the research presented here will pave the way to future studies which may more thoroughly answer such questions.

ACKNOWLEDGEMENTS

I would like to begin my lengthy list of acknowledgements by thanking my advisor, Dr. David W. J. Thompson. His choice to accept me as a student in December of 2013 began my graduate school experience, and his guidance was instrumental in shaping the research that went into this thesis. The other members of my committee also deserve recognition for their participation in this process, and for the helpful comments they have already provided and will no doubt offer at my defense: Dr. Richard Aster of the Geoscience Department and Dr. Libby Barnes of Atmospheric Science. My appreciation also extends to those associated with the Climate Dynamics grant at the National Science Foundation, as funding from that program enabled the research that constitutes this thesis.

Additionally, I would like to recognize and thank the other professors of the Climate Dynamics group for their informative lectures, helpful conversations, and general support relevant to this thesis: Dr. Libby Barnes, Dr. Thomas Birner, and Dr. Eric Maloney. Various students in the group were also helpful with numerous coding and conceptual issues at one point or another during my time here, including Samantha Wills, Jingyuan Li, Marie McGraw, Nicholas Davis, Edward Charlesworth, Ying Li, Eliott Faust, and Chengji Liu. Other professors and fellow students at Colorado State University, too numerous to list exhaustively, also deserve my thanks for their roles in shared educational experiences and making positive contributions to my graduate school experience in general.

Of course, even reaching a program of higher education is not without its challenges. I would like to thank various undergraduate professors, in particular Dr. Patrick Market and Dr. Neil Fox of the University of Missouri, for enlightening and challenging me during

my time with them. I would also be remiss if I did not acknowledge the invaluable research experience I gained from two summers of internships at Hobart and William Smith Colleges under the tutelage of Dr. Neil Laird and Dr. Nicholas Metz. The projects I worked on with them prepared me well for the challenges of graduate-level research, and were likely significant contributions to my admission to this graduate program.

Finally, it is with sincere gratitude that I would like to thank my friends and family, past and present, for their roles in my growth and development. Various friends and family members over the years have offered me the support, encouragement, and inspiration which has brought me to this point. Clearly, no two individuals have done more for me than my parents, Timothy R. Crow and Cheryl A. Crow. Their constant love, support, open-mindedness, and thoughtful advice has brought me this far in life, and will continue to shape me for years to come.

TABLE OF CONTENTS

CHAPTER ONE

INTRODUCTION AND BACKGROUND

At the interface between weather and climate, there exists a temporal range of relative mystery. Weather is well characterized as the day-to-day variability in the state of the atmosphere at any given place and time, while climate describes the long-term mean state of the atmosphere, determined by geography and the energy balance of the Earth with outer space. In the broad temporal range of weekly to monthly timescales, however, descriptions of the atmosphere's behavior are somewhat more abstract, fully constrained by the conventions of neither weather nor climate. Such timescales are beyond the range of what can be explicitly forecast by the most advanced contemporary forecast models, and yet fall short of the seasonal timescales in which phenomena such as El Nino become useful predictive tools. Successful weekly to monthly forecasting has thus largely eluded meteorologists.

Often, descriptions of the atmospheric state on these timescales are encapsulated in indices that attempt to identify a specific pattern of winds, heights, or pressures. The annular modes, discussed at length later in this chapter, provide a convenient and widely recognizable example. While many of these indices are useful descriptive tools, the large majority of such patterns evolve in highly irregular, nonlinear ways and do not exhibit periodic behavior, limiting their usefulness as forecasting tools. A hypothetical pattern that does have demonstrably periodic behavior would be far more useful, as recognition of the current state of the pattern would be sufficient to identify how it will evolve over at least the next cycle. In this thesis, we will explore such a pattern in observations and model data and its implications for weather predictability and climate. This pattern is termed the baroclinic annular mode (BAM), and we will explore its properties and effects in both hemispheres.

This first chapter will introduce some core concepts important to understanding the aforementioned pattern; these concepts include the annular modes, characteristics of storm tracks (particularly in the Southern Hemisphere), and some basics on baroclinic wave packet dynamics. The second chapter will describe the data and methodology used in our analyses. Analysis of "observations" (really, reanalysis data; this will be discussed more thoroughly in Chapter 2) will be discussed in Chapter 3. The extent to which the periodic behavior associated with the BAM emerges in the Northern Hemisphere will be explored in Chapter 4. The ability of a handful of modern global climate models to simulate the BAM will be assessed in Chapter 5. The sixth chapter will discuss the construction and use of a simple linear model that attempts to model the observed periodic behavior. Finally, Chapter 7 will summarize and conclude this thesis, as well as offering some thoughts on the potential forecast implications and consequences for climate.

1.1 The Annular Modes

The annular modes, broadly defined, are quasi-zonally symmetric modes of weather and climate variability on week-to-week and longer time scales. The word "annular" in common language means ring-shaped; in this context, it refers to the ring-like (zonally symmetric) appearance of the pattern of spatial variability. These rather distinct patterns of variability were first recognized in some form or another by Rossby (1939), who identified an irregular north-south displacement of semi-permanent circulation features and the accompanying shift in the zonal winds. A number of closely related studies then followed in the 1940s, leading to the development of the "index cycle" by Namias (1950). Extensive research on such annular mode-like variability continued for the next several decades, particularly concerning such barotropic patterns as the North Atlantic Oscillation (NAO) and the Southern Hemisphere high-latitude mode. However, much more recent work (e.g., Thompson and Barnes 2014; Thompson and Woodworth 2014; Thompson and Li 2015) has defined and characterized a second class of annular modes: *baroclinic* annular modes. These two categories of annular modes, barotropic and baroclinic, have very different characteristics; these will be discussed at length in the following subsections.

1.1.1 Barotropic annular modes

Across the more than fifty years of study of the annular modes, there have been several different definitions and calculation methodologies employed in various studies. For simplicity and consistency, the definition presented in Thompson and Barnes (2014) will be utilized throughout this study. Their definition states that the barotropic annular modes can be calculated as the leading empirical orthogonal function (EOF) or principal component (PC) time series of zonal-mean kinetic energy ($[u^2]$; henceforth, zonal-mean quantities will be denoted by brackets). Barotropic annular modes are driven by variations in the eddy fluxes of momentum and are marked by vacillation of the jet stream about its climatological mean axis (e.g., Lorenz and Hartmann 2001; Thompson and Wallace 2000; Thompson and Barnes 2014). These types of analyses will be discussed more fully in Chapter 2. The following sub-sections will detail the identification of the "index cycle"

(1.1.1.1), the emergence of the annular mode school of thought in both hemispheres (1.1.1.2), how the annular modes project onto weather (1.1.1.3), and how the annular modes act as a mode of variability internal to the atmosphere (1.1.1.4).

1.1.1.1 The index cycle

As alluded to previously, there has been some intuition about the existence of modes of planetary-scale variability since Walker and Bliss (1932), who recognized correlations in sea-level pressure patterns over large regions of the North Atlantic basin (often termed "teleconnections"). Soon after, Rossby (1939) identified shifts in various semi-permanent sea level pressure features throughout the Northern Hemisphere (NH). Through the 1940s, this line of inquiry began to consider the associated variability in the zonal winds across the mid- and high-latitudes (Willett 1948). Rossby and Willett (1948) then consolidated contemporary knowledge of hemispheric-scale variability into a description of the evolution of the "index cycle," a term that they coined to refer to the phenomenon that is the spiritual predecessor to the annular mode.

A follow-up study offered a description of the shifting of the primary belts of westerlies that is at least in part consistent with our modern understanding of the annular modes (Namias 1950). The chosen metric for the index cycle at this time was mean zonal winds between 35°N and 55°N at 700 hPa in the western hemisphere (0° longitude west to 180°) between the months of November and March. "High index" events were identified by the presence of anomalously large westerlies in this band, and "low index" events were marked by periods of anomalously small westerlies. Namias (1950) even proposed some expected consequences for NH weather as a result of this index cycle, although observations ultimately did not bear out these speculations.

Three additional studies utilized slightly different methodologies for characterizing sea-level pressure and wind variability in the high latitudes, all essentially resembling what would come to be known as the North Atlantic Oscillation (Lorenz 1950; Gates 1950; Lorenz 1951). While a robust “annular” pattern had been identified by numerous studies at this point, there was yet little understanding of the underlying mechanisms. Some speculated that since seasonal pressure changes are driven by the annual cycle of insolation, the short-term and irregular pressure fluctuations of the index cycle may be related to irregularities in solar flux (Namias 1950; Lorenz 1951). While at least one study has since suggested that interannual variability in solar activity may have a small impact on the zonality of atmospheric flow (Georgieva et al. 2007), the general consensus is that solar forcing is a minor factor and often implicated as a convenient explanation when no other mechanism can be identified (Rind 2002). Further study has since concluded that the annular modes are a mode of variability internal to the atmosphere; that is, external forcings likely serve only to alter the amplitude of variability but are not the primary driver of variability (e.g., Wallace 2000). More sophisticated analyses employed by later studies would reveal that the index cycle concept was rather incomplete, and offered only a simplistic observational basis for what would evolve into the annular mode concept.

1.1.1.2 Emergence of annularity in both hemispheres

For decades, studies continued to identify scattered regional indices defined by various pressure, wind, and air temperature patterns correlated across continental scales, largely in the Northern Hemisphere. Kutzbach (1970) was among the first to utilize eigenvector analysis to demonstrate that there were in fact hemispheric-scale patterns of variability, albeit with considerable regional biases. Wallace and Gutzler (1981) utilized composite anomaly, correlation, and eigenvector analysis maps (Fig. 1.2) to demonstrate that NH sea-level pressure and geopotential height variability had four main modes consistent with several leading teleconnections (including the index cycle or annular mode). However, it was in the SH that recognition of a truly annular pattern of variability first emerged.

Prior to the late 1970s, there had been only a handful of studies of interannual variability in the SH, largely due to a prohibitive lack of observational records (both spatially and temporally). Trenberth (1979) was the first study to truly document the mean and range of variability for heights in the SH. Rodgers and van Loon (1982) applied the eigenvector analysis techniques of Kutzbach (1970) and Wallace and Gutzler (1981) to the SH and discovered a quasi-annular structure in eigenvector 1. This result is rather remarkable considering that the dataset they utilized consisted of just 28 stations scattered throughout the SH; it seems likely that the very limited spatial resolution of the dataset artificially produced some of the asymmetric features seen in their analysis. Despite limitations of data quality and coverage, a handful of other studies during the 1980s and early 1990s established the robust nature of the annular mode in the SH (e.g., Kidson 1988; Karoly 1990). It would still be another decade before annularity was recognized in the NH, however.

Throughout this same time period, many studies were conducted on NH teleconnection patterns, in particular the North Atlantic Oscillation (NAO). A simple definition of the NAO index is the sea-level pressure difference between Lisbon, Portugal (38°N) and Stykkisholmur, Iceland (65°N) (Hurrell 1995, 1996). Its significance lies in the robust patterns of precipitation and temperatures that are associated with it across much of the NH (see Hurrell et al. 2003, and references therein). Numerous studies from the 1970s through 1990s employed techniques such as EOF analysis, singular-value decomposition (SVD), and canonical correlation analysis (CCA) to identify NAO-like patterns of variability that included centers of action in other regions of the hemisphere (e.g., van Loon and Rogers 1978; Trenberth and Paolino 1981; Baldwin et al. 1994). Thompson and Wallace (1998) later proposed the "Arctic Oscillation" as the first description of truly annular variability in the NH (see also Thompson et al. 2003).

The transition to the "annular mode" school of thought in the NH occurred in part due to the recognition of a connection between tropospheric height and pressure patterns and the strength of the stratospheric vortex. The leading mode of variability in stratospheric geopotential height was realized to be a product of the strength of the winter vortex, with lower-tropospheric temperature fields fluctuating in association (Perlwitz and Graf 1995). Soon after, the connection between the first EOF of sea-level pressure the strength of the stratospheric vortex was established (Thompson and Wallace 1998).

Ultimately, it was argued in Thompson and Wallace (2000) that the NAO/Arctic Oscillation was really the Northern Annular Mode (NAM), analogous to the SH's SAM. They further demonstrated that the NAM interacts strongly with planetary waves to modulate the mean flow and vice-versa. Baldwin and Dunkerton (1999) illustrated the seasonal cycle in amplitude of the NAM and indicated its apparent lack of influence on the stratosphere during boreal summer. It was also demonstrated that during winter, stratospheric anomalies tend to lead changes in the AO/NAM index, most frequently associated with stratospheric warmings (Baldwin and Dunkerton 2001).

While the annular modes in both hemispheres are qualitatively similar and often mirror each other in approximate amplitude and spatial scale (Fig. 1.3), subtle contrasts have crucial consequences for each hemisphere's circulation. As an example, stratosphere-troposphere coupling is quite different across the hemispheres. Baldwin and Dunkerton (1999) demonstrated that stratospheric anomalies had a tendency to lead changes in the AO/NAM. The stratospheric anomalies frequently had their origins in sudden stratospheric warming events, which are primarily a NH phenomenon (Kruger et al. 2005). These results were therefore not considered applicable to the SH.

By far the most significant difference in annular mode behavior between the hemispheres is tied to seasonality. While the NAM becomes very low amplitude and ill-defined during boreal summer months, the Southern Annular Mode (SAM) retains its structure and significance throughout the austral summer (e.g., Hartmann and Lo 1998; Thompson and Wallace 2000; Hall and Visbeck 2002). Additionally, the NH sees a lengthier "active season" each year, in which the tropospheric and stratospheric circulations are closely coupled due to the penetration of planetary waves into the stratosphere (Thompson and Wallace 2000). The weaker NH stratospheric vortex is capable of being disrupted for a greater period of time every year (JFM) than its stronger SH counterpart, which is usually only disrupted during its spring breakdown (Nov). There are many consequences of this seasonal troposphere-stratosphere coupling, as mentioned previously, but chief among them is the modulation of variability. Geopotential heights and zonal winds in the middle and high latitudes reach their greatest variability during these active seasons in each hemisphere, and projections onto precipitation and surface temperatures can therefore be expected as well.

1.1.1.3 Projections onto weather

The strength of the stratospheric vortex can be implicated in tropospheric cold anomalies, at least throughout the NH (Thompson et al. 2002). Following periods of a weak or easterly stratospheric vortex, which can occur during the low index phase of the NAM, widespread cold anomalies tend to occur throughout the high and middle latitudes of the NH. Even more generally, however, surface air temperature in both hemispheres has projections onto the annular modes (Thompson and Wallace 2000; Codron 2005). Codron (2005) demonstrated that much of interior Antarctica experiences substantial cold surface temperature anomalies during high index phases of the SAM, with a ring of slightly warmer temperatures over surrounding ocean and Antarctic Peninsula. However, temperature and zonal wind anomalies associated with the annular modes display significant asymmetries in both hemispheres (e.g., Thompson and Wallace 2000; Codron 2005; Codron 2007).

In addition to affecting surface air temperature, fluctuations in the SAM can impact rainfall in the southern subtropics. Hendon et al. (2007) isolated high- and low-index days of the SAM and considered daily wind, rainfall, and temperature anomalies over Australia. Composites revealed seasonally-dependent patterns of rainfall anomalies. During austral spring (SON) and summer (DJF), anomalous low-level easterly winds associated with the positive phase of the SAM produced notably higher amounts of rainfall over the southeast portion of the country. However, these same regions experienced drier conditions in the high index phase during the winter (JJA), largely due to the contraction of the midlatitude storm track to higher latitudes. Temperature anomalies are, somewhat counter-intuitively, cooler over much of Australia during the high-index phase in the warm season. This is perhaps the opposite of what might be expected in the absence of rainfall, but occurs as a result of cloud cover and evaporative cooling suppressing daytime maximum temperatures. A related mechanism is thought to be in play over South America: pressure shifts associated with the SAM produce greater cloud cover over certain regions, which in turn produce cold temperature anomalies over parts of the continent (Laken and Pallé 2012).

One final noteworthy impact of the annular modes is modulation of total column ozone concentrations, with the high (low) index corresponding to decreased (increased) ozone over the polar regions. The ozone decrease in the high index mode is largely due to the colder stratospheric temperatures during these periods, which provide greater formation opportunities for polar stratospheric clouds, the chief source of ozone-destroying mixed-phase reactions (see Fig. 1.4; Thompson and Wallace 2000). This effect is enhanced in the SH, where the strength of the vortex leads to greater containment of the polar airmass and cold anomalies can be more intense.

Additionally, Thompson et al. (2011) reviewed contemporary literature on the simulated effects of the SH ozone hole on the atmosphere and found that the ozone hole signature looks remarkably like the high-index anomalies associated with the SAM. This congruence explains much of the positive trend in the SH since the 1980s and has led to a tendency towards the requisite zonal wind and temperature anomalies discussed previously. Interestingly, climate model projections indicate that the poleward jet shift that is expected as a result of greenhouse gases accumulating in our atmosphere may roughly be offset in the coming decades by an equatorward jet shift as a result of ozone recovery (Barnes et al. 2014). It is therefore conceivable that trends in the SAM may not be as substantial in the coming decades as they were in the recent past, and may in fact cease altogether.

1.1.1.4 Annular modes as modes of internal variability

While the previous sections clearly demonstrate the importance of the annular modes to large-scale atmospheric variability, there has been little discussion to this point of the underlying mechanisms that give rise to these phenomena. Mainly, the annular modes come about as a result of the deposition of momentum via anomalous eddy momentum fluxes (Robinson 1991; Limpasuvan and Hartmann 1999, 2000). Primitive equation model studies of the zonal index/SAM uncovered the importance of synoptic-scale eddy fluxes in the SH, modulated by the amount of drag included in the model (Robinson 1996).

More sophisticated modeling studies demonstrated the self-maintaining nature of the annular modes. The intensity of the eddy fluxes was found to vary in accordance with the phase of the annular modes, with the high-index state being correlated with increased poleward eddy heat flux in the NH (Limpasuvan and Hartmann 1999). This, in turn, affects the strength of the eddy feedback mechanism and is thus related to the persistence of the high-index phase. Additionally, Rossby wave propagation is modulated by the annular modes: the high-index phase is associated with a more poleward-shifted jet, leading to more equatorward refraction of Rossby waves. This, in turn, enhances the eddy momentum deposition at high latitudes, and “shields” Rossby waves from disrupting the stratospheric vortex (Limpasuvan and Hartmann 2000). It’s still not well understood what instigates transitions between phases of the annular mode, or what mechanisms determine the meridional scale and zonal variations in the annular modes (e.g., Thompson et al. 2003).

1.1.2 Baroclinic annular modes

The concept of a different type of annular variability was introduced by Thompson and Barnes (2014), and extensively described by Thompson and Woodworth (2014). They offer a concise definition of the Southern *baroclinic* annular mode (SBAM) and distinguish its properties from those of the traditional, barotropic annular modes. The SAM is defined in the familiar way: it is essentially characterized by a north-south vacillation of the jet stream, it dominates the variance in zonal-mean kinetic energy, is driven by variations in eddy fluxes of momentum, and has no discernable periodicity. The SBAM, in contrast, dominates the variance in eddy kinetic energy and is driven by variations in eddy fluxes of heat. Rather than representing a latitudinal shift in the storm track, it represents a hemisphere-wide “pulsing” of eddy kinetic energy with a distinct periodicity centered near 25 days (Thompson and Woodworth 2014). Periodic behavior is also clear in midlatitude means of eddy heat fluxes and precipitation, albeit leading the peak in EKE by approximately one day.

Not only is this periodicity consistent across multiple measures of midlatitude cyclone activity, it appears to be a robust consequence of atmospheric dynamics. Thompson and Barnes (2014) compared the ERA-Interim “observations” with daily output from the GFDL CM3 model and found a remarkable resemblance. Additionally, aquaplanet and dry dynamical core GCMs reproduced a periodic effect in the EKE and eddy heat flux fields as well. This study also utilized a simple stochastic model to explore the interplay between eddy heat fluxes and baroclinicity; this will be discussed more extensive in Chapter 6.

Two follow-up studies offered further characterization of the SBAM. Thompson and Woodworth (2014) describe the SBAM index, a standardized index of the first PC of SH EKE anomalies which essentially enumerates the state of the mean EKE anomaly across the SH midlatitudes. This index was compared to the SAM index (standardized PC1 of anomalous zonal-mean zonal wind) via lag-correlation and found to correlate at $r < 0.1$ for all lags between -30 and +30 days. This finding will be revisited in later chapters. The SBAM is related to variability in the amplitude of baroclinic waves, and therefore of eddy heat fluxes as well. It therefore follows that the positive polarity of the SBAM is associated with increased midlatitude temperature variance (Thompson and Woodworth 2014). While much of the southern midlatitudes are comprised of open ocean, there is some variability in the variance of EKE across portions of the hemisphere. The variance in EKE is somewhat higher from the tip of South America through the South Atlantic and Australia, whereas it reaches a relative minimum in the southeast Pacific.

It is also worth noting that the presence of two robust annular modes of variability, one baroclinic and one barotropic, is not unique to the SH: Thompson and Li (2015) discuss at length the characteristics of the NAM and NBAM. Due to the presence of more significant topography and additional land-sea asymmetries in the NH versus the SH, the NBAM is not quite as annular and explains a slightly lower fraction of the variance in EKE than its southern counterpart (Thompson and Li 2015). The NBAM is also characterized by starker regional contrasts, as the North Pacific and North Atlantic sectors are the dominant regions of EKE variability, with regions of relative minima over the continents. However, the fact that the NBAM is still quite annular suggests that there is some degree of continuity or teleconnectivity between the separate storm tracks (Thompson and Li 2015).

These baroclinic annular modes, as they have been termed, represent a major process by which energy is cycled through the atmosphere. As section 1.4 will discuss further, the focus of this study will be to further investigate the properties of baroclinic annular modes, specifically as they pertain to the Southern Hemisphere. Next, however, is a brief review of the literature on Southern Hemisphere storm tracks and wave propagation dynamics, both of which will be crucial to understanding how the SBAM operates.

1.2 Characteristics of the Southern Hemisphere Storm Track

Storm tracks are regions of comparatively high eddy activity, located in a handful of midlatitude locations across the globe. They are generally better defined in the NH than the SH, where land-sea contrasts along the east coasts of Asia and North America produce strong temperature gradients and therefore have large potential for generating baroclinic eddies. The SH lacks such major baroclinic zones, but rather has a large, quasi-symmetrical temperature gradient throughout most of the hemisphere, driven by the contrast between the extreme cold of Antarctica and the temperate midlatitude oceans. These hemispheric differences have been explored through numerous observational studies and a handful of modeling experiments. A discussion of some of the most prominent of these studies follows.

In an attempt to broadly characterize how eddy activity is maintained in a hypothetical storm track, Chang and Orlanski (1993) utilized a highly idealized model without topography or land-sea contrasts. Instead, they simply prescribe a zonally-symmetric baroclinic jet with a periodic barotropic heating perturbation introduced slightly downstream of the beginning of the jet. As expected, they found that baroclinicity is maximized on the far western end of the channel, as eddies mix out the temperature gradients further downstream. However, they also determined that eddies tend to develop in groups, with subsequent eddies developing more barotropically downstream from an initial baroclinic disturbance. These eddies would then propagate eastward in a coherent packet with a group velocity of about 35 m s^{-1}. Decay of a given disturbance predominantly occurs through ageostrophic fluxes downstream, which in turn give rise to other disturbances where they converge. Further discussion of downstream development may be found in section 1.3.3. The core finding is that although baroclinicity may be concentrated in relatively small regions, downstream development of subsequent disturbances means that eddy activity does not need to be localized.

Another modeling study, aptly titled “On the Existence of Storm-Tracks,” utilized a sigma-coordinate spectral model to examine the degree to which the NH Atlantic and Pacific storm tracks are self-maintained (Hoskins and Valdes 1990). The study essentially determined that while the direct thermal effect of eddies reduces the baroclinicity in these highly baroclinic regions, and thus reduces the storm track’s ability to self-maintain, this effect is dwarfed by rather substantial diabatic heating in these regions. The diabatic heating acts to restore baroclinicity, thus enabling these storm track regions to exist in perpetuity. However, the authors note, the lack of midlatitude land-sea contrast throughout vast portions of the SH mean that its “extended but less definite storm-track” may in fact be maintained through another unspecified mechanism.

Despite the relative lack of large population centers in proximity to the SH storm track, characterizing storm behavior in the SH midlatitudes has been a topic of study for a number of years. As noted by Lee and Held (1993), the SH presents an opportunity to "study the development and organization of baroclinic eddies without the complexity introduced by the large planetary waves and localized storm tracks of the Northern Hemisphere (NH)." Thus, the SH midlatitudes represent a convenient testing grounds for new ideas about baroclinic wave growth, propagation, and decay. This concept will be explored extensively throughout this thesis.

Perhaps the most definitive climatological study of the SH storm tracks was conducted by Trenberth (1991). Using ECMWF analysis products over the period 1979-1989, the paper presents global statistics on the mean, variance, and standard deviation of a number of relevant meteorological variables, including u and v winds, vertical motion, temperature, moisture mixing ratio, and vorticity. While it was found that the SH storm track remained close to 50°S throughout much of the year, the latitude of peak variance was different for each variable. However, this variety of latitudes (illustrated in Fig. 1.6) can be explained by geostrophic principles and perturbation analysis of a typical baroclinic wave (Trenberth 1991). Owing to the lack of major midlatitude landmasses, the mean meridional temperature gradient is strong throughout the year, leading to a relatively zonally symmetric storm track that lacks robust seasonality.

Further evidence of the potential for a high degree of zonal symmetry in the SH storm track was presented by Randel and Stanford (1985b). Their study selected a single two-week period in which the SH tropospheric flow exhibited both a high degree of wave activity and a high degree of zonal symmetry. One of their main findings was that the stark contrast between the localized baroclinic wave activity of the NH and the hemisphere-wide activity in the SH may be indicative of "fundamentally different atmospheric behavior" between the hemispheres. The degree to which baroclinic wave activity actually does differ on large scales will be explored in greater depth later in this thesis.

While the idea that the SH storm track is continuous and largely zonally symmetric is true to first order, there are notable exceptions. First, most measures of the storm track indicate that it is strongest and most persistent in the southern Indian Ocean, in the longitudes between South Africa and Australia (Trenberth 1991). Additionally, there is a tendency for the jet to split, particularly in the wintertime, over the South Pacific Ocean to the east of New Zealand. This has been noted in multiple studies (e.g., Chang 1999; Trenberth 1991) and is largely a product of weak baroclinicity in the region enabling persistent blocking and standing ridges during austral winter.

Other studies have examined the presence of wave packets, rather than individual baroclinic waves, in the storm track regions. One such study focused primarily upon SH summer (DJF), the season in which wave packets were found to be most coherent (Chang 1999). Although seemingly counterintuitive, they demonstrated using a simple two-layer quasi-geostrophic (QG) model that wave packets actually become *more* coherent in time as the meridional temperature gradient decreases. This explanation appears to be at odds with the results of Trenberth (1991), but three other factors also contribute to increased coherence in summertime: (1) individual eddies tend to be physically larger during winter months, resulting in a smaller difference in scale between and individual eddy and the wave packet, (2) stationary waves have a stronger presence in winter months, obscuring and muting the propagation of wave packets about the hemisphere, and (3) the storm track is much more latitudinally confined in the summer months, making wave packet identification somewhat easier (Lee and Held 1993). The behavior and coherence of these Rossby wave packets is discussed in Section 1.3.

1.3 Dynamics of Wave Packets

As the previous sections have alluded to, the role of the annular modes in the atmosphere can be viewed as modulating the latitudinal range and strength of baroclinic eddies. In order to consider how the SBAM modulates the cycling of kinetic energy through eddies in the SH, it is also necessary to understand the hemispheric eddy kinetic energy budget. That topic will be addressed in section 1.3.1. In section 1.3.2, the interaction of Rossby wave packets with the mean flow and the state of the annular modes will be discussed. Section 1.3.3 will review literature on downstream development of atmospheric waves, particularly as it pertains to the SH storm track.

1.3.1 The eddy kinetic energy budget

One concept that will be explored more thoroughly during the model experiment conducted later in this thesis will be that of the eddy kinetic energy budget. Eddy kinetic energy is defined as follows:

$$(1.1)\ \ EKE_{point} = \frac{1}{2}(u^{*2} + v^{*2})$$

and

$$(1.2)\ \ EKE_{zm} = \frac{1}{2}[u^{*2} + v^{*2}]$$

where * denotes the difference from the zonal mean and [ ] indicate a zonal-mean quantity. Many of the analyses presented in Chapter 3 will be based upon EKE_{zm}; spectral analyses and regressions alike will consider EKE_{zm} averaged across the midlatitudes. For the purposes of this discussion, however, we will primarily be considering the EKE equation at a single gridpoint.

The eddy kinetic energy budget that will be considered in this section was derived by Orlanski and Katzfey (1991) in a study that analyzed the energetics of a particularly strong wave train originating over the southeast Pacific Ocean in September of 1987. As they noted, development of a complete EKE budget first requires the derivation of a complete set of energy equations that include contributions from the time-mean flow, the "first-order kinetic energy time fluctuation," and the eddy kinetic energy. This is accomplished by breaking down velocity and geopotential fields into time-mean and perturbation components, resulting in an equation of kinetic energy per unit mass that looks like the following:

$$(1.3)\ \ K = \frac{1}{2}(V_m \cdot V_m) + V_m \cdot v + \frac{1}{2} v \cdot v = \ K_m + K_1 + K_e$$

where *m* denotes a time-mean quantity, small *v* indicates a perturbation velocity value, *1* denotes the first-order time deviation, and *e* indicates an eddy quantity. While this equation is but many of the full set of energy equations they present, its inclusion here is intended to illustrate the partitioning of kinetic energy between time mean, deviations from the mean, and the eddy component of kinetic energy. The rest of the system of equations will be excluded from this summary in the interest of brevity.

Equations are derived for each of the three terms on the right hand side (RHS) of the previous equation; however, for our purposes, the most important equation is that describing the breakdown of K_e, or eddy kinetic energy:

$$(1.4)\quad \frac{\partial K_e}{\partial t} + V_m \cdot K_e + v \cdot \nabla_3 K_e$$

$$= -(v \cdot \nabla\phi) - \big(v \cdot (v \cdot \nabla_3 V_m)\big) + \big(v \cdot \overline{(v \cdot \nabla_3 v)}\big) - diss_e + v \cdot F_0$$

The terms on the left hand side (LHS) of the equation describe means by which the total EKE at a point location can change: the local time-tendency, advection by the mean flow, and three-dimensional advection by the eddies, respectively. The terms on the RHS describe the mechanisms by which these energy transformations can occur. The first RHS term is an eddy pressure-work term, which enumerates the EKE generated by cross-gradient (or ageostrophic) advection of geopotential. The second term represents energy conversion via Reynolds stresses, or approximately a conversion between mean flow kinetic energy and EKE. Term three is effectively the opposite, describing the conversion of EKE into mean flow kinetic energy. The fourth term, or $diss_e$, represents dissipation of EKE within the eddies due to internal friction. The final term can be described most simply as the effects of stationary wave forcing onto transient eddies. Over the long term, this term averages out to zero, but is usually of negligible magnitude even on shorter timescales. A similar EKE equation from a later study described the analogs to terms two and three as the barotropic conversion between EKE and mean flow kinetic energy, and a term similar to the final RHS term as representing baroclinic conversion of eddy potential energy into EKE (Chang and Orlanski 1993). Despite differences in their precise formulation, such an interpretation of the EKE budget may be considered accurate enough and convenient for our purposes.

It should be clear by now that the generation and dissipation of EKE can take numerous forms. Additionally, each means of energy transformation was of differing importance at different atmospheric scales. At a given point, the advection terms dominate the kinetic energy tendencies; however, the advection terms essentially cancel each other out when integrated over a region containing the entire disturbance (Orlanski and Katzfey 1991). Over regional scales or in the zonal mean, the primary source and sink terms are expected to be terms two, three, and four of the RHS. These energy transformations will be relevant for the analyses of EKE anomalies presented in Chapters 3 and 4. Downstream development is also a concept of central importance to our analyses, and is discussed at length in the next section.

1.3.2 Downstream development

The discussion of storm track characteristics in Section 1.2 was replete with references to propagating wave packets, modulation of which are among the central characteristics of the BAM. Wave packets themselves, however, are the result of the rippling of energy from an initial disturbance. While linear wave theory suggests that initially localized disturbances in an unstable medium will spread out both upstream and downstream, nonlinearities modify this process substantially (e.g., Lee and Held 1993; Chang and Yu 1999). Nonlinearities tend to force development of a more localized series of downstream disturbances, while the upstream-moving waves tend to dissipate fairly rapidly. Although nonlinear processes need to be considered to properly understand wave development patterns and characteristics, the downstream edge of observed wave packets tends to follow the propagation rate predicted by linear wave theory. Differentiating between linear and nonlinear wave processes for the purposes of understanding downstream development has been a focus of numerous studies in recent decades.

Using the same model as in Simmons and Hoskins (1978), Simmons and Hoskins (1979) were among the first to characterize downstream development of baroclinic waves in the atmosphere. They placed a localized vorticity perturbation in a simple zonal-mean flow and found that while the vorticity moved downstream and amplified, small-amplitude disturbances continued to grow upstream in the vicinity of the initial disturbance. This finding was somewhat surprising in that synoptic meteorologists at the time had very little understanding of *upstream* development as opposed to downstream. However, they also developed an important understanding of the properties of downstream developing waves. Among these properties are the tendency for waves to be zonally longer, higher amplitude, and quicker to peak in amplitude in the upper troposphere than at the surface. The peaking of wave amplitudes aloft prior to at the surface was suggestive of a downstream dispersion of energy, a finding which was supported by later studies (e.g., Chang 1993).

Although downstream development was recognizable in such idealized models, it was only after Chang (1993) that the realization emerged that downstream development is pervasive in the real atmosphere as well. By not time-filtering meridional wind data as was done in previous studies, Chang (1993) demonstrated that wave packets preferentially originate over regions of strong baroclinicity (the storm tracks in the NH; see Fig. 1.7), but grow downstream through ageostrophic fluxes from upstream. That is, regions of high baroclinicity generate waves through conversion of baroclinic energy to eddy kinetic energy, then decay via ageostrophic radiation of energy downstream (Fig. 1.8). Waves from outside strongly baroclinic regions generally grow due to convergence of ageostrophic fluxes from waves upstream, and decay through ageostrophic fluxes and dissipation. This finding confirmed that downstream development is ubiquitous in the real atmosphere, but left many questions about which factors determine the distance downstream that development can occur.

Chang (1993) also discovered, via analysis of an eddy-kinetic energy budget based upon Orlanski and Katzfey (1991), that the properties of individual waves within a downstream-developing wave train vary depending upon their location. If a "reference disturbance" is taken to be the baroclinic wave nearest to the baroclinic region or storm track (i.e., in the western Pacific over the Kuroshio current), the nature of each wave in a wave train can be described in terms of their baroclinicity. It was found that the reference or origin disturbance had the greatest westward tilt with height and eastward tilt in temperatures, indicative of a high degree of baroclinicity; tilt with height decreased with each successive downstream wave, indicating increasingly barotropic waves downstream. In fact, waves in weakly baroclinic regions (i.e., northeastern Pacific basin) may never reach a point in which baroclinic conversion is an important source term in the eddy kinetic energy budget; instead, they rely almost entirely upon ageostrophic fluxes from upstream for development. It should be noted that this study focused entirely on the NH, and primarily on the Pacific basin. However, results from Lee and Held (1993) suggest that similar asymmetries exist in SH wave packets, as they found that wave breaking was favored on the western (upstream) periphery of a wave packet whilst the greatest baroclinic growth was observed on the eastern (downstream) periphery. Taken together, the two studies suggest a well-established asymmetry of growth and decay across a coherently propagating wave packet.

Objective tracking of wave packets in the north Pacific was conducted in another study focusing on how wave train properties varied throughout the NH winter. Utilizing one-point correlations and regressions of 300 hPa v', propagation of wave packets across the north Pacific can be seen readily (Chang and Yu 1999). There exist latitudinal gradients in wavelength and wavenumber, but the midlatitudes are typically characterized by wavenumber 6-8 in the NH with a dominant period of 4-8 days. These waves have a typical phase speed of 12 m s^{-1} and group velocities of 25-30 m s^{-1}. This can vary between land and ocean, however: over land, zonal phase speeds are slightly faster than u_{700}, and over ocean, zonal phase speeds are slightly slower. This implies a lower “steering level” flow over the oceans as opposed to land. A decorrelation time scale was also defined to compare the lifetime of wave packets with individual wave phases. It was found that wave packets remain coherent for longer than individual waves. Such results provide useful context for comparison to the SH, but again with the caveat that such strong longitudinal gradients in baroclinicity are not present in the southern midlatitudes. It is expected that wave coherence will be at least as great in the SH, but with potentially different wavenumbers and periodicity.

In a continuation of the work from Chang and Yu (1999), Chang (1999) addressed hemispheric and seasonal contrasts in wave packet behavior. As mentioned in section 1.2, the SH storm track does not have the same degree of regional variability that is present in the NH. Rather, the SH storm track is largely continuous, but “spirals” in towards the pole, with its most equatorward position occurring in the southeast Pacific and its most poleward in the south-central Pacific. The SH also shows far less seasonality than the NH in a number of ways, chiefly in dominant wavenumber and wave coherence. Additional model experiments were conducted using the Geophysical Fluid Dynamics Laboratory (GFDL) GCM to determine which factors affect wave coherence. In agreement with Lee and Held (1993), it was found that wave packet coherence is greater in less baroclinic environments. However, Chang (1999) failed to find substantial seasonal differences in wave coherence between austral winter and summer. This could be partially due to the results obtained from a solstitial experiment, in which the position of the thermal equator was moved to simulate uneven heating across the hemispheres. While the implications of moving the latitude of maximum heating were unclear, it seems likely that the effects from moving the thermal equator are of similar magnitude and opposite sign to adjusting the strength of the Hadley cell. The strength of the Hadley circulation was adjusted by making sizable heating and cooling adjustments; these results suggest that a stronger Hadley circulation leads to increased wave packet coherence (Chang 1999).

The significance of downstream development to the SBAM is primarily that the SBAM is characterized by the development and propagation of anomalous wave packets through the SH midlatitudes. Evidence will be presented later in this thesis for the dependence of the quasi-periodic signal upon downstream development and conversion of baroclinic energy to eddy kinetic energy. The implications of these mechanisms for the behavior of wave packets will be discussed further at numerous other points throughout this study.

1.4 Study Objectives

While the characteristics of barotropic annular modes have been extensively studied, comparatively little is understood about the baroclinic annular modes and the implications they may have for weather and climate. This study focuses on the baroclinic annular mode of the SH (SBAM) because the SH is a simpler system than the NH, both geographically and dynamically. By understanding the behavior and causal mechanisms of the SBAM, it seems logical that analogous behavior and mechanisms can then be explored in the NH (NBAM), even if these signals appear weaker relative to the background noise. Given the profound implications of the barotropic annular modes for the global circulation, weather patterns, and even ozone concentrations, there is a reasonable expectation that the SBAM has similarly critical implications. This study will therefore seek to answer the following questions:

(1) Are there threshold time and space scales for detecting and isolating the quasi-periodic signal of the BAM from background variability?
(2) Are there significant weather and climate implications for the southern midlatitudes?
(3) Given that most atmospheric indices are characterized by irregular variability, why is there such pronounced periodicity associated with the SBAM?
(4) What factor(s) determine the periodicity of the BAM?
(5) Can the BAM be simply modeled as a two-way feedback between tropospheric baroclinicity and eddy kinetic energy? If so, what lessons are there to be learned from this simple paradigm?

(6) How does the Northern Hemisphere (NBAM) compare to the Southern Hemisphere (SBAM)?

(7) Can complex global climate models (GCMs) accurately capture the periodic signal of the BAM? If not, what might they be missing?

These questions will be the subject of the subsequent chapters of this thesis. Chapter 2 will describe the data and methods utilized for analysis in this study. Chapter 3 will present the results from observational analyses of the Southern Hemisphere. In Chapter 4, observational analyses of the Northern Hemisphere BAM will be presented as a comparison to the SBAM. Global climate models will be evaluated for their representation of the BAM in Chapter 5. Chapter 6 will describe the results obtained from a very simple baroclinic conversion model, which attempts to model the SBAM as a two-way linear relationship between baroclinicity and eddy kinetic energy. Finally, Chapter 7 will summarize and conclude this thesis, as well as include some commentary on the implications of this research and questions that remain to be addressed by future researchers.

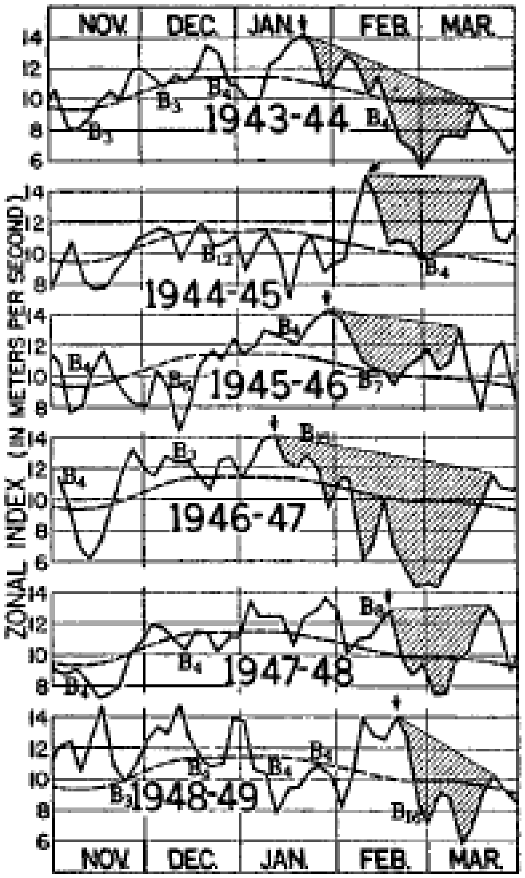

Figure 1.1. From Namias (1950), Fig. 1. The chart shows the difference in 700 hPa wind speeds (in m s^{-1}) between 55°N and 35°N over the western hemisphere for six different extended winters. The shaded regions denote where the primary “index cycle” of each season occurs.

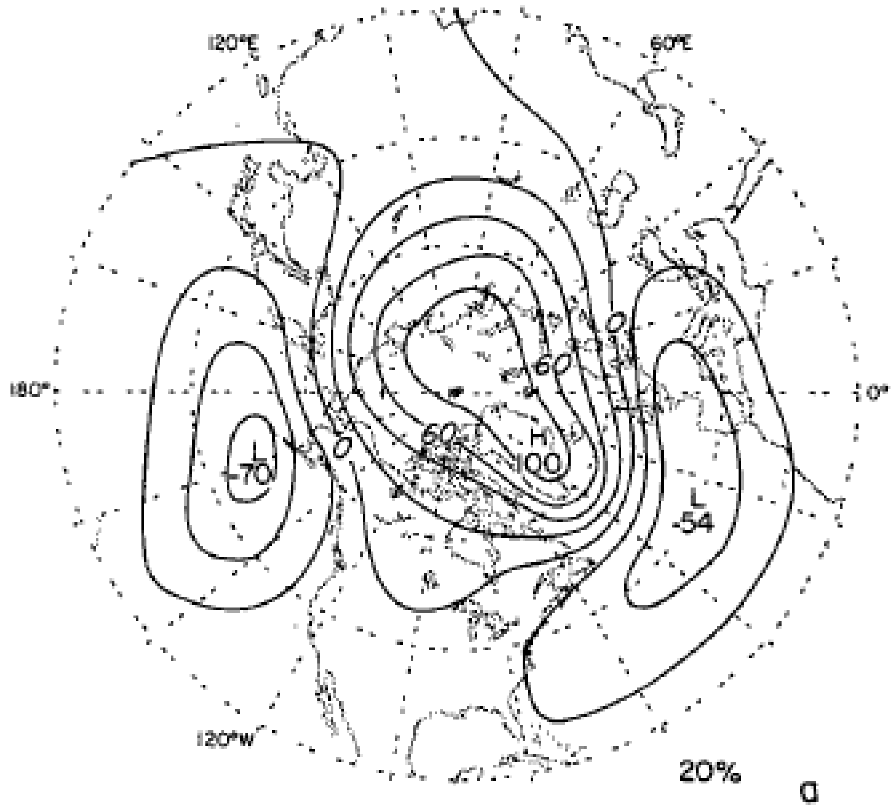

Figure 1.2. From Wallace and Gutzler (1981), Fig. 4. The map shows regressions of sea-level pressure onto the first eigenvector field, normalized such that the largest anomalies are scaled to 100.

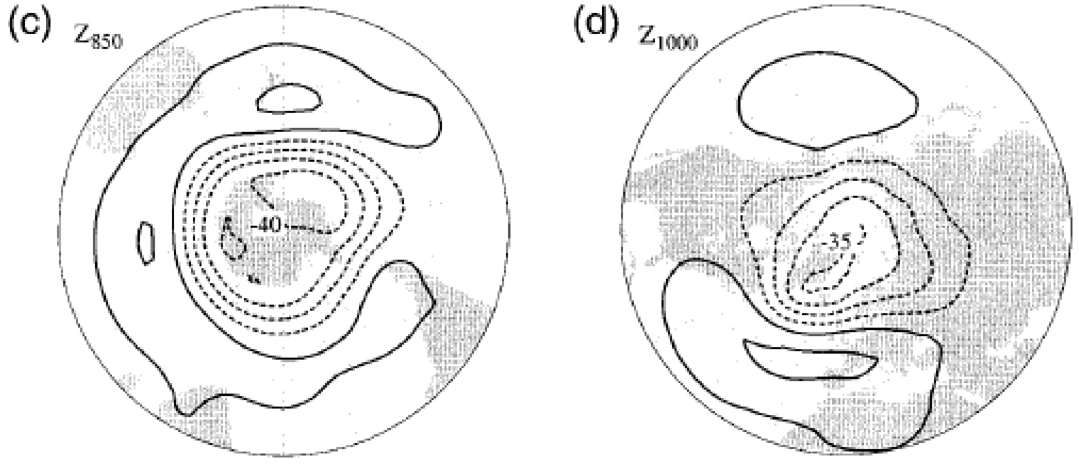

Figure 1.3. From Thompson and Wallace (2000), Fig. 1. Each map is a regression of monthly mean height fields for the designated pressure level onto standardized indices of the annular modes. Note the somewhat higher degree of annularity in the SH (left) as opposed to the NH (right).

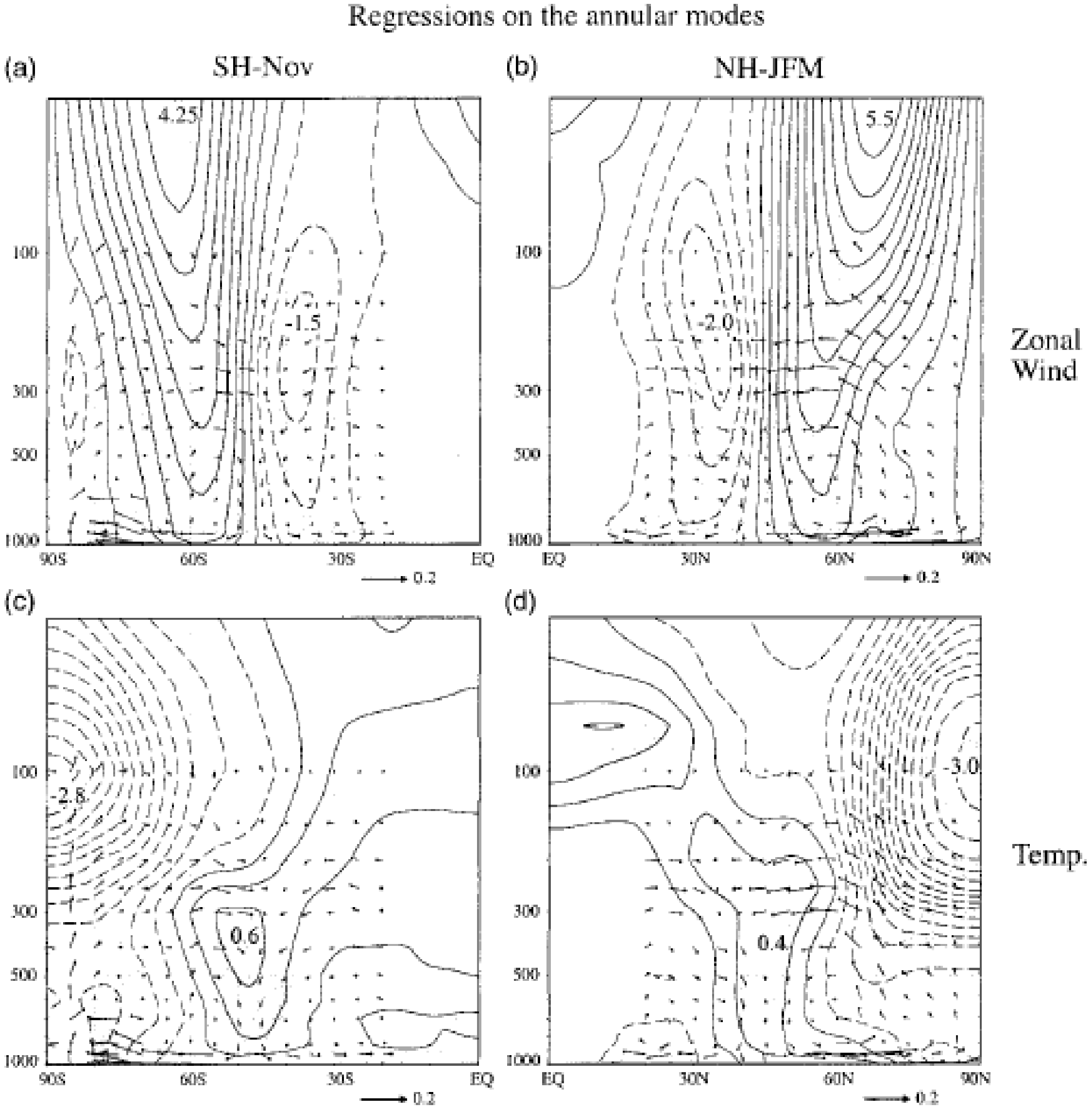

Figure 1.4. From Thompson and Wallace (2000), Fig. 7. As indicated, the charts illustrate regressions of zonal-mean zonal wind and temperature fields from throughout the troposphere and lower stratosphere onto indices of the annular modes. A positive wind or temperature anomaly in the figure indicates that the positive phase of the annular mode is associated with increased winds or temperatures at that given latitude and pressure level. Small arrows indicate the anomalous meridional circulation induced by the annular modes.

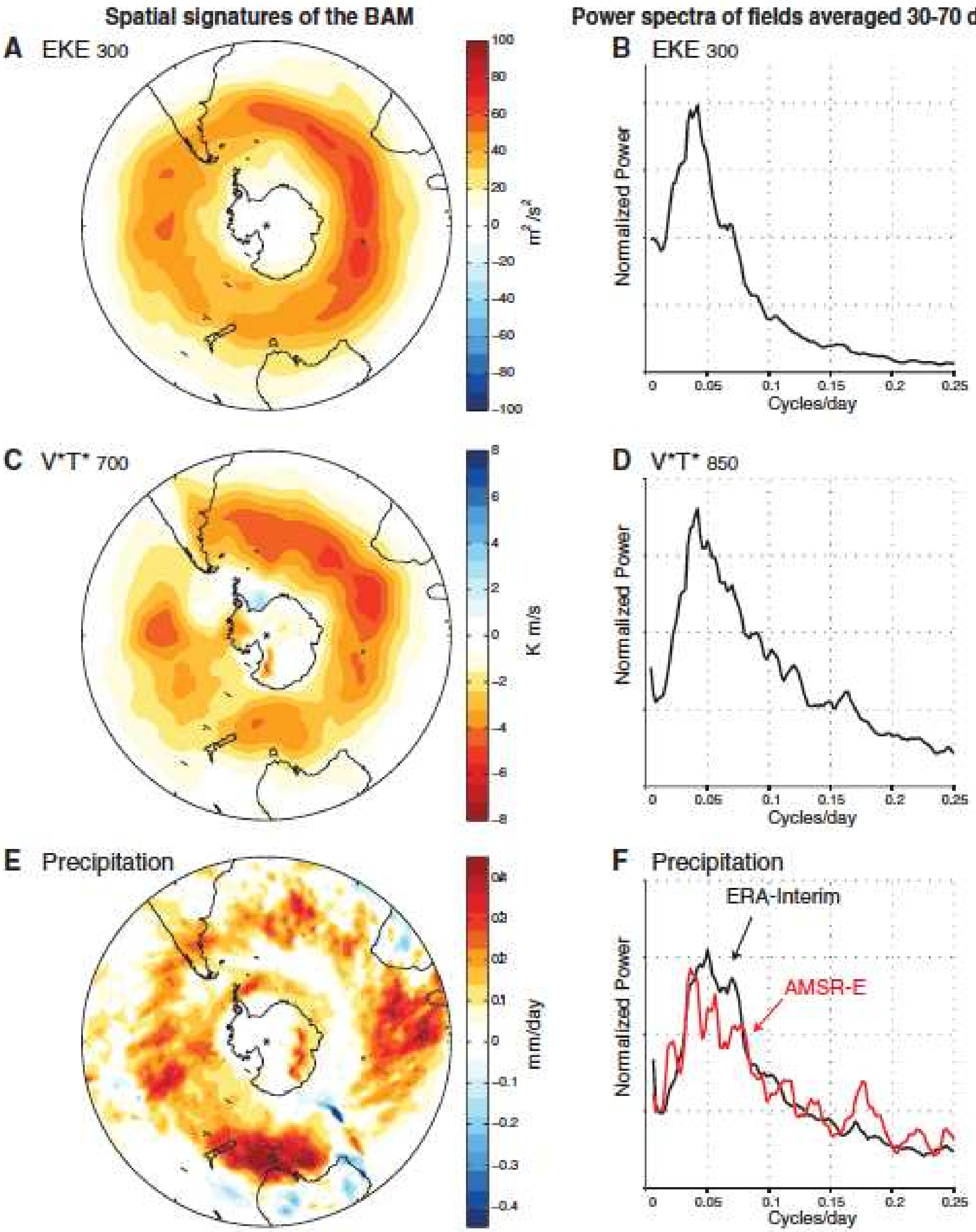

Figure 1.5. From Thompson and Barnes (2014), Fig. 1. Panels in the left column represent the indicated fields regressed onto the SBAM index. Panels in the right column represent normalized power spectra of the 30°-70°S mean time series of the given fields. Note the annular structure in all given fields, as well as the notable periodicity centered on approximately 25 days.

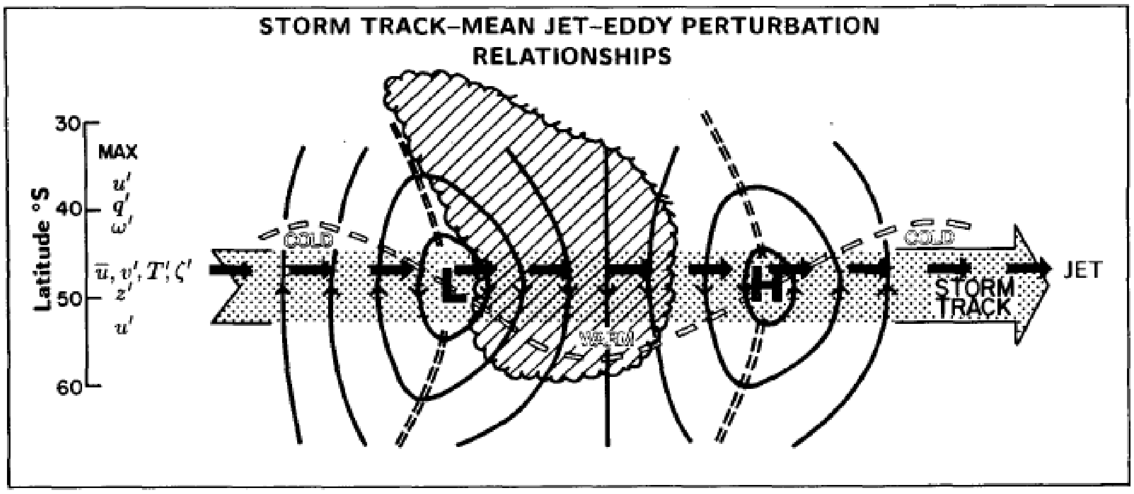

Figure 1.6. From Trenberth (1991), Fig. 1. This figure is a schematic illustration of the relationships between various atmospheric quantities and the mean storm track. The upper-level jet is given by the dashed arrows near 45°S, surface streamlines and pressure features are identified by the "L" and "H" inscribed within single solid contours, and upper-level trough and ridge axes are denoted by the double dashed lines bisecting the surface pressure features. An area of saturation is indicated by the hatched area between the surface low and high.

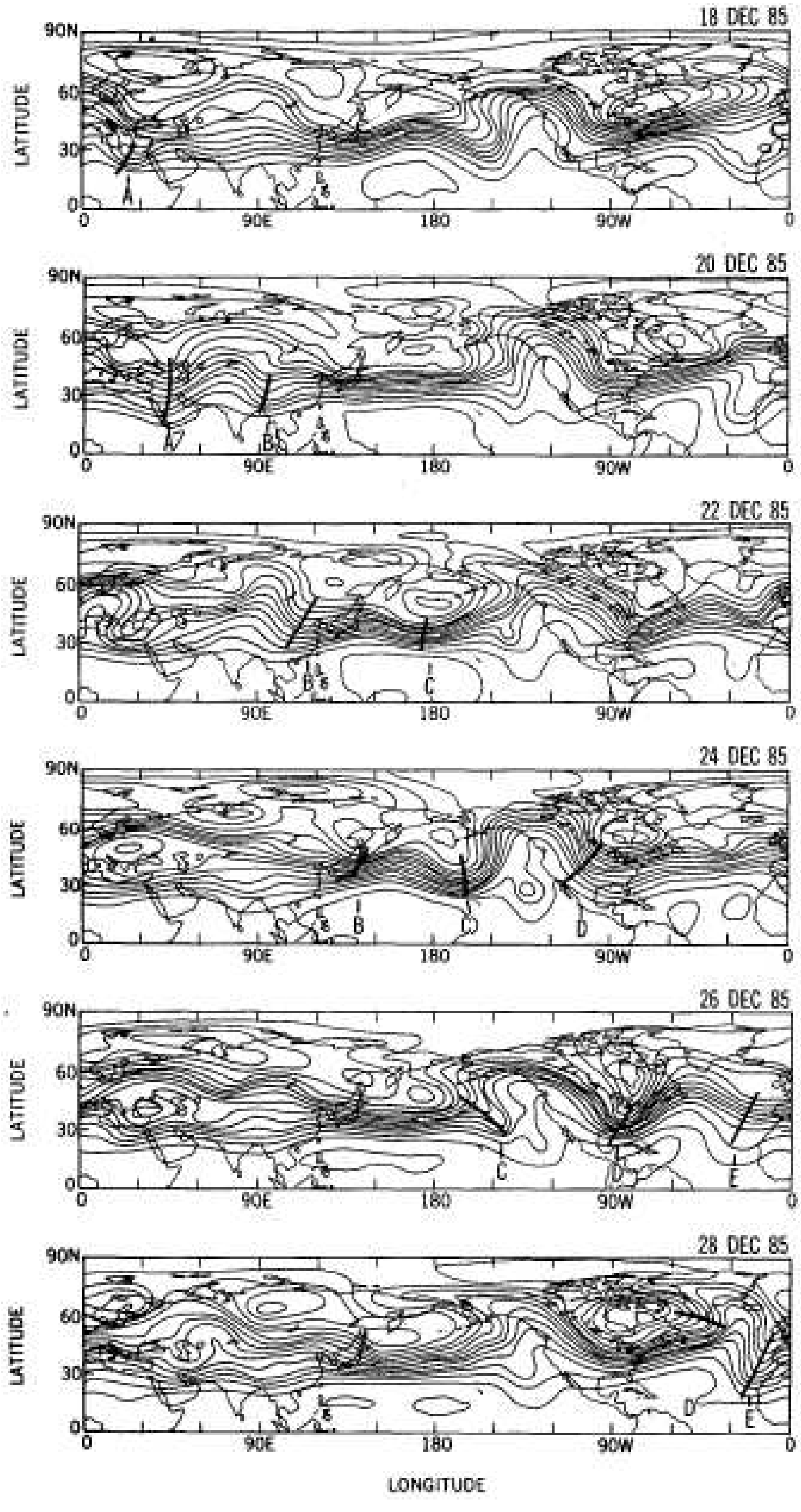
18 DEC 85
20 DEC 85
22 DEC 85
24 DEC 85
26 DEC 85
28 DEC 85
90N
60
30
0
LATITUDE
0
90E
180
90W
0
LONGITUDE
A
B
C
D
E

Figure 1.7 (previous page). From Chang (1993), Fig. 4. Each panel illustrates 300 hPa geopotential heights for the dates indicated. Each trough is designated with a letter, beginning with “A” for the origin disturbance. It can be readily seen that downstream wave development is occurring throughout this time period, with the wave packet essentially completing a circumnavigation of the globe during the 10-day period.

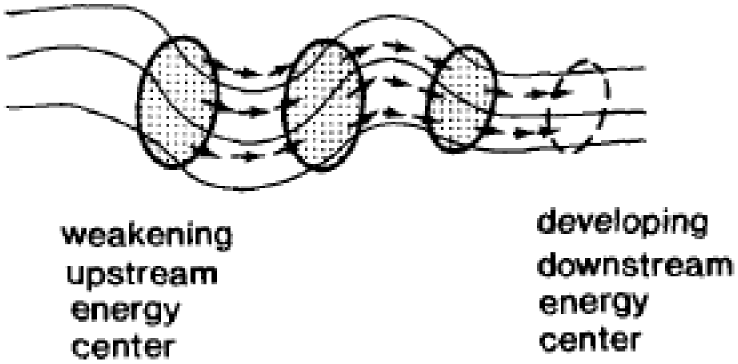

Figure 1.8. From Chang (1993), Fig. 13. The diagram is a schematic representation of the proposed mechanism by which baroclinic waves flux energy downstream ageostrophically, leading to wave development in less baroclinic regions.

CHAPTER TWO

DATA AND METHODOLOGY

The purpose of this chapter is, as implied by its title, to describe the data and methods utilized in analyses for this study. Descriptions of data will include data sources, the atmospheric variables obtained and analyzed, and the spatial and temporal resolution at which they were obtained. The methods subsection will describe how various analyses were conducted, including the mathematical basis for the spectral and lag-regression analyses that will be presented in Chapters 3 and 4.

2.1 Data

For the purposes of this study, it was desirable to have a dataset that met the following criteria:

(1) Has global or near-global coverage,
(2) Has a temporally continuous record of daily values over a time span of sufficient length to encapsulate interannual variability,
(3) Has sufficient spatial resolution to resolve regional-scale atmospheric features.

It therefore seemed most appropriate to employ a reanalysis dataset that offered the necessary variables for our analysis. These necessary variables include U (zonal) and V (meridional) wind speeds at various pressure levels from which to construct the eddy kinetic energy field, temperatures at various pressure levels for calculating heat fluxes and meridional temperature gradients, and precipitation. All of these variables were needed on at least daily time scales; sub-daily data would simply be averaged to daily.

The European Centre for Medium-range Weather Forecasting (ECMWF) has a widely used reanalysis dataset, the ECMWF Interim Reanalysis (henceforth referred to as ERAi). The details of the reanalysis system are described in Dee et al. (2011), and references therein. ERAi daily data are available beginning on 1 Jan 1979, and the most recent data are usually available within two months of real time. The data utilized for this study included 6-hourly values of wind and temperature at various pressure levels for the period 1 Jan 1979 to 31 Dec 2014 (13,149 days, or 36 years). The ERAi data portal enables users to select from multiple spatial resolutions for gridded pressure-level data; all of the data referenced in this study was acquired at 1.5° latitude x 1.5° longitude resolution. U and V winds at all 23 pressure levels between 1000 hPa and 200 hPa (1000, 975, 950, 925, 900, 875, 850, 825, 800, 775, 750, 700, 650, 600, 550, 500, 450, 400, 350, 300, 250, 225, and 200 hPa) were utilized in the full, mass-weighted southern and northern baroclinic annular mode (SBAM and NBAM) indices. Temperature data were only acquired at 850, 700, and 500 hPa, as eddy heat fluxes are most robust in the lower troposphere. While global data were acquired from the online server, only the midlatitudes of each hemisphere (30°-70°S and 30°-70°N) were used in the analyses.

While actual precipitation analyses are not available in ERAi, the system does offer 12-hour forecasts from the ECMWF forecast model. While obviously discrepancies between a model forecast and real observations will exist, the operational ECMWF forecast model has the highest precipitation forecasting skill of any current model (Haiden et al., 2012, and references therein). Additionally, the lack of surface observation stations throughout much of the Southern Hemisphere midlatitudes, our primary area of interest for this study, presents a significant obstacle to using a true observational dataset.

In addition to the analyses that are employed to study the real-world BAM, two Global Climate Models (GCMs) were utilized in Chapter 4 to determine the extent to which the BAM can be represented in models. The first of these models was an “Aquaplanet” model, in which the entire Earth surface is represented as a single slab ocean of homogeneous depth and heat capacity (Frierson et al. 2006). It therefore removes the influences of topography and surface inhomogeneities, creating a simpler system in which to examine the interplay between baroclinicity and EKE. A second simplified GCM used in this study was the Geophysical Fluid Dynamics Laboratory (GFDL) dry dynamical core, which excludes topography and explicit representations of moisture (Held and Suarez 1994; McGraw and Barnes 2016). The two models will be described in greater detail in Chapter 4.

2.2 Construction of Data Arrays

As discussed above, all of the “observational” data in this study comes from the ERA-Interim reanalysis. However, fields such as eddy kinetic energy and eddy heat flux are derived quantities, and are thus not directly output by the reanalysis. This section will describe how each derived field is calculated from output variables.

Eddy kinetic energy, as mentioned in section 1.3.1, is calculated from zonal anomalies of u and v winds (u^* and v^*). To calculate EKE at a given pressure level, it is first necessary to calculate zonal-mean quantities of u and v and subtract them from the data, producing zonal-anomaly *u* and *v*, or *u** and *v**. These quantities are then squared, added together, and divided by 2 to produce an array of 6-hourly EKE. The 6-hourly EKE values are then averaged to daily values before subtracting the seasonally-varying mean to produce a final array of daily EKE anomalies. Henceforth, references to EKE will be referring to this time-anomalous, daily-mean EKE array.

Eddy heat fluxes are calculated in a similar manner to EKE, albeit at fewer pressure levels. First, 6-hourly arrays of *v* and *T* (temperature in Kelvin) are converted into zonal anomalies by removing the zonal means from each quantity. These two fields are then multiplied together (EHF = v^*T^*) and averaged to daily. The seasonal cycle is then removed to produce EHF anomalies. Such calculations are done at the 850 hPa and 700 hPa pressure levels only, since heat fluxes are best represented in the lower troposphere. The resulting arrays contain daily-mean anomalous eddy heat flux, and will be referred to simply as "eddy heat flux" or "EHF" throughout the remainder of this thesis.

A small number of other data matrices and time series will be utilized for some other calculations in this study. One such example is the ERA-Interim precipitation, which is calculated from 12-hour forecast values from the ECMWF forecast model. These data are considered accurate enough to serve as a proxy for observed precipitation. Producing an array of daily precipitation is quite simple: the two 12-hour values per day are simply added at each grid point.

While the specifics of the simple baroclinic conversion model will be discussed in section 2.3.3 and Chapter 6, a brief description of the data will be provided here. One input into the model is a "baroclinicity" time series, which was simply produced using 500 hPa temperatures. At all longitudes and times, the temperature at 60°S was subtracted from the temperature at 40°S and divided by the distance (in meters) between the two latitude circles. The time series is then produced by averaging the values at all longitudes, resulting in a time series of zonal-mean baroclinicity in Kelvin per meter (K/m).

2.3 Methodology

Much of the observational analysis done for this study is based upon spectral analyses and lag-regression/lag-correlation analyses. This section will discuss the mathematical basis for each of these types of analysis. Additionally, specific parameters utilized in producing the spectra presented in Chapters 3, 4, and 5 will be discussed in 2.3.1. In 2.3.2, the calculation of the lag-regression and lag-correlation plots will be discussed in detail. Finally, this chapter will conclude by describing the methods utilized for significance testing in 2.3.3.

2.3.1 Spectral analysis

The periodicity discussed throughout this thesis is most robustly revealed in power spectra of EKE, EHF, and precipitation time series on large spatial scales. To produce power spectra, the gridded latitude by longitude by time data matrix is first averaged over a specific range of latitudes (usually 30-70° or 40-60°). Then, the mean value is calculated over either the entire hemisphere (all longitudes) or a subset of longitudes. This produces a daily-mean anomalous time series, which is then passed on to a program to calculate the power spectrum.

The "spectrum maker" program operates by selecting subsets of the time series, which are generally 500 days in length with a 50% (i.e., 250 days) overlap between sections. Spectra are then calculated for these individual subsets via Fourier transformation of the time series anomalies. All individual spectra are then averaged together and smoothed using a 3-point filter to produce the final power spectrum. Resulting mean spectra have approximately 70 degrees of freedom each.

2.3.2 Lag-correlation analyses

One type of analysis that underpins much of the exploration of the BAM that is described in this thesis is the lag-correlation analysis. Lag-correlation of time series is quite simple: the correlation coefficient is calculated with one time series shifted by however many indices correspond to the lag in question (e.g., daily values are shifted by one when determining the lag-one correlation). Such correlation sequences can be instrumental in assessing the time scale on which one variable leads another. Several lag-autocorrelations will be presented in Section 3.2, which are simply the lag-correlation of the given time series with itself to examine the amount of physical "memory" that exists in the time series.

A second form of lag-correlation analysis is used to explore the spatial coherence and propagation of features in physically derived quantities such as eddy kinetic energy. These analyses are conducted by averaging over a selected latitude band (typically 40-60°) at every longitude, then correlating each longitude slice with every other longitude at each lag. The resulting correlation "maps" illustrate how physical features such as wave packets propagate in both space and time. Such analyses will be used in particular to elucidate the behavior of wave packets on synoptic scales.

2.3.3 Significance testing

While the lag-correlation and spectral analyses are themselves illustrative of concepts useful to this thesis, the emergent signals must at times be assessed for statistical significance. Depending on the type of analysis, there are a number of different techniques available for such assessments.

For spectral analyses, the most straightforward way to accomplish this is to utilize a comparison to a hypothesis curve based on the expected shape of the spectra. Time series of geophysical variables are generally assumed to resemble red noise due to the nature of the "memory" in such variables – red noise contains some degree of memory from the previous time step with some random amount of noise. Red noise curves essentially resemble exponential decay, with the greatest power at very low frequencies steadily decaying to no power at very high frequencies.

Producing a red noise hypothesis curve is done via the univariate lag-one autoregressive process (a.k.a. the Markov process). As the name implies, the lag-one autocorrelation of the time series being fit is calculated. Then, the following formula is utilized for the requisite number of time steps, creating a time series that contains random white noise as well as memory commensurate with the lag-one autocorrelation of the test series (Torrence and Compo 1998):

$$(2.1)\ \ x(n) = \alpha x(n-1) + \varepsilon(1-\alpha^2)^{1/2}$$

where α is the lag-one autocorrelation and ε is a random variable between 0 and 1. This time series then undergoes the same Fourier transformation process that the other spectra are treated with, resulting in a "best-fit" red noise spectrum. The process is repeated 100 times and the resulting spectra are averaged together (commonly referred to as a "Monte Carlo" technique).

Confidence intervals are then calculated by using the F-statistic. The critical F-value is determined by looking at a table for the F-statistic based on the degrees of freedom of the test time series and the "fit" time series, respectively. Multiplying and dividing the red noise fit curve by the critical F-value produces the upper and lower confidence boundaries, respectively. Points on the spectrum of the test time series that surpass either boundary are considered significant at the 95% threshold (although, of course, roughly 5% of points will do this by pure chance).

Determining the significance of correlation values in the oft-utilized Hovmoeller diagrams is done by employing a Student's t-test. In the 13,149-element daily band-mean EKE or EHF time series, the critical one-tailed t-value is approximately 0.02 for a 95% confidence interval. Correlations exceeding this value are considered significant.

The analysis methods discussed at length in this chapter will form the basis of the observational and model analyses in the chapters that follow. In general, spectral analyses form the basis for our argument in favor of a quasi-periodic behavior in the extratropical atmosphere, and lag-correlations illustrate spatial variations in this behavior. Significance testing reveals many of these features to be significant, as will be shown in the subsequent chapters.

CHAPTER THREE

OBSERVATIONAL ANALYSIS OF THE SOUTHERN HEMISPHERE

The Baroclinic Annular Mode (BAM), which was introduced in Section 1.1, has projections onto several atmospheric parameters that are key to sensible weather and climate. All of the figures and data presented in this section were created utilizing the ERA-Interim reanalysis dataset (as detailed in Section 2.1), which for our purposes we are treating as observations. In the following sections, we will explore zonal-mean and longitudinally varying characteristics of the SBAM, as well as explore the sensitivity of our analyses to spatial and temporal variability.

3.1 Spectral Analysis

The defining characteristic of the BAM is the robust periodicity that reveals itself in large-scale, area-mean quantities of eddy kinetic energy (EKE), eddy heat flux (EHF), and large-scale precipitation fields. Many geophysical variables can be approximated by Gaussian red noise, indicating some degree of day-to-day memory in the system that diminishes with time. Few natural systems contain truly periodic variability, as most are subject to irregular or chaotic variability. The BAM is therefore both unusual and significant in that it is robustly periodic on timescales of approximately 20-30 days.

Utilizing spectral analysis as detailed in Section 2.2.1, this section will explore periodicity in these fields in terms of midlatitude zonal-mean quantities (Section 3.1.1), mean quantities at smaller scales (Section 3.1.2), and in a flow-following time series (Section 3.1.3).

3.1.1 Midlatitude means

The SBAM is a large-scale phenomenon, showing up most prominently on hemispheric space and interannual to decadal time scales. The analyses in this section were constructed by averaging the field in question over the 30°-70° (midlatitude) and 40°-60° ("stormtrack") latitude bands for daily values running from 1979-2014. These spectra therefore represent the distribution of frequencies of each field on the hemispheric scale in the midlatitudes. Statistically significant spectral peaks on this scale can be thought of as representing the "pulsing" of the extratropical storm track: any robust frequencies that occur are indicative of hemisphere-wide fluctuations on those time scales. The field that most closely defines the BAM, eddy kinetic energy, will be discussed first.

3.1.1.1 Eddy kinetic energy

Eddy kinetic energy, which we defined in Chapter 1 as the added squares of the u and v zonal anomalies, can be thought of as a measure of storm activity on a large scale. Prominent zonal jet streaks are associated with large u^* and can therefore contribute to positive eddy kinetic energy anomalies at times, but most eddy kinetic energy anomalies are driven by variations in v^*. As such, periods of high wave activity, which are frequently associated with strong meridional winds, are generally the cause of positive eddy kinetic energy anomalies and vice-versa. It is therefore a reasonable assumption that our analysis of EKE anomalies can be treated as an assessment of large-scale storminess.

It's worth noting at this point that the nature of power spectra means that our analyses do not describe a true regularity to the cycle of hemispheric-mean EKE anomalies. Purely periodic behavior would show up in a power spectrum as having all power concentrated at one frequency and its harmonics (e.g., spikes at 0.05, 0.1, 0.2, etc.). Rather, the use of the term "periodicity" with regards to extratropical cyclone activity in the midlatitudes is simply made in reference to the unusual concentration of spectral power in the frequencies corresponding to 20-30 days. Such behavior is still significant because it has its origins in physical processes contributing to the production of extratropical cyclone activity. The potential physical implications of this will be discussed further in Chapter 6.

The robust periodicity referred to frequently throughout this thesis is most directly illustrated in Figures 3.1 and 3.2. The first of these figures simply shows the normalized power spectra of 300 hPa EKE anomalies averaged over two different latitude bands: the 30-70°S "midlatitude" and 40-60°S "stormtrack." A pronounced spectral peak is obvious around 0.04 cycles per day, corresponding to a period of approximately 25 days. However, the peak is rather broad, and thus we typically characterize the periodicity of the BAM as being in the 20-30 day range. A red noise fit is overlaid on the midlatitude band EKE in Figure 3.2 to illustrate the departure from the "typical" behavior of geophysical variables.

3.1.1.2 Eddy heat flux

Another field in which the periodic nature of the BAM is clearly evident on large scales is eddy heat flux (EHF). Time series of mean upper-tropospheric EKE and lower-tropospheric EHF over 30-70°S are correlated at around -0.6 with EHF leading EKE by approximately one day. This makes sense in the context of the lifecycle of baroclinic waves:

eddy heat flux anomalies in the lower troposphere cause amplification of baroclinic waves, producing meridional wind anomalies that contribute to EKE anomalies. This relationship can be seen rather clearly in Figure 3.3, which illustrates the correlation between the two time series for lags ranging from -30 (EHF leads EKE) to +30 (EKE leads EHF) days. A rather weak relationship exists outside of lags +/- 3 days, but the influence of EHF anomalies on generating EKE anomalies can clearly be seen.

As one might expect from these results, the spectrum of EHF looks broadly similar to that of EKE (Figure 3.4). A pronounced peak in spectral power is present at 0.04 cycles per day, with the remainder of the spectrum bearing a strong resemblance to the red noise fit. Periodicity in the hemisphere-mean eddy heat flux field, like that of the hemisphere-mean EKE field, is suggestive of a recurring cycle of baroclinic wave development and decay. The basic principle has been understood since the 1940s and 1950s (see Chapter 1), but only in our analyses is this periodicity so evident. While the implications of this will be discussed in later chapters, clearly there are physical mechanisms that determine the time scale for the build-up and release of baroclinicity. The quasi-periodicity in extratropical cyclone activity is a direct consequence of such a time scale.

3.1.1.3 Precipitation

Yet another important field in which we see evidence of periodicity is in the hemispheric mean of daily precipitation. As described in Chapter 2, the precipitation is based on ECMWF forecast model output, and is therefore subject to the limitations of grid spacing and whatever biases plague the model’s forecasts. However, on a large scale, such an estimate should be sufficient for our purposes.

Rather interesting spectra emerge from analyses of the two latitude bands of choice. The full midlatitude spectrum (Figure 3.5) has a broad spectral peak ranging between approximately 0.04 and 0.07 cycles per day (14 to 25 days), which likely results from two separate processes: the generation of precipitation on time scales consistent with the baroclinic annular mode, and the advection time scale for a wave packet circling the SH. This second point will be explored more thoroughly in the lag-correlation and lag-regression analyses presented later in this chapter. The reason the advection time scale would come into play in the precipitation field is due to the hemispheric asymmetries in storm development and decay. With baroclinicity in the SH at its weakest over the South Pacific Ocean, cyclones are generally in a state of decay in that region. This leads to lesser precipitation amounts over the South Pacific, and therefore a quasi-periodicity associated with a continuous wave packet circling the globe appears in our spectral analysis.

Perhaps the more interesting result is the stark contrast between the broader midlatitude band spectrum and the more focused stormtrack band. Unlike that of EKE, the spectra between the two different bands in the SH are markedly different from one another. When just the 40-60°S mean is analyzed, the broad spectral peak discussed previously nearly disappears. The reasons for this are not entirely clear, but one possibility is that the 40-60°S latitudes experience such frequent precipitation that the periodicity is not discernable, whereas the 30-40°S and 60-70°S latitudes are more dependent on greater levels of cyclone activity for significant precipitation. Thus, the more general "midlatitude" precipitation anomaly reflects a greater impact from the SBAM. A deeper examination of the role of varying spatial scales follows in the next section.

3.1.2 Spectra at smaller spatial scales

Antecedent studies had previously demonstrated the quasi-periodicity in the extratropical circulation (e.g., Thompson and Barnes 2014; Thompson and Woodworth 2014), but these studies considered just hemispheric-scale variability. In order to more fully appreciate how the BAM projects onto smaller spatial scales, spectra for 300 hPa EKE were calculated over a variety of longitude spans from 360° down to 45°. Each longitude span was utilized with an anchor point at every grid point (i.e., for 45° spectra, 1.5° to 46.5°, 3.0° to 48.0°, etc.) and then averaged together. These results are shown for the SH in Figure 3.6.

Spectral power peaks robustly in the SH at frequencies of around 0.04 cycles per day, no matter what longitude span is being evaluated. However, the magnitude of the peak diminishes as the spatial scale shrinks, indicating the mean spectrum regressing more and more towards red noise behavior. While assigning a single cut-off value is difficult, it seems reasonable to conclude that the BAM retains its influence down to longitude spans of at least 120°. Further evidence for this may be found in the paper that accompanies this chapter (Thompson et al. 2016, submitted to JAS).

This result makes intuitive sense, as the large-scale influence of the BAM becomes progressively less important as synoptic- and local-scale processes become progressively larger factors in the development of EKE anomalies. As a general rule, observing smaller and smaller spatial scales causes progressively more obscuration of the BAM signal. The synoptic-scale behavior of wave packets will be explored further via lag-correlation analysis later in this chapter.

3.1.3 Spectra on shorter time scales

The effect of shorter time scales on EKE and EHF spectra was also explored in the SH, but with unclear results. Six-year spans yielded spectral peaks of somewhat varying magnitude, but all centered on 0.04 cycles per day (not shown). More interestingly, the decadal spectra (1980-1989, 1990-1999, 2000-2009) had spectral peaks at frequencies varying between 0.03 and 0.06, with the majority of the power around 0.04 cycles per day coming from the 1990s (Figure 3.7). A cursory examination of these results suggested that some form of multidecadal variability could be invoked as a possible explanation. However, the analysis was repeated using every decadal subset in our record (1979-1988, 1980-1989, 1981-1990, etc.) in order to test the effects of sampling variability. The results clearly indicate that the decadal spectra all fall within the confidence bounds delineated by using the F-statistic with degrees of freedom consistent with 10-year time series.

The possible influence of El Nino was considered as well – each major cold (-1.0°C Oceanic Nino Index or less) and major warm (+1.0°C ONI or greater) episode in the ERAi record was analyzed by isolating the 18-month periods of the 30-70°S mean time series of EKE centered on the peak ONI month. Each spectrum was produced using 250 day subsets, and therefore just two realizations were typical for each event. The results are mixed, with spectral power peaks scattered between frequencies of approximately 0.02 to 0.07 cycles per day (Figure 3.8). However, two notable events appear to stand out: the “super El Nino” of 1997-1998 and the very strong La Nina of 2010-2011.

Both events exhibit robust spectral peaks right around 0.04 cycles per day, and stand out well above other events. However, due to the limitations imposed by sampling variability and the lack of a clear association between stronger ENSO episodes and a more robust BAM, these results remain inconclusive. Like with the decadal spectra, a sampling variability test was conducted (Figure 3.9) to illustrate the range of variability associated with such short timescales. Therefore, while it is possible that ENSO has some interaction with the BAM, the more likely explanation for differences between events is simply sampling variability.

While the 36-year reanalysis analyzed in this study was insufficient to effectively examine any such connection, it is possible that the BAM is modulated on decadal and longer time scales by such multi-decadal oceanic oscillations as the Atlantic Multidecadal Oscillation (AMO) and the Pacific Decadal Oscillation (PDO). These patterns are associated with significant alterations of global SST patterns and could therefore contribute to altering baroclinicity on regional scales. Using different datasets, particularly reanalyses with longer analysis periods, may have enabled such an investigation. Future studies may wish to further examine the possible linkages between the BAM and other large-scale climate oscillations on interannual to decadal time scales.

3.1.4 Flow-following spectra

In addition to exploring various time and space scales to find the limits of influence for the BAM signal, spectra were also calculated for anomaly time series following various flow rates. The purpose of such an exercise was to determine the role of mean-flow advection in modulating the apparent periodicity due to the BAM. Beginning from a grid of latitude band-mean EKE anomalies, the flow is "followed" by calculating the advection distance per time step. This distance is rounded to the nearest longitude, and that longitude is selected for the time series. This time series then undergoes the standard procedure for calculation of power spectra. The results are presented in Figure 3.10.

As evidenced by Figure 3.10, periodicity in SH EKE anomalies emerges most clearly at intermediate flow rates of approximately 5 to 15 m/s. At a flow rate of zero, which is the spectrum of a time series from a single longitude, the spectrum strongly resembles that of red noise. However, at flow rates of approximately 5 to 15 m/s, a peak in spectral power emerges around 0.04-0.05 cycles per day (the exact peaks in this region are obscured by the saturation of the color scale), corresponding to the periodicity of the SBAM.

Interestingly, the periodicity then becomes less apparent at faster flow rates, including those close to the group velocity of wave packets (~25 m/s). While intuitively it may be expected that the periodicity should emerge following a wave packet as it propagates around the hemisphere, the signal is at its clearest at intermediate velocities. The reasons for this will be discussed more fully in the lag-correlations section, but in essence, it has to do with where the negative, positive, negative anomaly pattern emerges. Negative EKE anomalies develop in the wake of the wave packet, which are then followed by positive anomalies some time later. From a hemispheric perspective, the mean EKE across the hemisphere waxes and wanes on a roughly 25 day cycle; from a wave-packet perspective, the largest (dominant) anomalies grow and decay at different locations throughout the hemisphere, giving the appearance of a less “periodic” variability.

3.2 Lag-Correlation Analyses

The various spectral analyses discussed in the previous section are a useful tool for assessing the variability at a range of frequencies in a given time series, but they offer no information about the spatial structure of the data. By correlating anomalies in a space-by-time array with all other points in space at numerous time lags, a region of high correlations emerges in association with the propagation of those anomalies, typically due to the action of a wave packet. The lag-correlation analyses discussed in this section therefore serve to illustrate the continuity of anomalies in space and time.

3.2.1 Eddy kinetic energy

The simplest framework from which to view the variation of EKE anomaly correlations in time is through the stormtrack-mean perspective. The autocorrelation sequence for 40-60°S 300 hPa EKE anomalies is given by the right-hand panel of Figure 3.11. As expected, correlations monotonically decrease from lag 0 to around lag 8, a result you'd expect from a geophysical variable with some day-to-day systemic "memory." However, correlations reach a minimum (maximum negative correlation) around days 9-10, in association with the development of negative EKE anomalies throughout much of the hemisphere. These correlations are statistically significant at the 95% confidence level, using a one-tailed test of the t-statistic assuming much greater than 100 degrees of freedom. Correlations then regress towards zero again between days ~15 and 22 before reaching a secondary positive maximum around day ~25. This secondary maximum is indicative of the re-emergence of positive EKE anomalies on the timescale of the BAM, and is roughly equivalent to the threshold of statistical significance (approximately r = 0.04).

While the zonal-mean autocorrelation perspective again supports the notion of a quasi-periodicity in the SH extratropical circulation, it is perhaps more useful to see the spatial variability in anomaly correlations. By calculating correlations between longitude-band averages (i.e., EKE anomalies at a given longitude averaged between 40°S and 60°S) at various time lags from -30 to +30 days, a Hovmoeller plot of EKE anomalies propagating zonally and temporally is produced (Figure 3.11, left panel, and Figure 3.12). Two such plots of 300 hPa EKE anomaly lag-correlations have been provided: Figure 3.11 shows what such an anomaly correlation diagram looks like at a single longitude (in this case, 180°E), and Figure 3.12 shows what an average of all single-longitude maps "stacked" at the same longitude looks like. The patterns are roughly the same, but the mean Hovmoeller plot removes some of the noise and any spurious features that may be the result of local variability. This practice also serves to increase the sample size of the analysis, but may result in a slight underestimation of the population correlation (e.g., Thompson et al. 2016, Fischer 1921).

The main feature of interest in both plots is the region of saturated positive correlations (red) running for approximately +/- 7 days from longitude 0, lag 0. This feature of highly correlated EKE anomalies is associated with a Rossby wave packet, propagating around the globe at approximately the Rossby group velocity of 25 m/s (shallow black line). Flanking the core of the wave packet are two regions of strong negative correlations (blue), associated with the negative EKE anomalies that develop in the wake of an anomalous wave packet. Along a line of 8 m/s (steep black line), or approximately the Rossby wave phase speed, a sequence of alternating positive and negative correlations can be seen as EKE anomalies grow and decay with each passing wave.

Figure 3.13 provides a more detailed depiction of the appearance of individual wave phases in correlation space. The correlation field is the same as that of Figure 3.12, but the color scale has been adjusted to prevent saturation, and only lags -8 to +8 are shown. The small negative correlations are now no longer apparent, but instead a sequence of positive correlation centers can now be seen within the confines of the main wave packet. These results are consistent with established principles of Rossby wave propagation and downstream development (see Section 1.3.3), but also reveal how negative EKE anomalies emerge in the wake of wave packets.

Further illumination of the development of the negative anomalies in the wake of a wave packet is provided by Figure 3.14. The correlations at each longitude correspond to the 30° longitude running-mean EKE correlations at the specified longitude and lag. Like Figure 3.12, a mean correlation over all separate longitudinal realizations has been utilized here, and as such the x-axis is labeled with relative longitudes. Longitudes have also been repeated such that the plot shows 1.5 repetitions of Earth, allowing easier visualization of anomalies propagating all the way around the globe.

This way of presenting the lag-correlations allows one's eye to track the propagation of the main anomalous wave packet to the east. The emergence of trailing negative EKE anomaly correlations is also evident in the period from lag ~3 to lag ~15. Significant positive anomalies then re-emerge around day 25, approximately 180° downstream of the original location of the positive anomalies. This spatial lag also helps explain the result seen in Figure 3.10, the flow-following spectra: spectral power maxima are at their greatest at flow rates between 5 and 12 m/s. Flow rates of this magnitude are intermediate to both the phase speed and group velocity of the wave packet, and likely correspond to a pathway along which baroclinicity and EKE anomalies alternate most periodically.

This alternating pattern of positive-negative-positive anomalies is also made clear by the right panel of Figure 3.14, which highlights the variation in zonal-mean correlations: positive between lags -6 and +6, negative from day +6 to day +22, and then positive correlations re-emerge thereafter. Such a progression is consistent with the quasi-periodicity evident in the large-scale spectral analyses discussed in Section 3.1.

3.2.2 Eddy heat flux

As with upper-tropospheric EKE, we begin our analyses of 850 hPa eddy heat flux in the SH with a time series autocorrelation sequence (Figure 3.15, right panel). Correlations drop off far more rapidly with EHF than with EKE, with positive correlations losing their statistical significance by day 3. There is then a brief window of statistically significant negative correlations between days ~5 and 9 before correlations become statistically indistinguishable from zero thereafter.

Several possible explanations for this behavior exist; for one, lower-tropospheric EHF anomalies are not entirely coupled to upper-tropospheric EKE anomalies. Notable eddy heat fluxes can occur in conjunction with standing waves coincident with an anomalous temperature gradient, and therefore be largely decoupled from EKE anomalies aloft. EKE anomalies also lag EHF anomalies (as evidenced by Figure 3.3), due in part to bottom-up baroclinic cyclogenesis and the continuation of high-amplitude waves after the occlusion process.

Occam's Razor would suggest that the low zonal-mean correlations are simply due to the nature of EHF anomalies: alternating couplets of high and low correlation occur with each wave phase since heat fluxes are of opposite sign on the upstream and downstream sides of the cyclone (Figure 3.15, left panel and Figure 3.16). Since the time series is a mean of just 40-60°S anomalies, there should be a net poleward (negative EHF anomalies) heat flux, and the anomalies should not quite average to zero. It does seem likely that this effect would mute zonal-mean correlations sufficiently to limit the emergence of statistically significant correlations at large lags.

The alternating couplets of high and low correlation alluded to previously are clearly evident in Figures 3.15 and 3.16, which are the same type of lag-correlation Hovmoeller plots as in the previous section. Much like the EKE plots, a wave packet can be quite clearly traced along a 25 m/s propagation line, this time through alternating centers of large positive and negative correlations. A phase speed of 8 m/s also nicely tracks individual correlation centers well for approximately +/- 4 days before diminishing below significance thresholds.

As in the zonal mean, this drop off of correlations in time occurs more quickly than with EKE. Familiarity with daily weather patterns offers some insight into why this may be. Upper-tropospheric features (anomalous troughs and ridges, for example) tend to be more persistent features in time and space than lower-tropospheric features. While numerous feedbacks occur between upper and lower atmospheric features, a single 300 hPa EKE anomaly (say, a persistent trough) may be associated with multiple lower-tropospheric pressure centers (cyclones), which may not be as temporally persistent. The formation and occlusion of individual lower-tropospheric cyclones generally happens more rapidly than the formation and dissipation of upper-level EKE anomalies, and the EHF correlations therefore fade more rapidly in time.

Organized correlation anomalies near lags +25 and -25 are also not as clear in EHF as in EKE, although some hints of larger correlations exist near days +20 and -20. Again, the short-lived nature of significant EHF anomalies is probably the reason for this apparent lack of periodicity, though this does not explain the presence of anomalies around ~20 days as opposed to ~25.

Traceable, significant lower-tropospheric eddy heat flux anomalies in association with the SBAM clearly imply a connection to sensible weather in the southern midlatitudes. While the implications of the SBAM's impact on weather and climate will be more fully discussed in Chapter 7, the modulation of both EKE and EHF anomalies is indicative of significant effects on cyclogenesis and cyclolysis on large scales. While the attenuation of the periodic signal at smaller spatial scales leaves doubt as to how apparent these effects are to a given region or location, at least some component of intraseasonal variability can likely be ascribed to the SBAM.

3.2.3 Precipitation

Given the present understanding of how the SBAM modulates upper-tropospheric eddy kinetic energy and lower-tropospheric eddy heat flux, it logically follows that precipitation anomalies will also be modulated accordingly. However, the precipitation data utilized for these analyses has its limitations.

As briefly described in Chapter 2, the daily precipitation arrays were developed from adding the two 12-hour forecast periods from the ECMWF forecast for each given day. These 12-hour forecasts are the most accurate produced by today's models (Haiden et al. 2012) and are among the most accurate representations of global precipitation that exist (most global precipitation data sets are based on satellite retrievals, which are subject to considerable bias and uncertainty; see e.g., Maggioni et al. 2016). Obviously the model has biases of its own, but as we have considered other reanalysis products to be sufficiently accurate to be treated as observations, we will do the same in this case.

The largest problem by far is the projection of the model forecasts onto the reanalysis grid. The operational ECMWF model runs at a spectral resolution of T1279, which translates into an approximate horizontal resolution of 20 km at 50°S. However, the reanalysis grid is 1.5°x1.5°, or an approximate horizontal resolution of 107.5 km zonally by 167.5 km meridionally. Each point in the reanalysis is effectively an average over a region of ~5 by ~8 grid points, which can obviously obscure mesoscale precipitation features (narrow frontal precipitation bands, convective features, etc.). The overall effect will be to dampen the largest anomalies, leading to less robust correlation centers.

An even greater areal average is given by the autocorrelation sequence for the 40-60°S mean precipitation time series in Figure 3.17 (right panel). In contrast to the behavior observed with EKE and EHF, the band-mean correlation never dips below the threshold for significant negative correlations. This suggests that the effect of the SBAM on precipitation is not sufficient for a period of significant negative precipitation anomalies (reduced precipitation) to follow particularly active periods. Quasi-periodicity is also difficult to ascertain, as the autocorrelation sequence flirts with the 95% significance threshold from ~days 12 to 30.

The Hovmoeller diagram (Figure 3.17, left panel) of 40-60°S precipitation offers little additional clarity. The same alternating couplets of high and low correlation as in the EHF Hovmoeller are present along the path of the main wave packet. Crucially, however, there appears to be little to no indication of a re-emergence of significant anomaly correlations around the requisite ~20-30 days. Whether this absence is a product of signal loss from large-scale precipitation averages is difficult to determine. However, it also seems probable that within the 40-60°S latitude band, it simply precipitates too often for significant frequencies to emerge. While the SBAM possesses a clear quasi-periodic influence over EKE and EHF anomalies, any such influence on large-scale precipitation is difficult to isolate.

3.3 Summarizing Remarks on Observations of the SBAM

The Southern Baroclinic Annular Mode has been revealed in this analysis of ERA-Interim reanalysis data to be a robust modulator of numerous aspects of extratropical cyclone development and propagation. This effect is most clearly observable in spectral analyses of upper-tropospheric eddy kinetic energy, lower-tropospheric eddy heat flux, and large-scale precipitation over the southern midlatitudes. All such fields have broad spectral peaks centered around 0.04 cycles per day, or approximately one cycle every 25 days. Even where not statistically significant, such peaks are robust and pervasive on hemispheric scales; on synoptic scales, periodicity is far less evident.

A unique line of investigation in this study was the examination of variability with time in the effect of the SBAM upon the extratropical circulation. Decadal spectra reveal statistically insignificant differences in the peak frequency and magnitude from decade to decade, likely due to sampling variability. Analysis of significant warm and cold ENSO episodes since 1979 is also inconclusive due to inconsistent event-to-event behavior and the dominating effects of sampling variability. A longer analysis period may enable future researchers to determine the interaction, if any, the SBAM may have with such long-term fluctuations as the Atlantic Multidecadal Oscillation or the Pacific Decadal Oscillation.

The primary contribution made by this study to the understanding of the SBAM was exploring the spatial variability of anomalies by way of lag-correlations. Spatial variability associated with the SBAM is most clear in analyses of upper-tropospheric EKE; both the propagation of an anomalous wave packet and its re-emergence approximately 25 days later are clearly evident in Figure 3.12. Similar but somewhat less robust structures are apparent in Hovmoeller plots of lower-tropospheric eddy heat fluxes and precipitation.

Collectively, these analyses clearly indicate the influence of the SBAM on extratropical cyclone formation and propagation in the Southern Hemisphere midlatitudes. To this point, there has been little discussion of the causes of the SBAM itself. Chapter 6 will attempt to demonstrate that such periodicity can rather simply arise from interplay between baroclinicity and eddy kinetic energy via use of a simple schematic model. While this is a new method for demonstrating the behavior of that interplay, the understanding that baroclinicity and eddies feed back on each other is nothing new: Lorenz (1963) wrote of “vacillation,” or the idea that the hemispheric wave pattern fluctuates in amplitude in time. Additionally, it has long been a principle of medium- to long-range forecasting that hemisphere-wide patterns of more active weather last for approximately 10 to 15 days, followed by a relatively quiescent period of roughly the same length. These concepts are both built upon the idea that baroclinicity requires time to “recharge” after periods of significant meridional mixing induced by eddies. It is this cycle that is the primary driver of SBAM variability.

The SH circulation was most convenient for this study, primarily because it in some ways represents a semi-idealized case: almost the entire southern midlatitudes are one continuous ocean surrounding a roughly circular ice mass centered near the pole. It is thus easier to parse out dynamics internal to the atmosphere, rather than forced by complex topographic features. However, the large majority of the Earth's human population lives in the northern midlatitudes, begging the question: is there an analogous baroclinic annular mode in the NH? At least one study to date (Thompson and Li 2015) has demonstrated that there is, albeit somewhat less robust. Chapter 4 will provide a further exploration of evidence for quasi-periodic baroclinic variability in the NH.

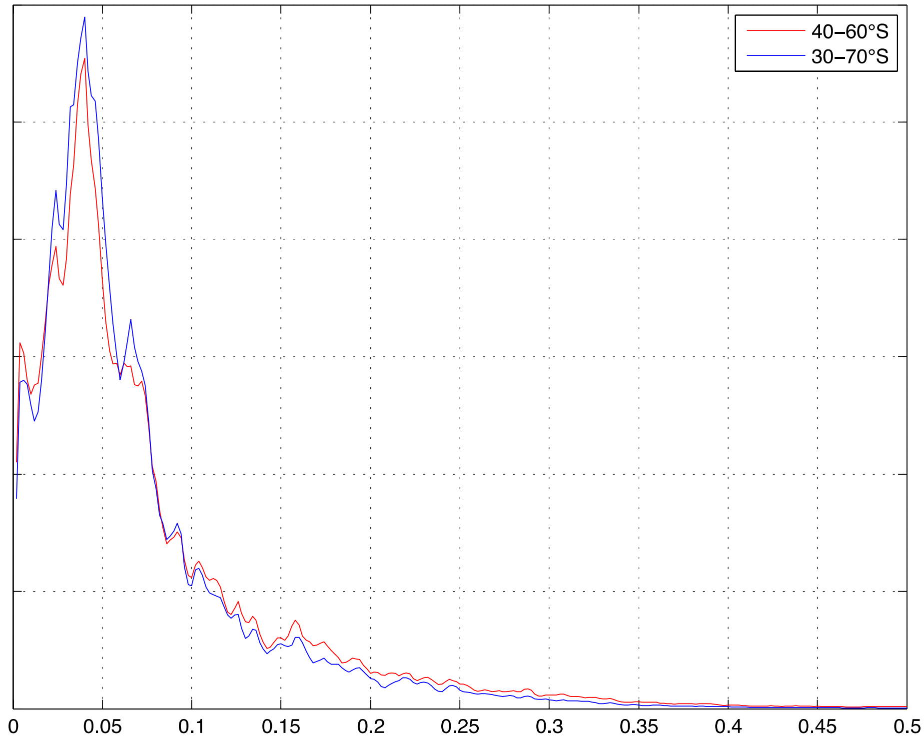

Figure 3.1. The normalized power spectrum of 300 hPa eddy kinetic energy, averaged over two distinct latitude bands. A distinct departure from a red-noise spectrum is apparent at low frequencies, with a peak power occurring around 0.04 cycles per day (or a 25 day period).

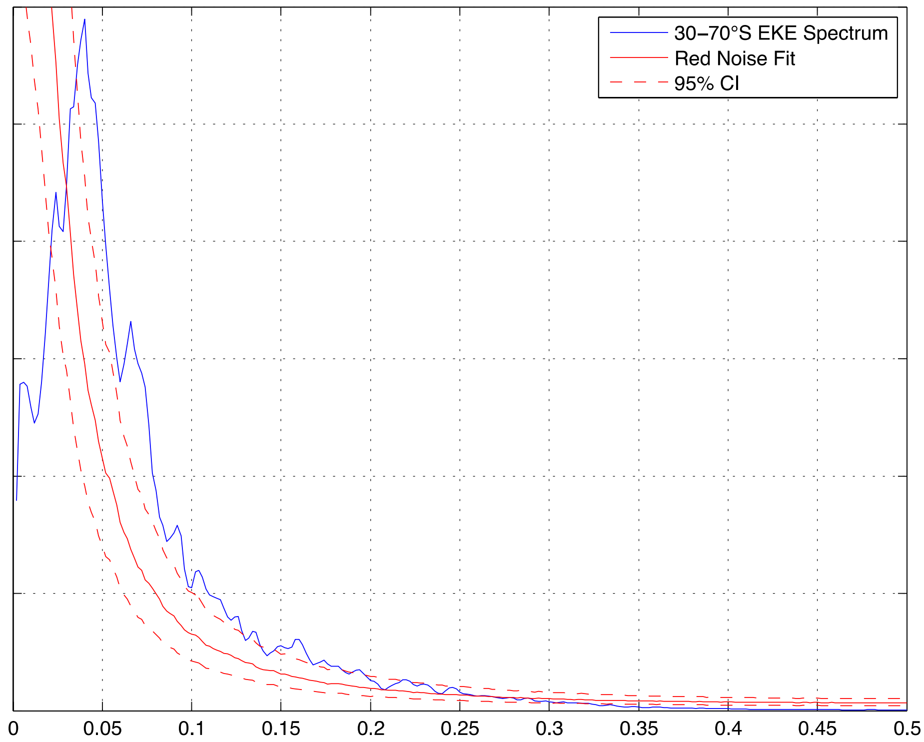

Figure 3.2. The normalized power spectrum of 30-70°S 300 hPa EKE, overlaid with a red noise hypothesis curve with 95% confidence bounds. While the red noise hypothesis is inexact, the plot illustrates the departure from typical geophysical behavior.

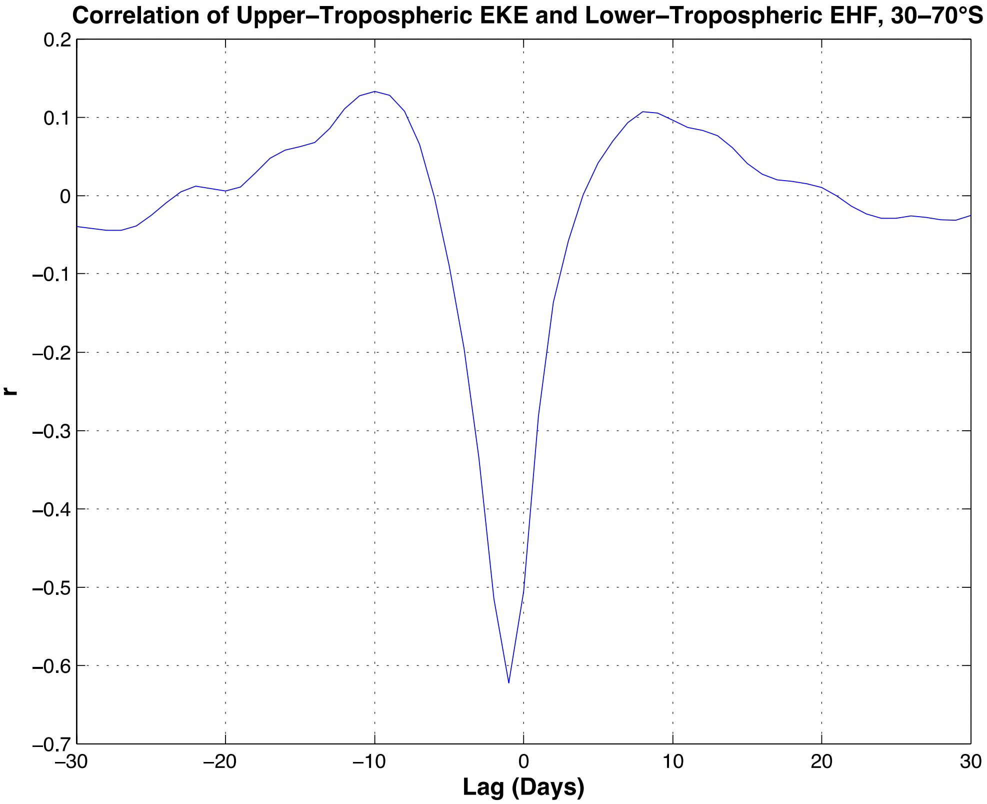

Figure 3.3. Lag-correlation of 30-70°S 300 hPa EKE and 850 hPa EHF time series. The maximum relationship between the two occurs at lag -1, or EHF leading EKE by approximately one day. Outside of lags -4 to +3, the relationship is rather weak.

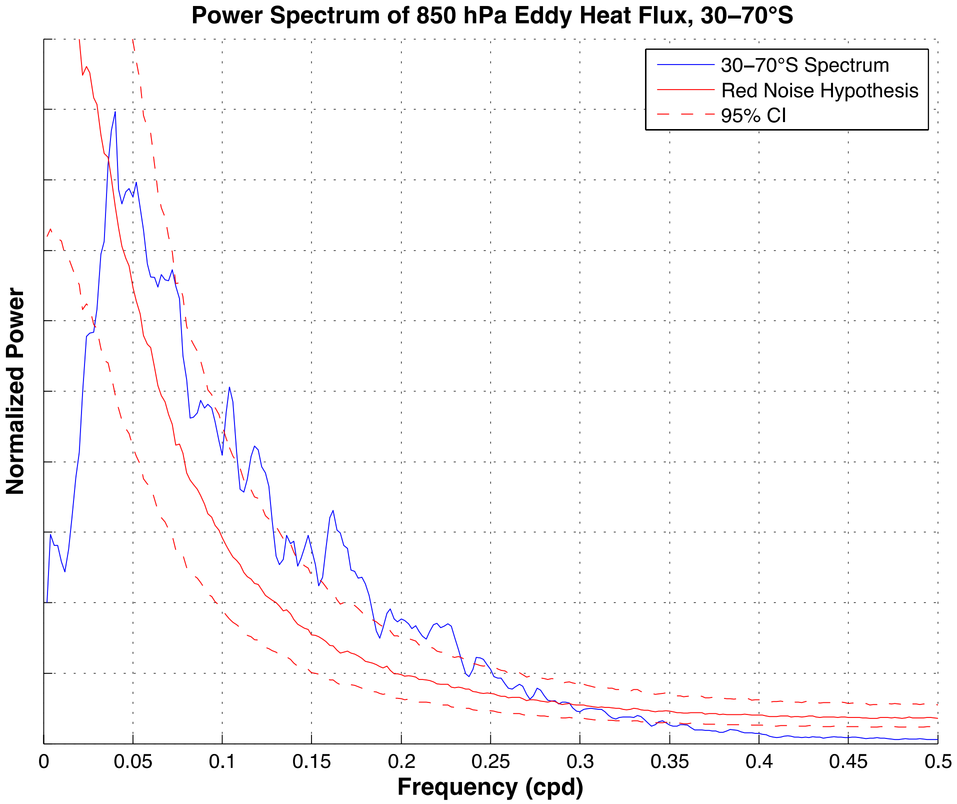

Figure 3.4. The normalized power spectrum of SH 850 hPa eddy heat flux, averaged over 30-70°S. While the spectrum appears more "red" than its eddy kinetic energy counterpart, a pronounced spectral peak still exists around 0.04 cycles per day.

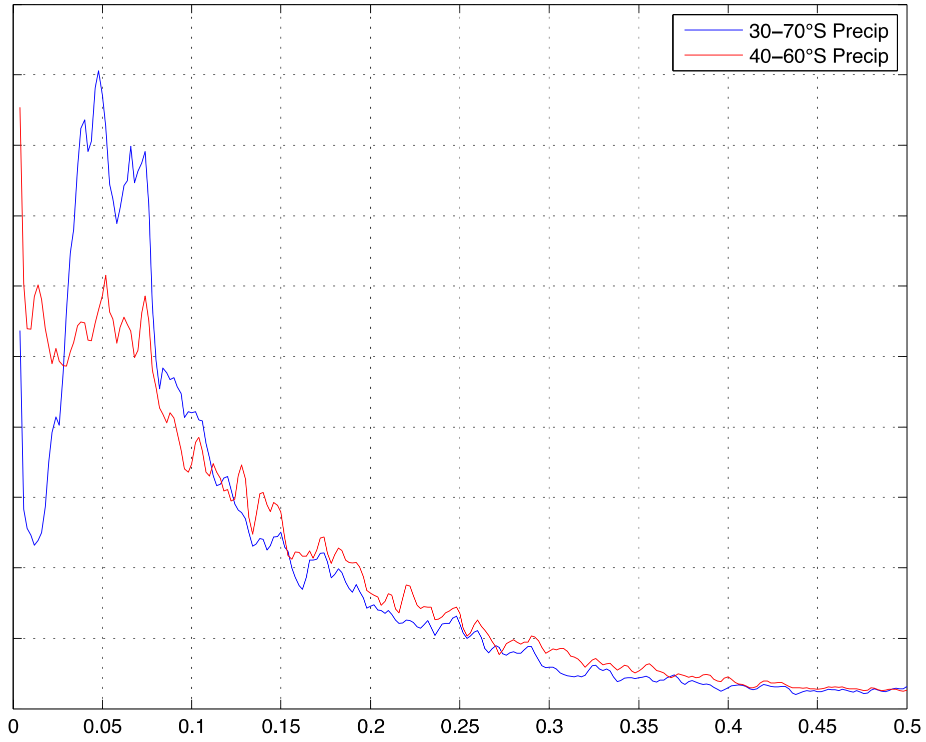

Figure 3.5. The normalized power spectrum of ERA-Interim daily large-scale precipitation, averaged over 30-70°S (blue) and 40-60°S (red). When averaging over the narrower, "storm track" focused band, no clear spectral peaks emerge; however, the broader midlatitude mean reflects the same periodicity as that observed in the EKE and EHF fields.

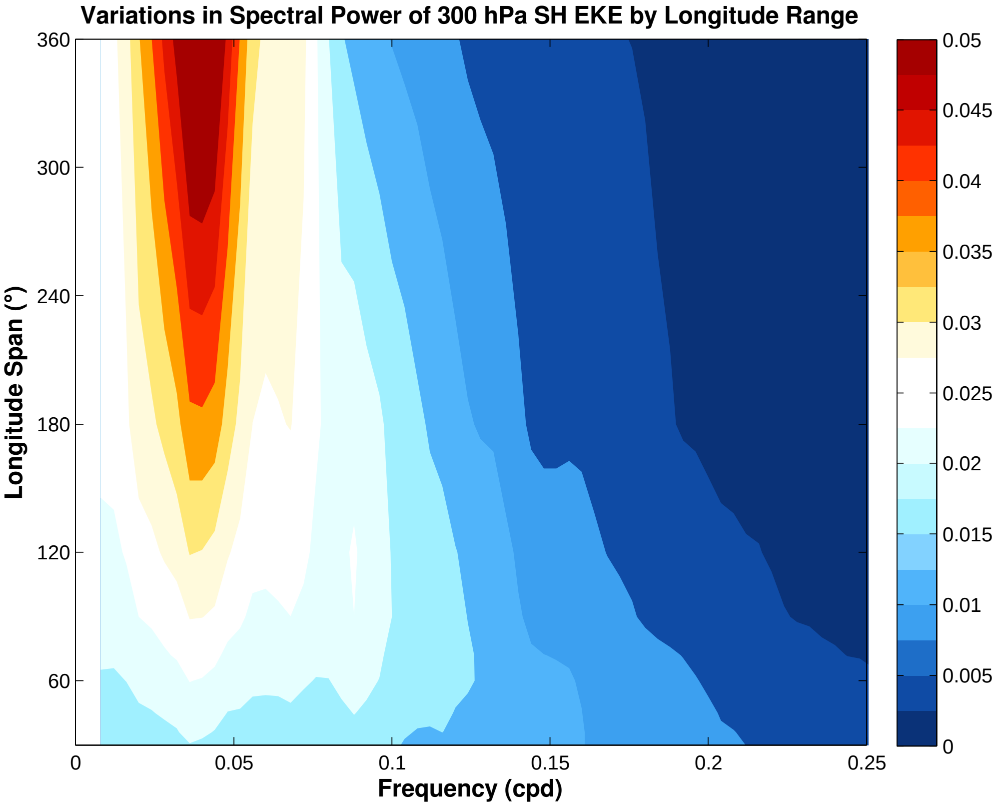

Figure 3.6. Plot of normalized spectral power at a range of frequencies by the size of the longitude span utilized for analysis. While the frequency at which peak power occurs is essentially invariant, the spectral peak becomes more and more pronounced as the averaging area is expanded.

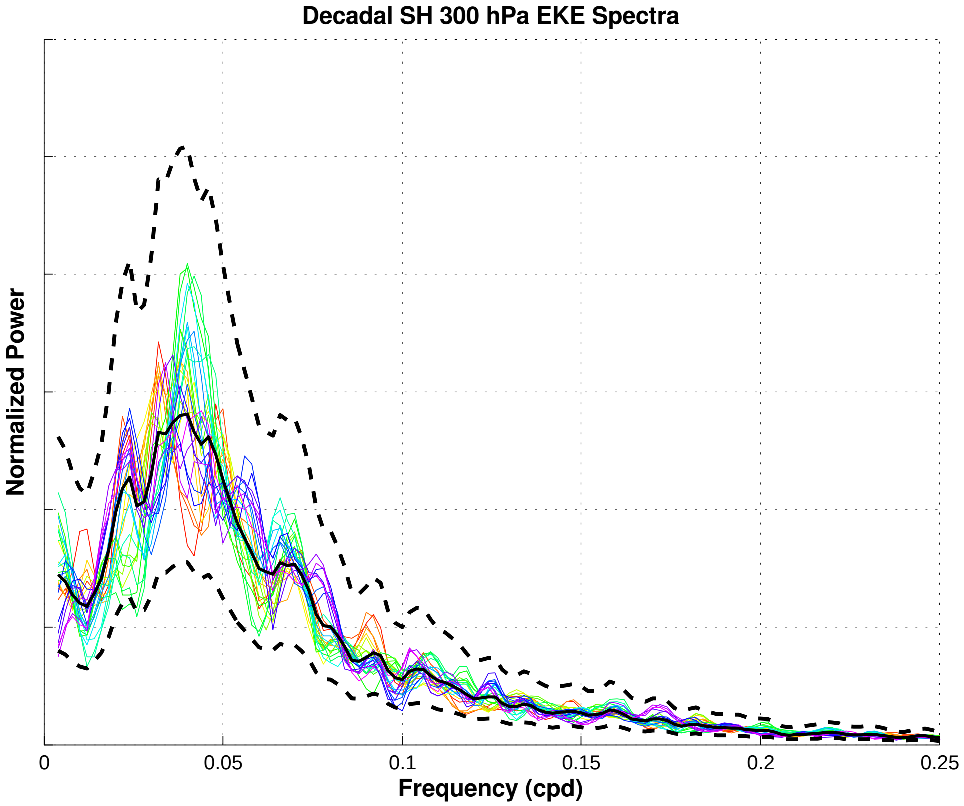

Figure 3.7. The normalized power spectra of 30-70°S EKE, broken up into decadal periods (e.g., 1979-1988, 1980-1989, etc.). The bold black line corresponds to the power spectrum of the full 36-year time series, and the dashed error bounds correspond to 99% confidence intervals for spectra of 10-year time series. All other curves represent mean spectra from each 10-year period.

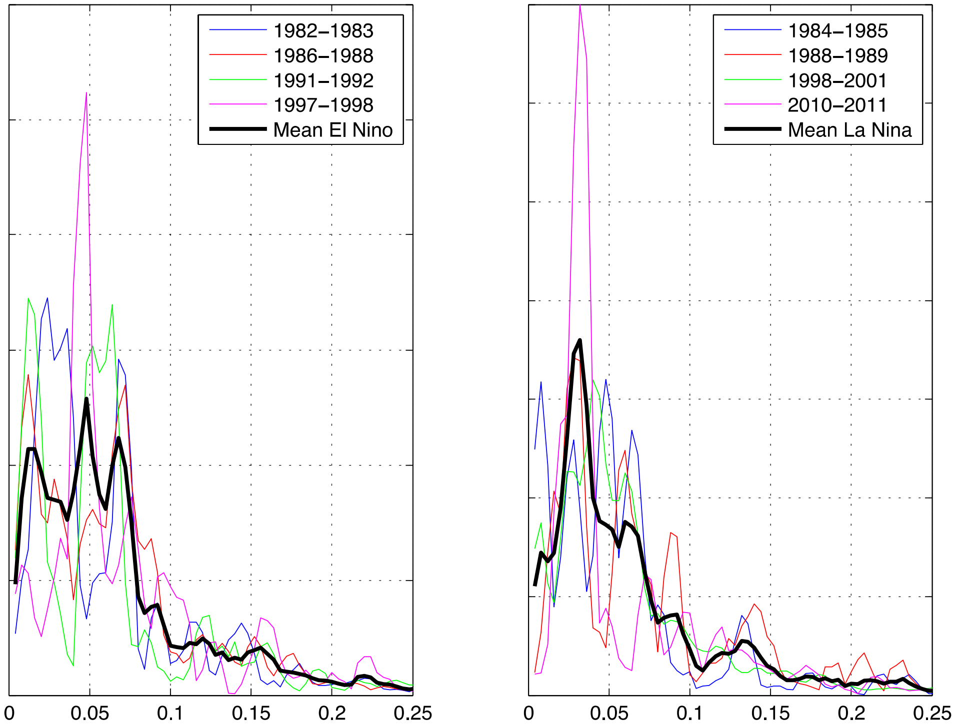

Figure 3.8. Normalized power spectra of major El Nino and La Nina episodes during the ERA-Interim analysis period (1979-present).

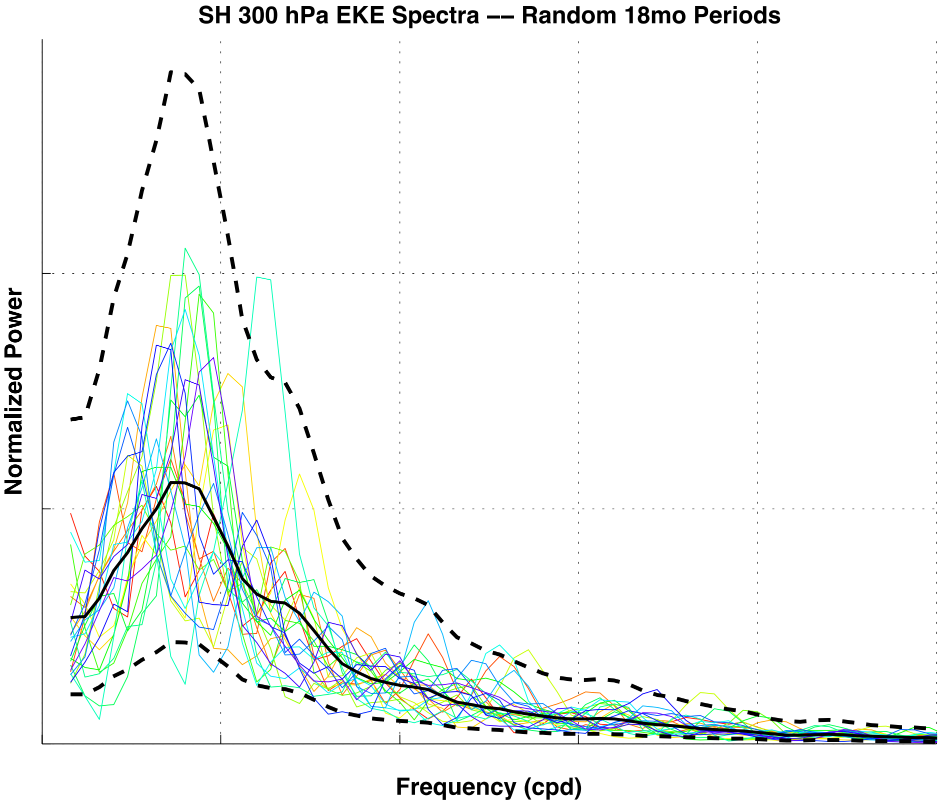

Figure 3.9. Normalized power spectra of 30-70°S EKE anomalies for all distinct 18-month periods in the 1979-2014 analysis period. The solid black line represents the mean of all 18-month power spectra and the dashed black lines indicate the 99% confidence interval based on the F-statistic.

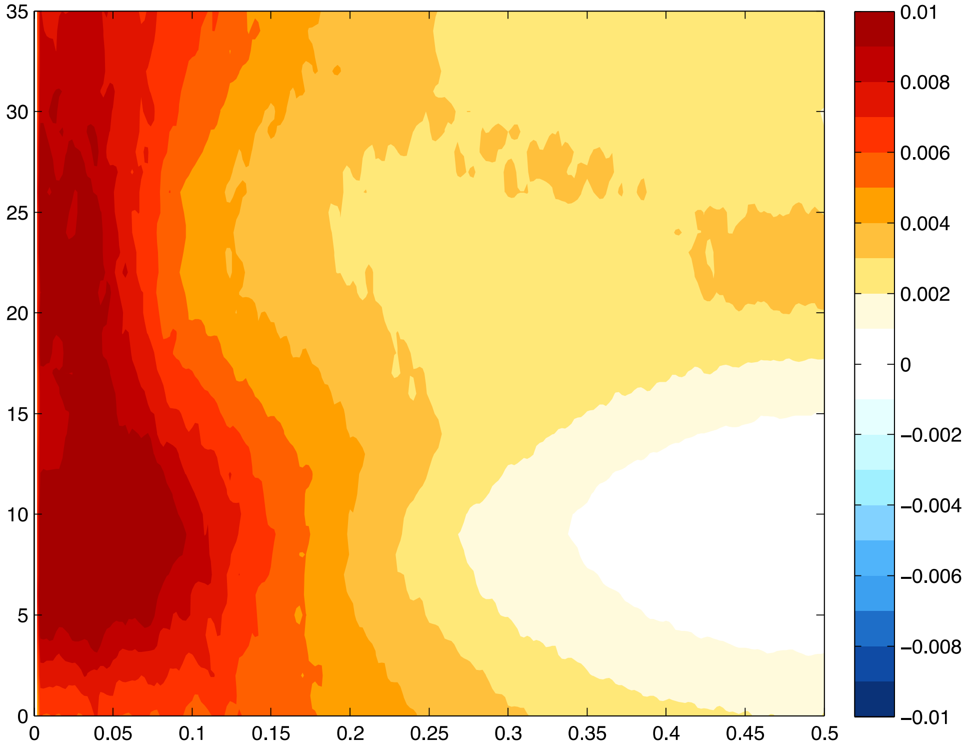

Figure 3.10. How normalized spectral power varies for 40-60°S 300 hPa EKE time series constructed by starting at a point and following the flow at the rate given by the y-axis. Spectral power is most robust around 0.04-0.05 cycles per day and at flow speeds of approximately 5 to 12 m/s.

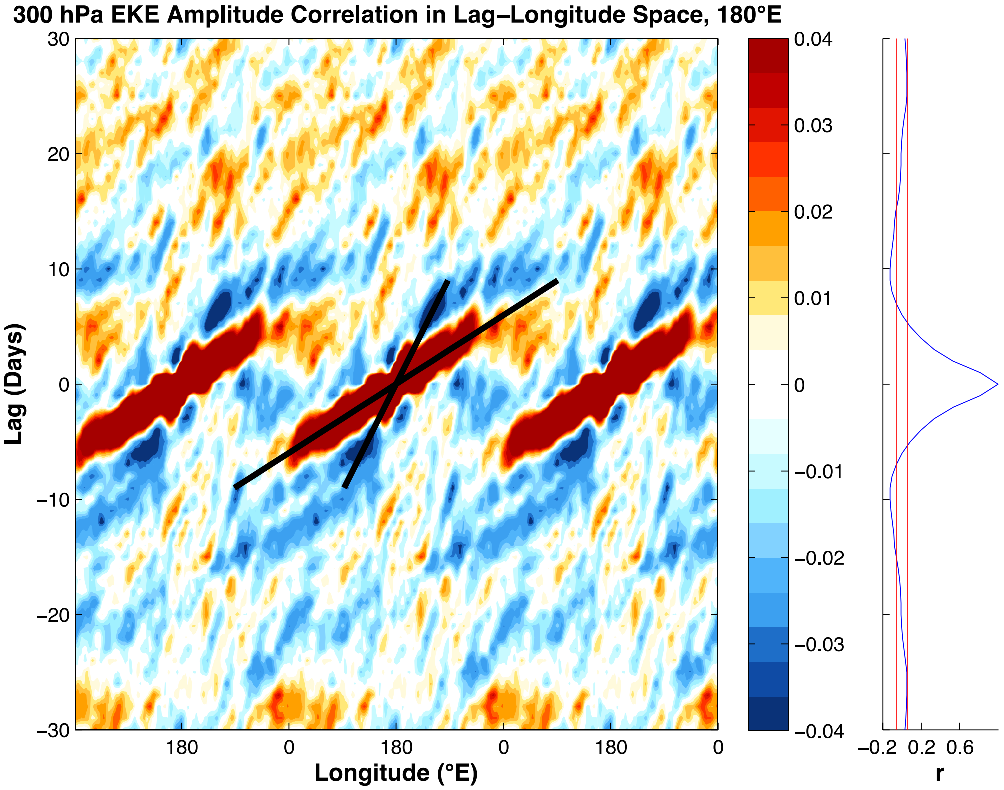

Figure 3.11. (Left panel) Variations in correlation by longitude and lag for SH 300 hPa EKE. The two black lines represent propagation rates of 8 m/s (steep) and 25 m/s (shallow), indicative of the approximate speeds at which wave phases and wave packets travel, respectively. The plot is based on lag-correlations with a 20° latitude band average over 40-60°S centered on 180°E. (Right panel) Autocorrelation sequence for 40-60°S mean 300 hPa EKE with 95% confidence bounds in red.

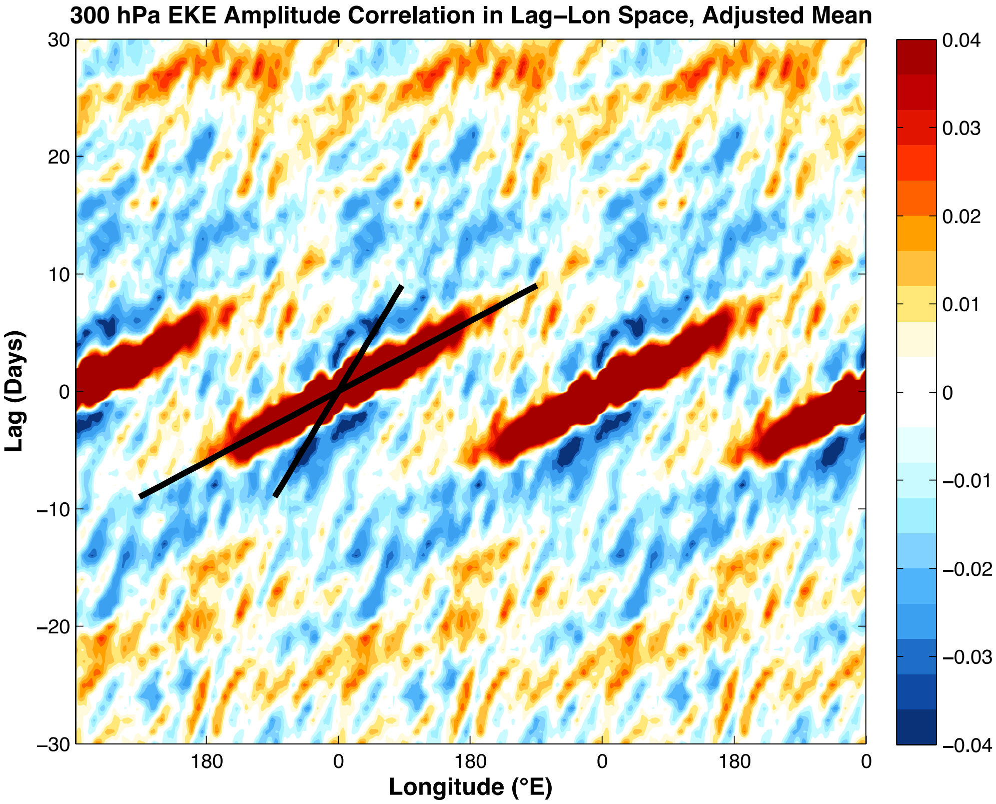

Figure 3.12. As in Figure 3.11, but for a mean of all lag-longitude correlation maps, centered on the same point (0°E). The maps are largely similar, but some of the variable noise has been smoothed out in this average.

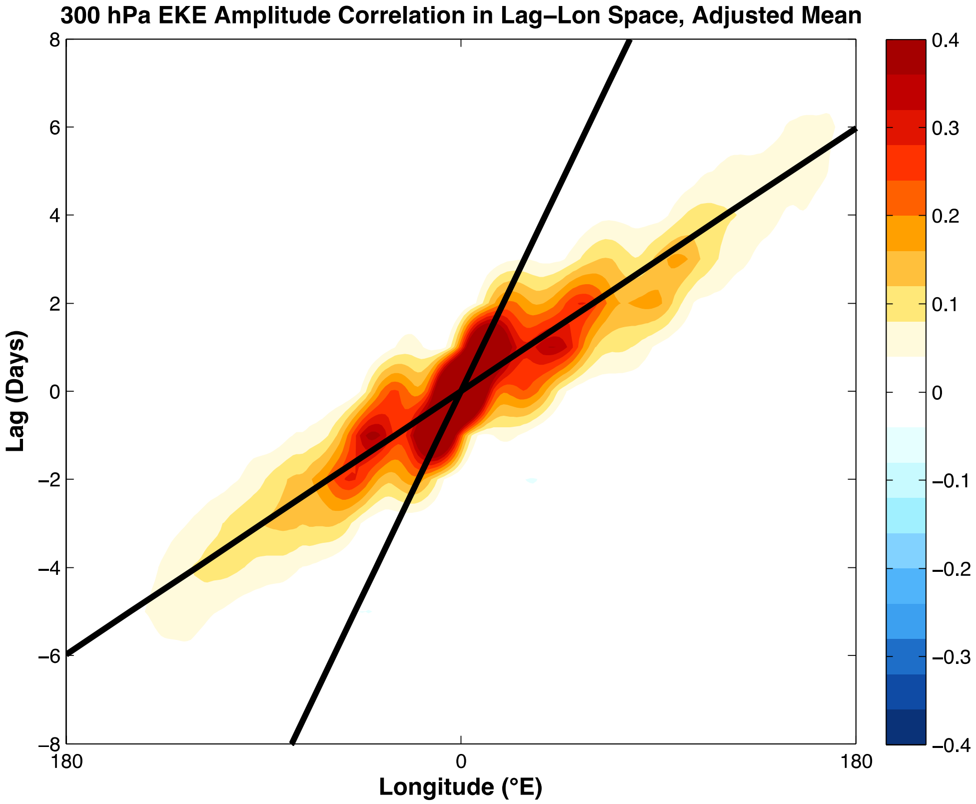

Figure 3.13. The same lag-correlations as in Figure 3.12, but with a greatly expanded color scale to reveal the detail within the color-saturated regions on previous plots. Individual wave phases can now be seen as parallel regions of high correlation, propagating at approximately the phase speed estimate (steep black line) of 8 m/s.

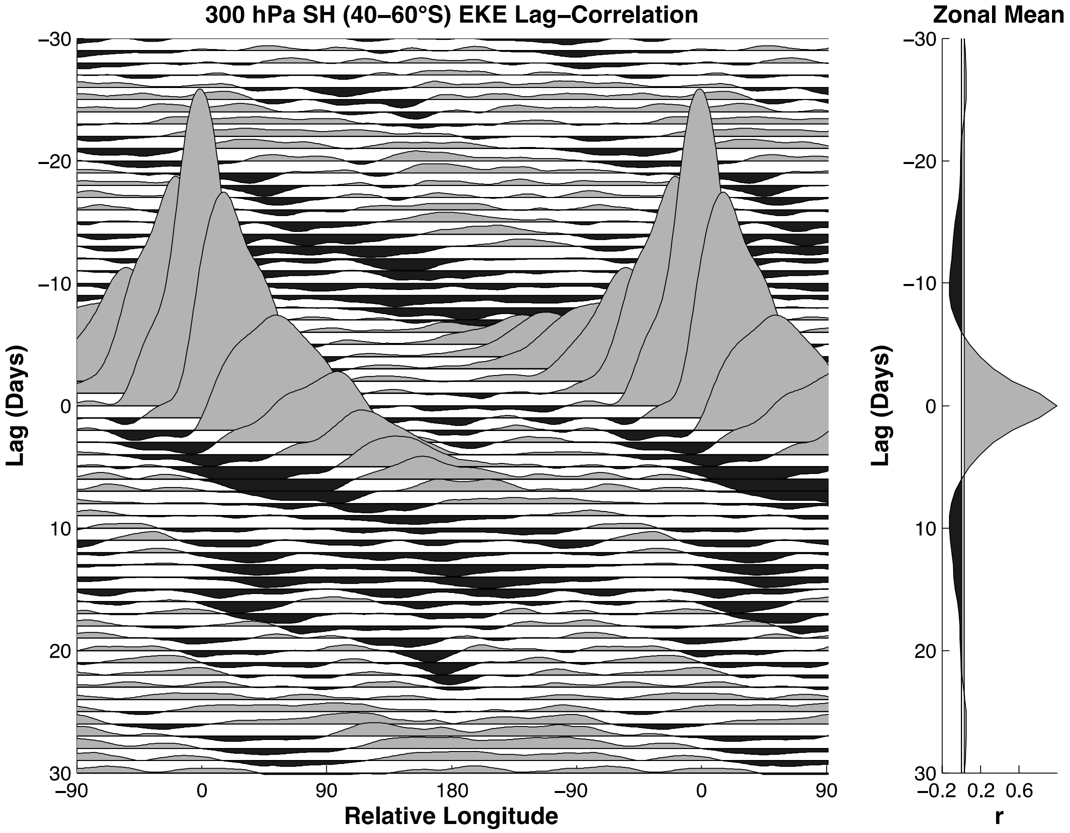

Figure 3.14. A plot of lag-correlations of 300 hPa 40-60°S EKE, but visualized as curves at single lags rather than a filled contour plot. These correlations are calculated as 30° longitude running means. Note the emergence of negative correlations to the east of the original longitude, as well as the re-emergence of positive correlations around day 25.

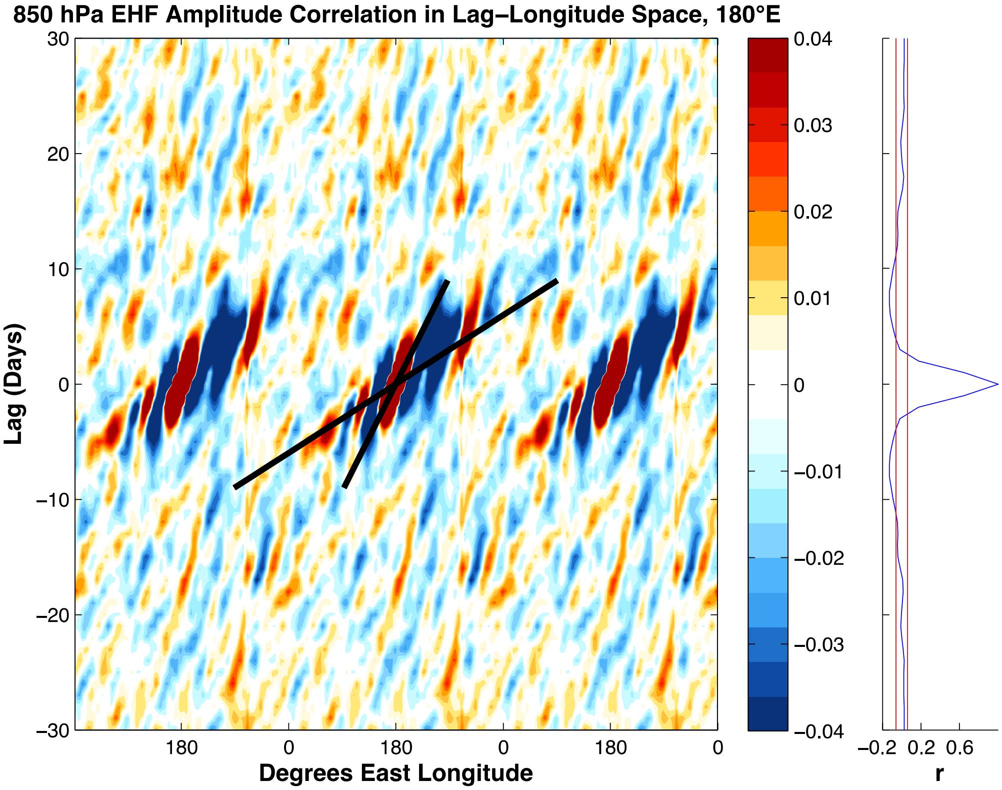

Figure 3.15. (Left panel) As in Figure 3.12, but for 850 hPa eddy heat flux anomalies. Note the alternating couplets of high and low correlation, which is a product of the sign reversal of heat fluxes on the east and west sides of lower-tropospheric extratropical cyclones. (Right panel) Autocorrelation sequence of 40-60°S mean 850 hPa EHF.

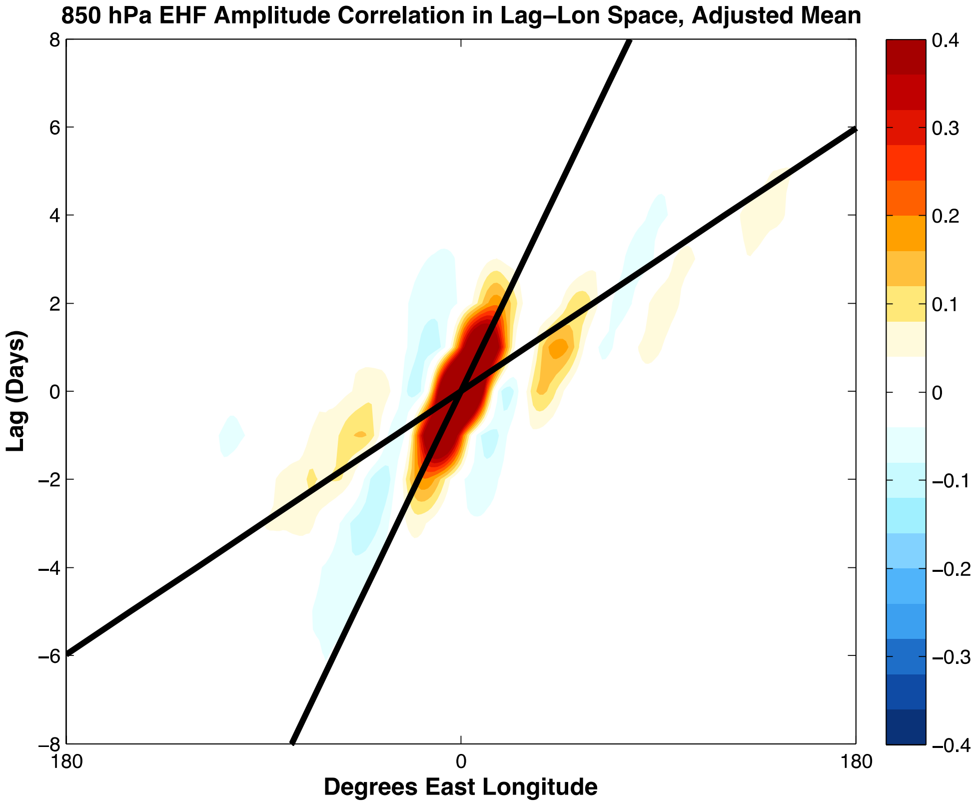

Figure 3.16. As in Figure 3.15, but without color saturation of the main wave packet. The alternating positive and negative correlations can be seen clearly for multiple wave phases within the core packet.

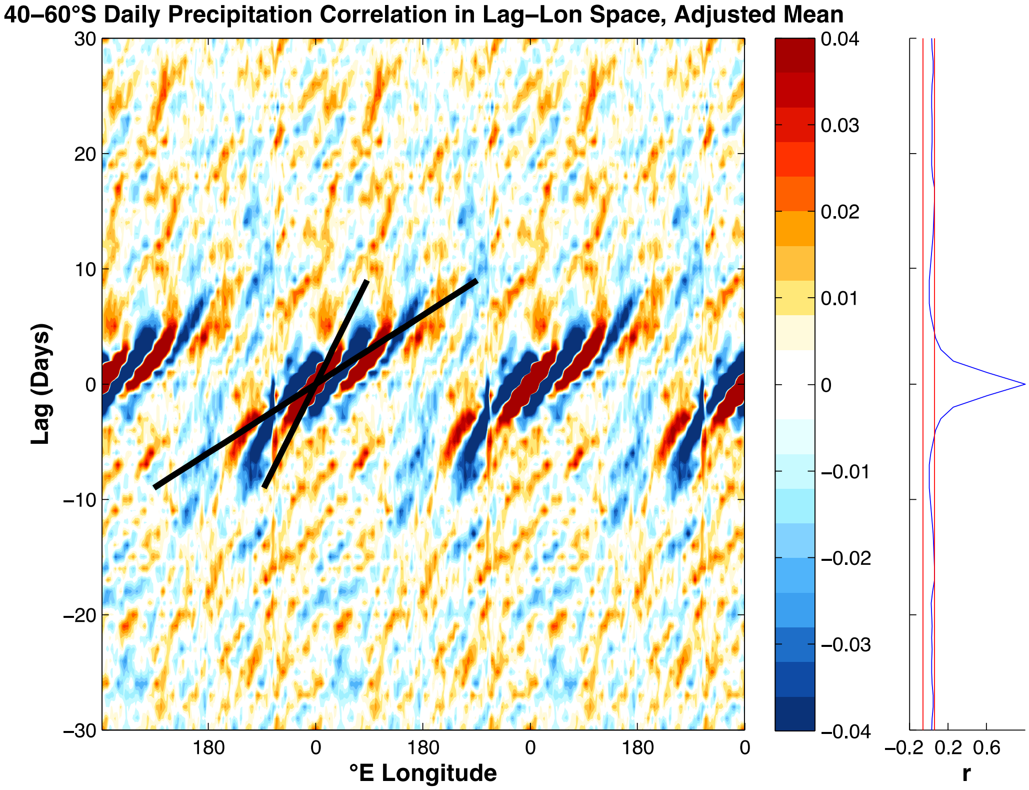

Figure 3.17. (Left panel) Lag-correlation Hovmoeller plot of 40-60°S mean "large-scale precipitation" field from ERA-Interim, averaged over all base longitudes. Like in the EHF Hovmoeller, alternating couplets of high and low correlation are present within the main wave packet due to the differing upstream and downstream effects of waves upon precipitation. (Right panel) Autocorrelation sequence of 40-60°S mean precipitation anomalies.

CHAPTER FOUR

OBSERVATIONS OF QUASI-PERIODIC BEHAVIOR IN THE NORTHERN HEMISPHERE

The Southern Baroclinic Annular Mode is a powerful modulator of extratropical cyclone activity in the SH, revealed as robust quasi-periodicity in large-scale averages of eddy kinetic energy, eddy heat flux, and precipitation. Previous studies have demonstrated that an analogous signal, the Northern Baroclinic Annular Mode, exists in the NH, but it is considerably less robust than its SH counterpart (Thompson and Li 2015). This chapter will present some analysis on the longitudinal structure of the NBAM and explore its contrasts with the SBAM (Section 4.1). Such comparisons are intended to determine what lessons from studying the SH phenomenon can be applied to the NH.

4.1 Spectral Analyses

As alluded to in previous chapters, considerable differences exist in the behavior of the BAM across the hemispheres. Much of this difference can be ascribed to the differences in land-sea distribution and the consequent zonal contrasts in baroclinicity. Overall, the NBAM signal appears less robust than the SBAM, but there is still reason to believe it has significant modulating effects on NH extratropical cyclone activity. The spectral (section 4.1) and lag-correlation (section 4.2) analyses presented here will attempt to demonstrate this significance.

Much like the investigation of the SBAM conducted in Chapter 3, the exploration of the NBAM begins with a spectrum of upper-tropospheric (300 hPa) EKE (Figure 4.1). As mentioned in the introduction, the periodicity of the NBAM is not particularly clear; the spectral “peak” bears more of a resemblance to a bump in a hypothetical red noise spectrum. The likeliest explanation for this departure from the observed behavior in the SH is that standing waves and planetary waves constitute a greater proportion of upper-tropospheric waves in the NH, largely due to the presence of complex topography.

Planetary waves have preferred residence locations downstream of the topographical features that force them, and they frequently exert their influence on extratropical cyclone development. They therefore give rise to EKE anomalies that are not as affected by the fluctuations of the BAM as in other regions. In order to isolate the effects of the NBAM on the NH circulation, it was therefore necessary to filter planetary waves (typically wavenumbers 3 and below) from the EKE data. Filtering is accomplished by expanding the raw, 6-hourly U and V fields into their Fourier harmonics in the zonal (x) direction. Harmonics 0-3 are then removed, resulting in wavenumber-filtered, zonally anomalous U and V (harmonic zero corresponds to the zonal mean). EKE is then calculated in standard fashion from these fields. The resulting spectrum (Figure 4.2) bears a much stronger resemblance to that of the SH EKE spectrum (Figures 3.1 and 3.2), with a robust peak in power residing around the requisite 0.04 cycles per day. Note that the wavenumber filtering not only enables the BAM periodicity to emerge more clearly, but it also shifts the peak frequency to a slightly higher value. This shift is perhaps reflective of the removal of lower-frequency variability associated with planetary waves.

Power spectra of eddy heat fluxes in the NH also appear different than their SH counterparts (Figure 4.3). In both wavenumber-filtered and unfiltered data, a double-peak structure is present; the peak common to both occurs at around 0.04 cycles per day. While this frequency is roughly consistent with the BAM periodicity, the origin of the higher-frequency peak in the unfiltered curve appears to be related to planetary wave activity, since it is largely eliminated in the filtered spectrum. This result stands in contrast to the results from EKE, in which apparent planetary wave influences resulted in lower-frequency variability. However, the filtered spectrum also introduces a peak at very low frequencies for which there is no obvious explanation.

If the periodicity of the BAM is significantly obscured in NH spectra of unfiltered EKE and EHF, this problem is even more pronounced in spectra of large-scale precipitation. While the general shape of the power spectrum implies a very broad concentration of frequencies centered around 0.05 cycles per day, solitary frequencies fail to emerge (Figure 4.4). One significant similarity across the hemispheres is the greater strength of the signal in the broader 30-70°N latitude band than in the 40-60°N band; however, enough noise is present that this may not be a robust feature. Once again, the effects of topography can be invoked here as a likely explanation.

Complex topography has two notable effects: it introduces substantial inhomogeneities in precipitation, EKE, and EHF patterns across the hemisphere, and it means that deep moist convection makes up a substantial fraction of all precipitation over large (primarily continental) portions of the hemisphere. As a result, any periodic behavior induced by the BAM is diluted by precipitation produced on local scales, often unassociated with extratropical cyclones. The magnitude of this effect should be reduced by the use of the large-scale 1.5°x1.5° grid, but convective aggregation and upscale growth do frequently produce large-scale precipitation events over continental regions such as the central United States. Such factors, along with the overall less robust periodicity in cyclone activity in the NH, help explain the observed discrepancies. Favored locations for increased baroclinicity along coastlines and mountain ranges may also affect the observed EHF and EKE anomalies around the hemisphere, thereby obscuring the periodicity of the BAM. Such regional inhomogeneities will be further explored in Section 4.2.

4.1.1 Spectra at smaller spatial scales

Clearly, the zonal asymmetries introduced by complex topography in the NH have considerable effects on the emergence of periodic signals. As seen in Chapter 3, however, sub-hemispheric means are too noisy and dependent on local effects. In the much noisier NH, this result holds true as well, even over the hemisphere's storm tracks. In each of the Atlantic and Pacific storm tracks, significant periodicities fail to arise in the unfiltered 300 hPa EKE data (not shown).

However, once wavenumber filtering has been applied, clear BAM periodicities emerge in the North Pacific and North American sectors (Figure 4.5), although surprisingly not in the Atlantic storm track region. With the influence of planetary waves removed, an explanation for this absence in the North Atlantic is not obvious. The main driver of baroclinicity in the northwest Atlantic is the temperature gradient between the Gulf Stream and the eastern portion of continental North America; perhaps there is another forcing agent responsible for lower-frequency variation in this region.

While it has been demonstrated that taking zonal means throughout the entire NH is generally ineffective at isolating the effects of the BAM, the appearance of periodicity on synoptic scales can still be examined by repeating the analysis used for Figure 3.6 in the previous chapter. First, a longitude-mean array was calculated over the 40-60°N latitude band. Next, various longitude spans from 45° up to 360° were averaged to time series, which then underwent spectral transformation. Base longitudes spanning the entire globe were selected for each span and their spectra were averaged together, giving a single result for each size of longitude range. The resulting plot illustrates the decay of the BAM signal with spatial scale (Figure 4.6).

Whereas a purely red noise spectrum would have monotonically decaying power from high to low frequency, the BAM spectrum stands out as a separate peak around 0.04 cycles per day. This feature is evident for longitude spans greater than approximately 210° in the NH, but becomes approximately red on smaller scales. Such a result is consistent with other results suggesting a reduced prominence of the BAM signal, since the SH plot indicated that the BAM could be clearly seen down to at least 120° spans. Thus, certain sectors of the NH retain clear influence from the BAM on smaller scales, whereas over the entire hemisphere, periodic behavior is much less identifiable.

4.1.2 Spectra following atmospheric motion

Another useful device for examining how the BAM periodicity emerges is to consider spectra calculated from time series following atmospheric flow. Figure 4.7 is based on assembling time series by choosing the longitude closest to where a parcel advected at the specified rate would be on each day. This method shows that, like in the SH, the most robust periodicity appears at flow rates near and slightly greater than the phase speed, but significantly less than the group velocity (peak power around 0.03-0.04 cycles per day occurs between 3 and 7 m/s, versus a phase speed of 5 m/s and group velocity of 24 m/s). As in the SH, this has to do with where the negative anomalies develop: the strongest negative EKE anomalies trail the anomalously positive wave packet, thus leading to an “offset” that is neither stationary nor moving at the speed of the wave packet. The lag-correlation analyses that follow will more effectively illustrate the spatial structure of the NBAM.

4.2 Lag-Correlation Analyses

Given the substantial differences in spectra that were discussed in the previous section, it should come as no surprise that the spatial structure of the BAM is quite different in the NH as well. The most useful tool for diagnosing this structure is the lag-correlation Hovmoeller diagram (Figure 4.8). Each panel of the diagram is constructed by correlating 40-60°N mean 300 hPa EKE anomalies at a given longitude with all other longitudes at lags from -30 to +30 days. The resulting plot illustrates longitudinal variations in anomaly correlations with time, essentially outlining how correlated features (i.e., wave packets and wave phases) propagate in time and space. Our discussion of this figure will begin with the analysis in the left panel, which shows the lag-correlations for the full, unfiltered EKE anomaly field.

Along an axis of 20 m/s mean motion (shown by the bold black line of shallower slope), a region of statistically significant positive correlations track eastward in time from around day -8 to day +4. This feature corresponds to the track of the primary wave packet of interest. Notably, the correlations retain their significance for a much shorter time than seen in the SH. Additionally, a spike of positive correlations extending from lags -15 to +15 can be seen residing at the original base longitude, consistent with influences from large-scale stationary waves that dominate certain regions of the hemisphere. The correlations associated with an individual wave phase can be seen by tracing along the 5 m/s line (steeper), although the exact propagation rate is hard to determine with such a large stationary wave component.

As with the spectral analyses, isolating the effects of the BAM requires filtering out the dominating influence of planetary waves. Utilizing the same EKE data as in the wavenumber 4+ filtered spectra, the lag-correlation analysis was repeated to produce the right-hand panel of Figure 4.8. With the stationary waves removed, the correlations associated with both the central wave phase and the wave packet become far clearer. The group velocity has also ticked up somewhat from what is seen in the all-wavenumbers analysis, with the best fit line following a propagation rate of approximately 24 m/s. This difference is likely due to the removal of quasi-stationary waves (i.e., waves that propagate at speeds near 0 m/s), resulting in a higher mean eastward propagation rate.

Another way of visualizing this propagation is seen in Figure 4.9, which simply plots the correlations across all longitudes at each lag as individual curves. The motion of the main wave packet (positive correlations, filled in light grey) can be traced to the east as time moves forward, with negative anomalies beginning to fill in by day ~6 at longitudes slightly lagging the motion of the original anomalous packet. This offset between where the positive anomalies propagate and decay and the negative anomalies grow gives rise to the intermediate speed at which the BAM periodicity is most apparent in flow-following spectra (see again Figure 4.7).

Even with planetary waves filtered from the EKE data, the substantial topographical asymmetries of the NH are still culpable in producing zonally asymmetric EKE anomalies. That is, certain longitudes correspond to “storm track” regions, where baroclinic contrasts between continental regions and oceanic regions produce frequent and robust extratropical cyclones. It is therefore of interest to examine the lag-correlation structure of EKE anomalies in the storm track regions in isolation.

Qualitatively, the Hovmoeller diagrams of EKE anomaly correlations for the Atlantic (Figure 4.10, left panel) and Pacific (right panel) storm tracks resemble that of the zonal-mean diagram, albeit with considerably greater noise. Interestingly, both seem to also fit well with the assumed phase speed and group velocity of 5 m/s and 24 m/s, respectively (not shown). Of interest are the weaker upstream correlations, consistent with the idea that the chosen longitudes are frequently in or near the preferred region for cyclogenesis, and there are not necessarily antecedent waves upstream.

4.3 Summarizing Remarks

Clearly, the observable effects of the BAM in the NH are more subtle and nuanced than those in the SH. The presence of two distinct, basin-specific storm tracks and topographically-induced planetary waves that preferentially reside in specific regions significantly obscure the variability induced by the BAM and make detecting the quasi-periodicity associated with it more difficult. Filtering out wavenumbers 0-3 significantly clarifies the BAM signal, but even then it lacks the robustness of its SH counterpart. Given the difficulty in linking even the periodicity of the SBAM to observable shifts in weather, it seems even less likely that the NBAM can be exploited as a predictive indicator of regional weather patterns.

If the BAM is indeed an inherent property of a baroclinic atmosphere, some facsimile of the observed quasi-periodic behavior should exist in sophisticated climate models. This possible implication then gave rise to several other questions: are simple GCMs capable of reproducing the periodicity of the BAM? Are moist processes necessary to produce the BAM? Does the BAM appear in baroclinic atmospheres that are devoid of land-sea contrasts and other surface inhomogeneities? These questions will be answered in the following chapter by employing two types of GCMs: the grey-radiation aquaplanet model and the GFDL dry dynamical core.

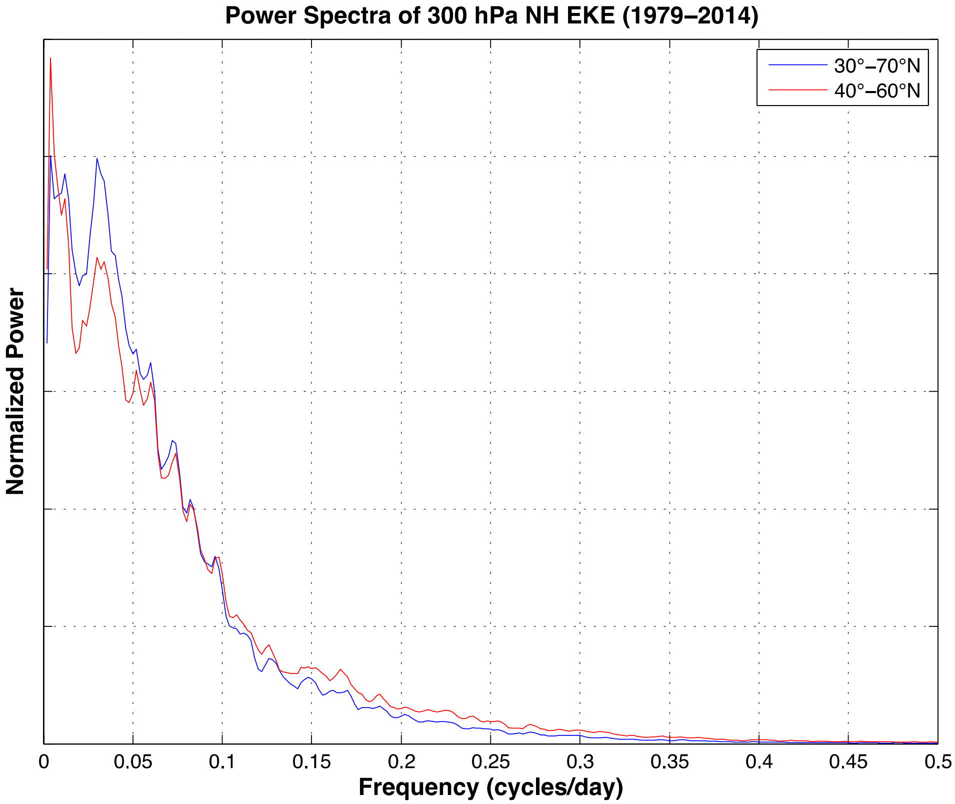

Figure 4.1. Power spectrum of 300 hPa EKE averaged over the two NH latitude bands described in the legend.

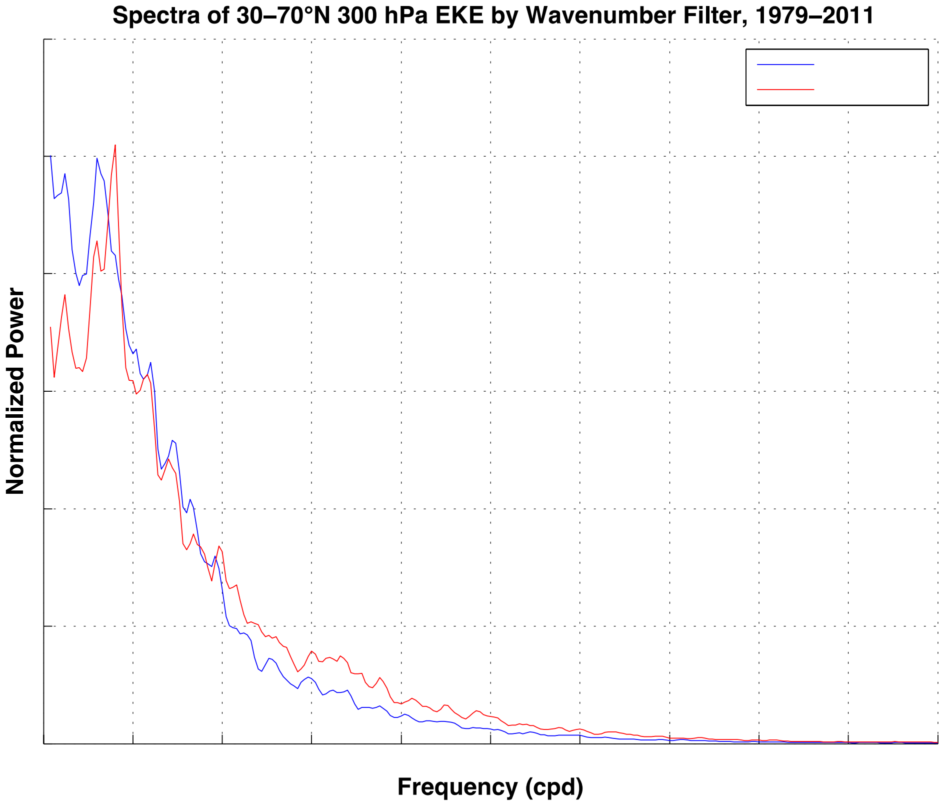

Figure 4.2. Power spectra of 30-70°N 300 hPa EKE anomalies for both unfiltered and wavenumber 4+ data. The blue curve is a reproduction of the blue curve in Figure 4.1, whereas the red curve is calculated from data for only wavenumbers 4 and higher.

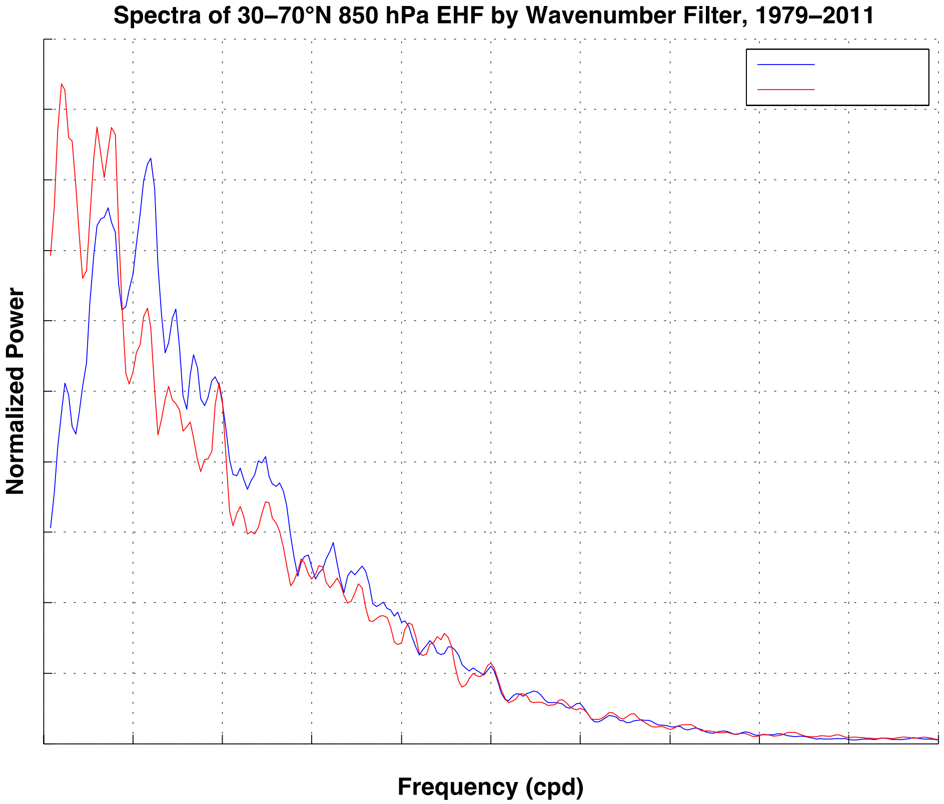

Figure 4.3. Power spectra of 850 hPa eddy heat flux anomalies over 30-70°N for both unfiltered and wavenumber 4+ data.

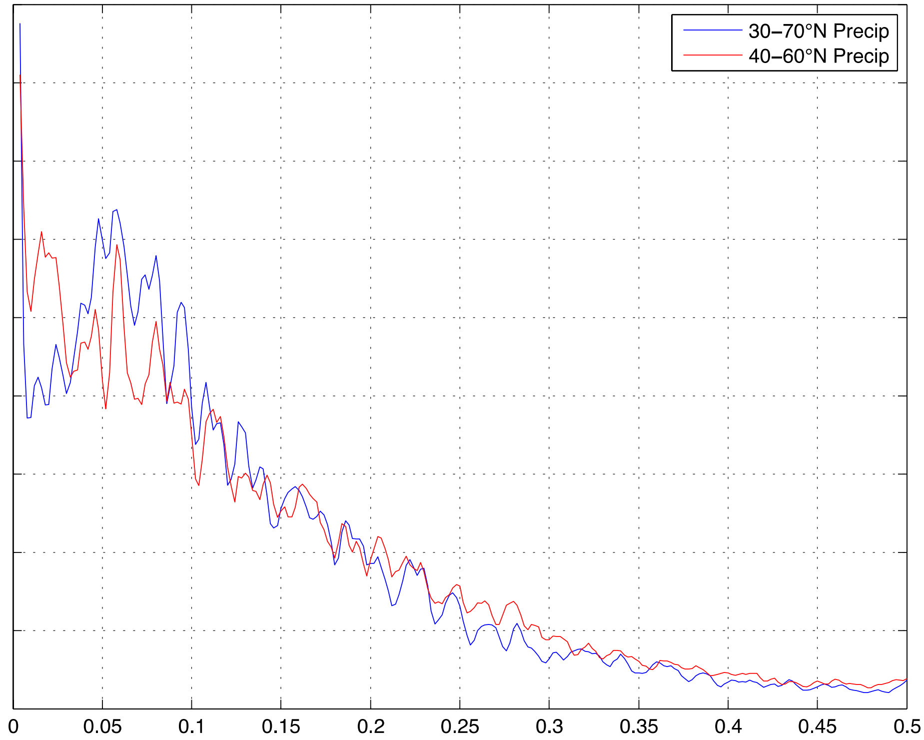

Figure 4.4. Power spectra of total daily precipitation anomalies based on the ECMWF model's 12-hour forecasts interpolated to a 1.5°x1.5° grid.

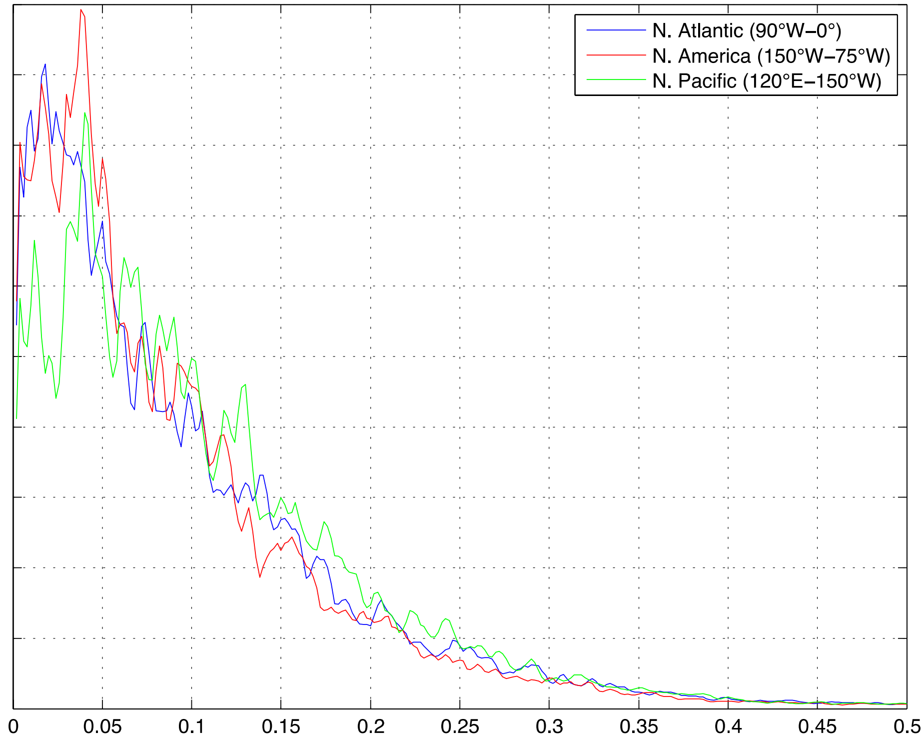

Figure 4.5. Power spectra of wavenumber 4+ filtered mean 300 hPa EKE over the longitude ranges specified in the legend. Each spectrum is representative of a distinct geographical region of the NH.

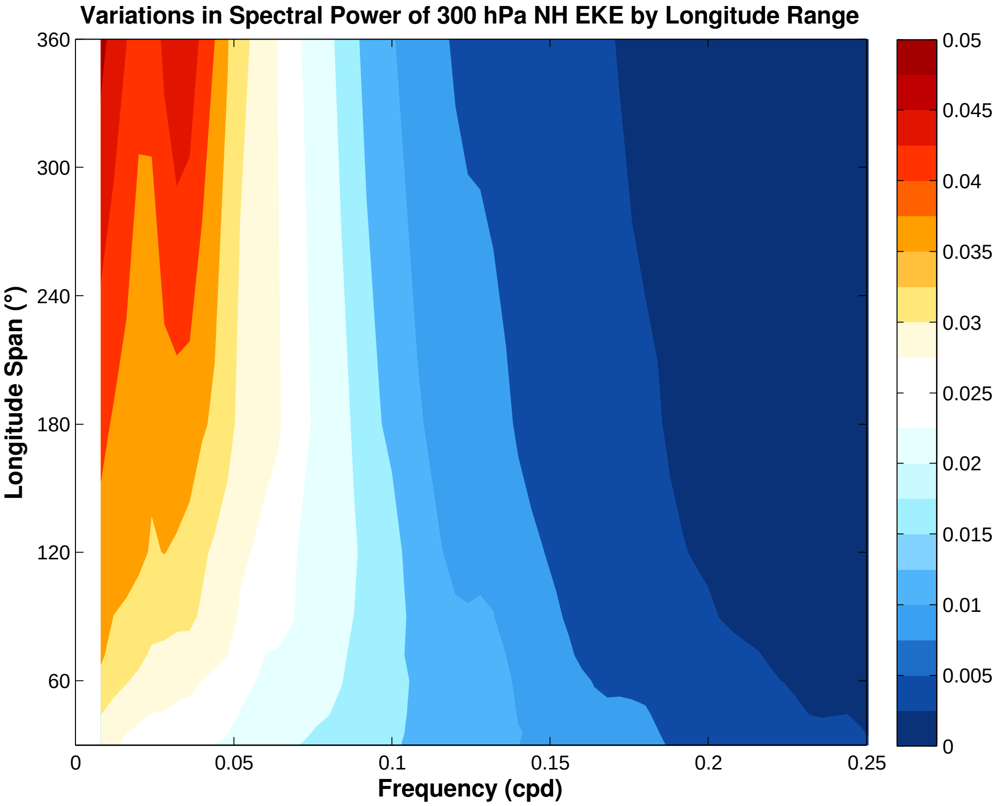

Figure 4.6. The variability of spectral power as a function of both frequency and longitude span for 300 hPa NH EKE averaged over 40-60°N. Note that a perfectly red noise spectrum would have monotonically decaying power from low to high frequencies, a result which is largely mirrored here.

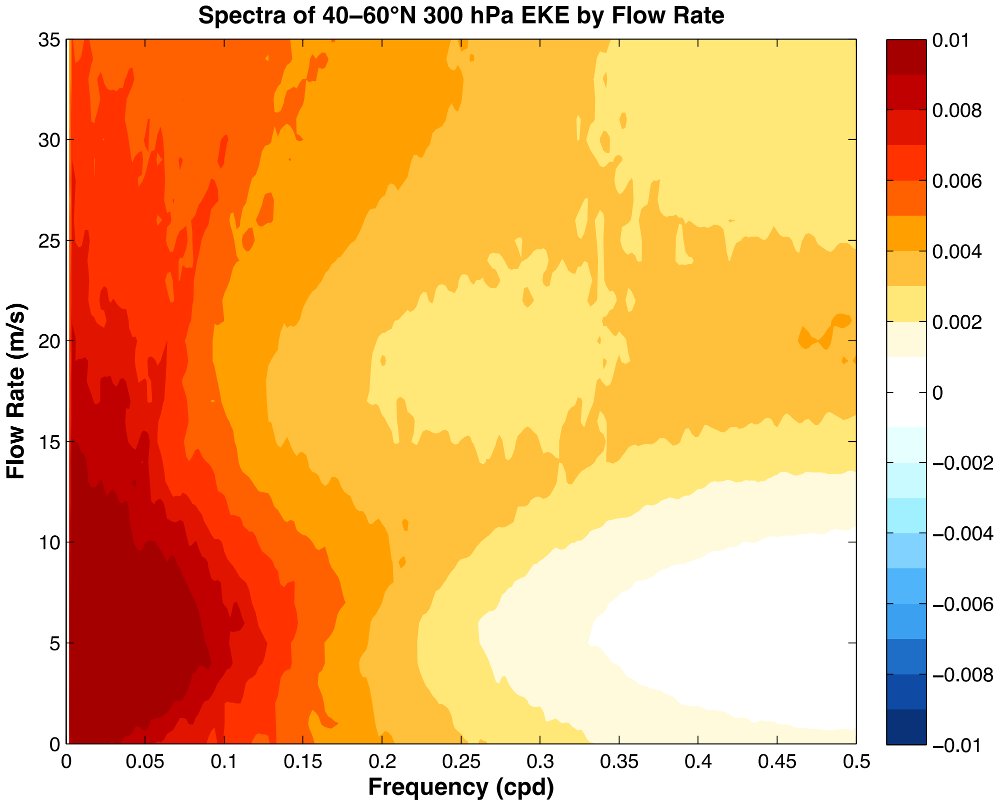

Figure 4.7. The variability of spectral power of 300 hPa EKE over 40-60°N and 30° longitude sections by flow rate and frequency.

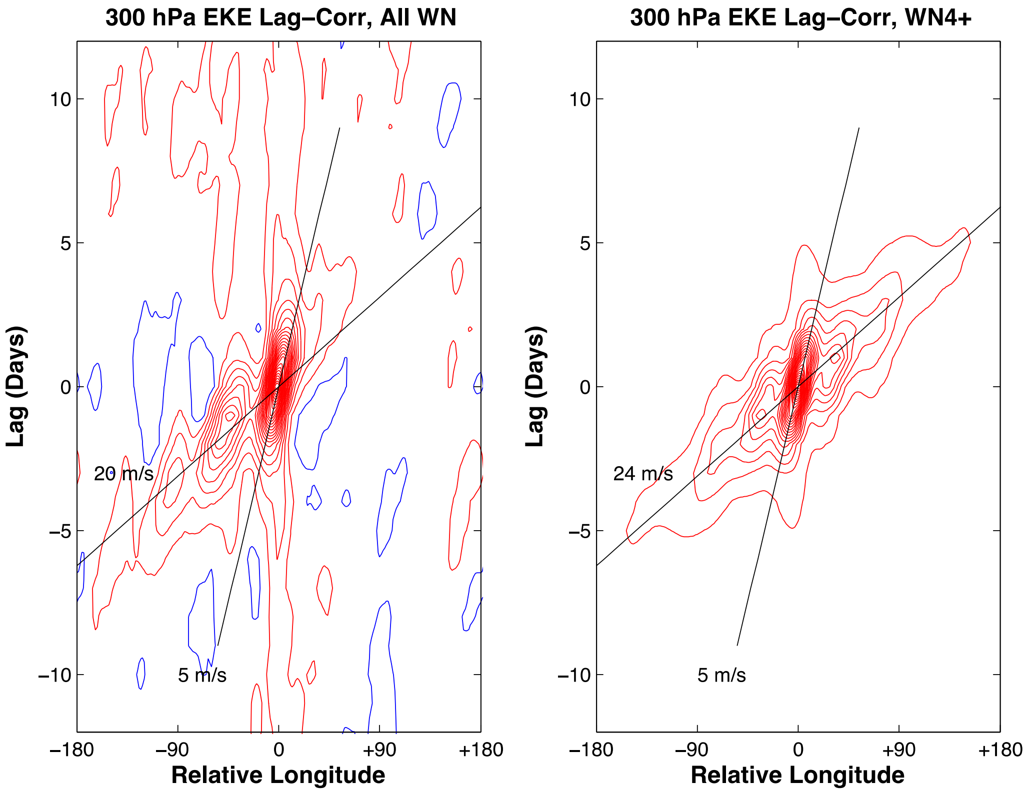

Figure 4.8. (Left panel) The lag-correlation of unfiltered 300 hPa EKE anomalies averaged over 40-60°N. Note the large positive correlations that remain fixed at roughly one longitude over the course of numerous days; this feature is a result of planetary and quasi-stationary waves. The steep and shallow black lines correspond to propagation rates of 5 m/s and 20 m/s, respectively. (Right panel) The lag-correlation of 300 hPa EKE anomalies averaged over 40-60°N after being filtered for just wavenumbers 4 and up. The steep and shallow black lines correspond to advection speeds of 5 m/s and 24 m/s, respectively.

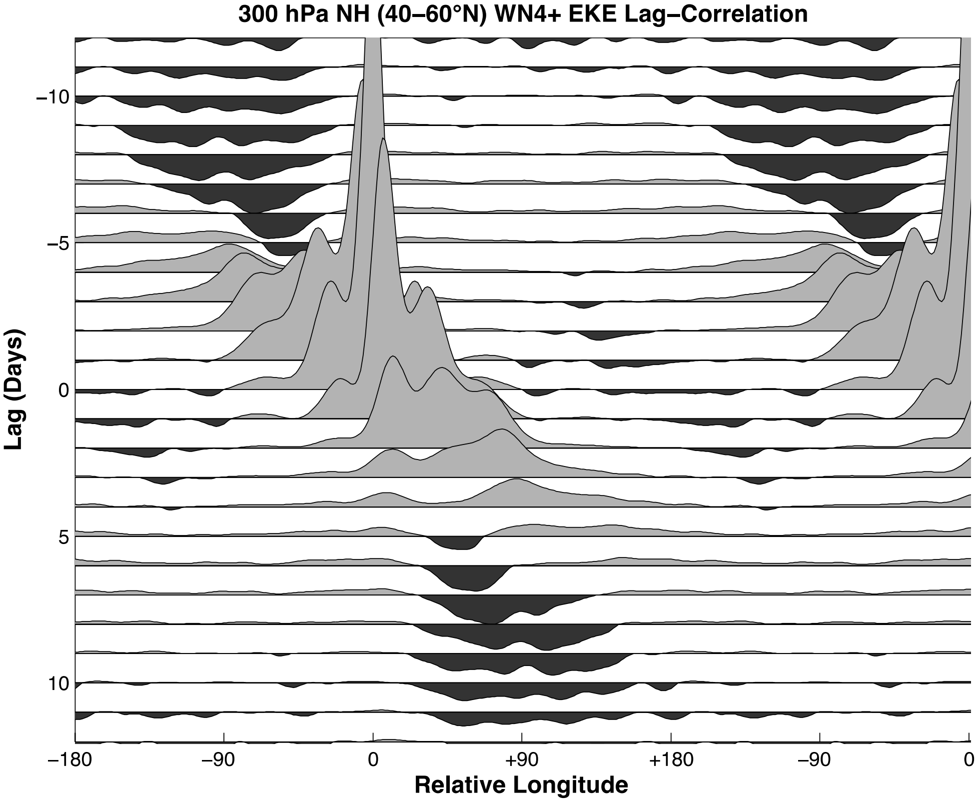

Figure 4.9. Lag-correlations of wavenumber 4+ filtered 300 hPa EKE over 40-60°N, illustrated as fill curves over different longitudes at a given lag. Note the decay of the initially positive correlations as the wave packet propagates east, and their replacement by negative correlations.

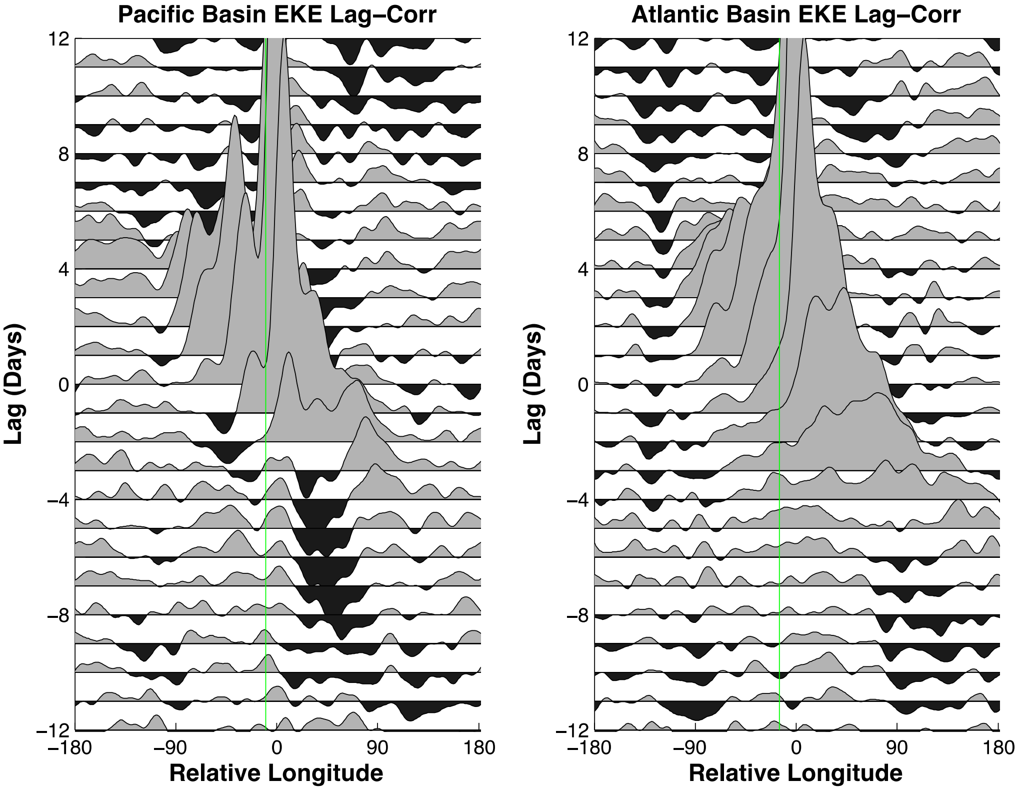

Figure 4.10. (Left panel) Lag-correlations of WN4+ 300 hPa EKE anomalies at 150°E, or over the Western Pacific storm track, expressed as relativistic filled curves at individual lags. (Right panel) As in the left panel, but for 300°E/60°W, or over the Western Atlantic storm track. In both panels, the vertical green lines denote the approximate location of the average coastline in the 40-60°N latitude range.

CHAPTER 5

SIMULATIONS OF THE BAROCLINIC ANNULAR MODE IN GCMS

Thus far, the analyses presented in this thesis have utilized only data from the ERA-Interim reanalysis product, which have been treated as observations. However, given the importance of modeling to modern atmospheric science research, it is worth exploring the extent to which the BAM and the periodic behavior associated with it are captured by global climate models (GCMs). To that end, two GCMs have been selected for close study: the grey radiation aquaplanet model (Section 5.1) and the GFDL dry dynamical core (Section 5.2).

5.1 Grey Radiation Aquaplanet Model

As a first-order exploration of how GCMs represent the BAM, output from a grey radiation aquaplanet model (Frierson et al. 2006) is analyzed in this section. The model represents a rather simple scenario: as an “aquaplanet,” there is no topography in the model, but rather a global slab ocean. The slab ocean consists of a single mixed layer (homogenous temperature with depth) of set heat capacity and adjusts according to radiative fluxes. While the model contains water vapor, there are no clouds. The entire atmosphere is treated as “grey,” with pre-specified longwave absorption and radiative fluxes that are a function of temperature only. Shortwave radiation absorption by the atmosphere is also neglected to better capture the effects of radiative destabilization of the atmosphere. Finally, the model contains no seasonal cycle: instead, an invariant equatorial irradiance value is prescribed and modified symmetrically as a function of latitude (equinoctial conditions).

Clearly, these are rather substantial simplifications, and the behavior of eddies in the model will not be identical to what is observed in the real atmosphere. However, this model configuration isolates the core dynamics at work in the extratropical atmosphere without the complications of topography and seasonality. Therefore, if the BAM is an intrinsic property of a baroclinic atmosphere, its periodic signature in EKE and EHF should be present in the aquaplanet model.

5.1.1 Spectral analyses

First indications from the aquaplanet GCM would seem to be that the model does not capture well the signature periodicity of the BAM. Spectra from 350 hPa EKE anomalies averaged over 30-70° in each hemisphere contain multiple peaks scattered between 0.02 and 0.05 cycles per day (one cycle per 20-50 days), with no particularly robust peaks standing out distinctly from the others (Figure 5.1). If interpreted very narrowly, this could perhaps be considered suggestive of a variable quasi-periodicity, but this explanation seems unlikely. The far more likely culprit is sampling variability, especially given that this result stands in contrast to a similar examination of the aquaplanet model from Thompson and Barnes (2014). Additionally, the 7200 days analyzed amounts to less than 20 years of total data, and the previous examination of decadal-scale (see Ch. 3) time series shows how relatively short periods of record can obfuscate long-term signals.

5.1.2 Lag-correlation analyses

An initial inspection of the EKE anomaly lag-correlation Hovmoeller analysis from the aquaplanet GCM would seem to indicate very clear, robust propagation of wave packets. A very coherent region of high correlations spreads from lag -10 to lag +10 along an axis of motion at 25 m/s, more than circling the globe before diminishing below significance thresholds. Negative correlations also emerge in the wake of this wave packet on a similar timescale to what is seen in observations.

The cascading filled curve plot in Figure 5.3 gives an alternative visualization of the progression of lag-correlations. The eastward propagation of correlation centers is obvious, as is the emergence of negative anomalies at an approximate 3-6 day lag. Considerable noise exists in this analysis, likely a result of the relative brevity of the time series utilized (3000 days). Notably, correlations beyond the day ~15 timescale fail to meet significance thresholds, again consistent with the lack of a single robust periodicity in the zonal-mean spectrum. How these results compare to observations will be discussed in greater detail in section 5.3.

5.2 Dry GCM

While there are many other simple model configurations in which the BAM could potentially be identified, a dry dynamical core enables exploring the properties of a baroclinic atmosphere in the total absence of moisture. For this study, the Geophysical Fluid Dynamics Laboratory (GFDL) spectral dry dynamical core was examined. The dry core essentially replaces the complexities of explicitly simulating radiation, turbulence, and moist convective processes with greatly simplified equations for forcing and dissipation

(Held and Suarez 1994). Topography is also absent, and rather than having a well-defined surface, the model instead applies the radiative relaxation scheme at the "surface" pressure (see below).

The model has a T42 spectral resolution, which translates into an approximate grid spacing of 2.8° x 2.8° with 20 evenly spaced sigma levels (Held and Suarez 1994). The closest available pressure to 300 hPa that still resides within the troposphere is 324 hPa, and this level is therefore the one utilized in exploring upper-tropospheric EKE anomalies. Radiative effects are simulated by employing a relaxation temperature profile as a function of pressure and latitude, with the default configuration set to be hemispherically symmetric. This default configuration is modifiable by introducing a Χ (chi) parameter to describe the degree of hemispheric asymmetry (see McGraw and Barnes 2016, and references therein). For the run analyzed in this thesis, a chi parameter corresponding to perpetual March 15 insolation was employed; conditions are therefore nearly but not quite equinoctial. Model output was obtained in daily form, and the first 1440 days were discarded for model spin-up, leaving 7200 days for analysis.

5.2.1 Spectral analyses

Straight away, spectral analysis of the daily upper-tropospheric EKE anomalies from the dry core model reveals a much clearer BAM periodicity than in the aquaplanet model (Figure 5.4). Again, slight differences exist between the NH and SH despite the relatively symmetric conditions, but noise can likely be invoked to explain such discrepancies. However, both possess marked periodicity around the 0.03 to 0.04 cycles per day (20 to 25 days per cycle) mark, indicating the likelihood of substantial influence from the BAM.

Analyses of spatial variability in the following section will offer additional support to this assertion.

5.2.2 Lag-correlation analyses

At this point, a not-insubstantial variety of datasets have been analyzed using lag-correlation, but none has been quite so robust as that of the dry GCM 324 hPa EKE. Figure 5.5 contains two such analyses, the topmost being the Hovmoeller diagram of 40-60°N mean EKE anomaly correlations and the bottom being the same result when calculated for 40-60°S. What is immediately apparent is the robust and long-lived nature of the primary correlation centers. The main positive correlation (main anomalous wave packet) can be traced in both hemispheres from nearly lag -10 to lag +10, during which time it circles the globe at least a time and a half. Additionally, the negative sidelobes associated with leading and trailing regions of anomalously negative EKE are highly prominent for nearly as great a time span.

Diagrams for both hemispheres, despite their very similar appearances qualitatively, were included to illustrate the discrepancies between the hemispheres despite near-equinoctial conditions. The most prominent different is the magnitude and timing of the re-emergence of the positive correlations. In the NH, these correlations are greater and appear in the lag +/- 25-30 day range; in the SH, positive correlations are far weaker and appear around the lag +/- 20 day range. This is consistent with the frequency at which each spectral peak appears in Figure 5.4. The difference in time scales seems unlikely to be linked to the slight hemispheric asymmetry of insolation, but no other explanation readily presents itself. It seems likely that the difference is largely down to noise.

Finally, the lag-correlation cascading filled curves plot (Figure 5.6) serves very well to illustrate the clarity of wave propagation in the dry GCM. When compared to Figure 5.3, Figure 5.6 clearly contains less noise and looks more like our idealized BAM scenario (more on this in Chapter 6; refer, for instance, to Figure 6.1). Correlation centers propagate steadily to the east while negative correlations develop in their wake. At a given longitude, this lag is approximately 3-6 days, consistent with the Hovmoeller portrayal of lag-correlations. Overall, the results obtained from the GFDL dry dynamical core bear strong resemblance to the observations.

5.3 Comparison to Observations

At first glance, the lag-correlation Hovmoeller diagram of upper-tropospheric EKE anomalies from the aquaplanet simulation appears qualitatively very similar to that of the ERA-Interim data (compare Figures 5.2 and 3.11). However, there is a crucial lack of significant anomaly correlations beyond lag ~15. While present, the anomaly correlations are nowhere near as strong as the observed, and largely fail to meet the significance threshold of around $r = 0.04$. This result is consistent with the multiple, scattered periodicities that appear in the corresponding power spectra, but is most likely to just be a consequence of sampling variability.

Because many of the limitations that were identified with the aquaplanet model also apply to the dry dynamical core model, it seems logical to conclude that explicit simulation of moist processes are not necessary to produce the BAM. Any non-sampling factors contributing to the differences between the aquaplanet and dry GCM periodicity are not obvious, but differences in boundary-layer processes could contribute. The aquaplanet has a defined slab-ocean surface, whereas the dry GCM simply uses radiative relaxation to simulate a near-surface atmosphere, resulting in rather poor representation of processes like lower-tropospheric mixing (McGraw and Barnes 2016). The result could be something of an idealized tropospheric temperature gradient that enables the BAM to emerge more clearly.

5.4 Summarizing Remarks

This chapter has investigated the degree to which periodicity in the baroclinic annular mode, which is robust in the real atmosphere, appears in two types of global climate models. The models shared several properties, most notably their lack of explicit moist processes and their use of homogeneous surfaces (though the treatment of the surface layer was strikingly different in each). Power spectra of upper-tropospheric EKE from the aquaplanet simulation appeared to show a less robust than expected periodicity, but the dry GCM spectra looked nearly identical to those from the ERA-Interim analyses. Similar patterns were reflected in the lag-correlations, with much more robust negative anomaly correlations flanking the main wave packet in the dry GCM simulation.

Thus, it appears that moist processes are not necessary to produce the required fluctuations in baroclinicity that give rise to quasi-periodic variability in midlatitude cyclone activity, although the degree to which various models capture the periodicity evidently depends on numerous factors. Despite not having an explicit surface, the dry GCM does an excellent job of producing a BAM of approximately the correct periodicity. The aquaplanet produces a less marked periodicity despite having a slab ocean surface that ensures preservation of mean-state baroclinicity, but given that this result conflicts with past studies (i.e., Thompson and Barnes 2014), this is likely a product of sampling variability. Future studies may consider analyzing additional models to help clarify what aspects of model configurations affect the ability to model the BAM.

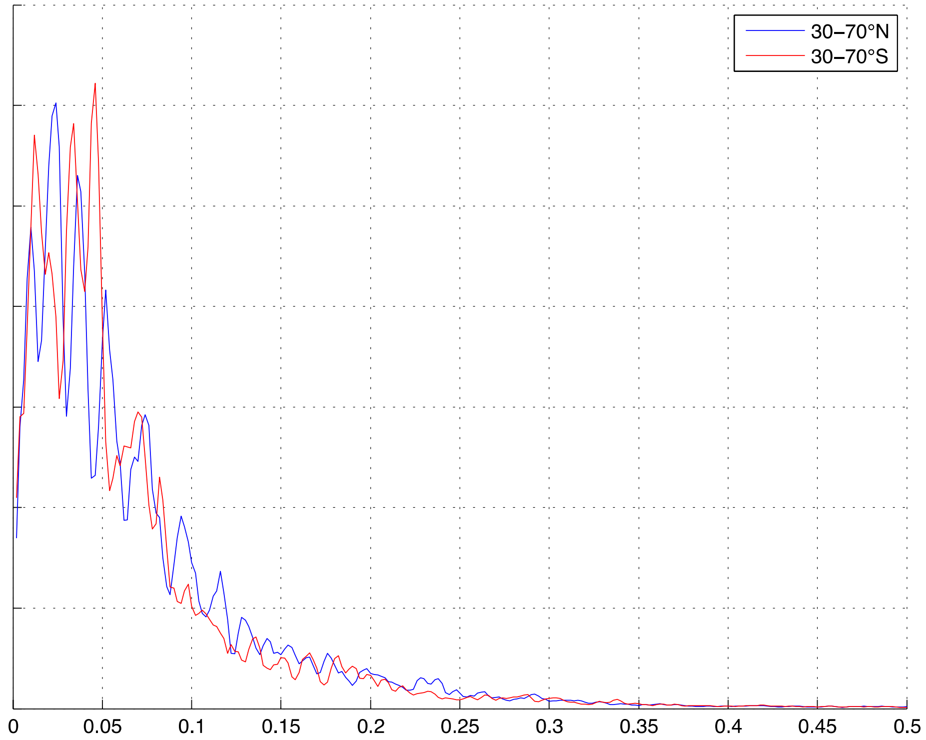

Figure 5.1. Power spectra of 350 hPa EKE from each hemisphere of the aquaplanet GCM. Multiple spectral peaks are scattered between approximately 0.02 and 0.05 cycles per day, but a robust, single periodicity is absent.

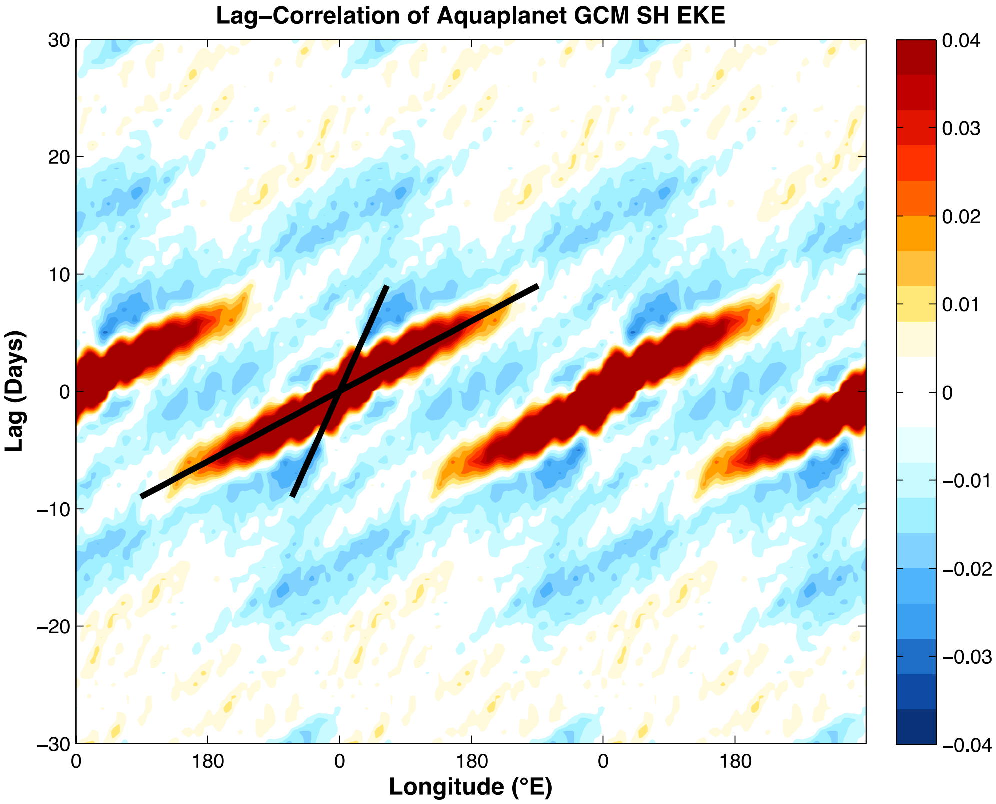

Figure 5.2. The lag-correlation of 40-60°S mean EKE anomalies from the 3000-day run of the aquaplanet GCM. Bold black lines correspond to a phase speed of 6 m/s (steep line) and a group velocity of 25 m/s (shallow line).

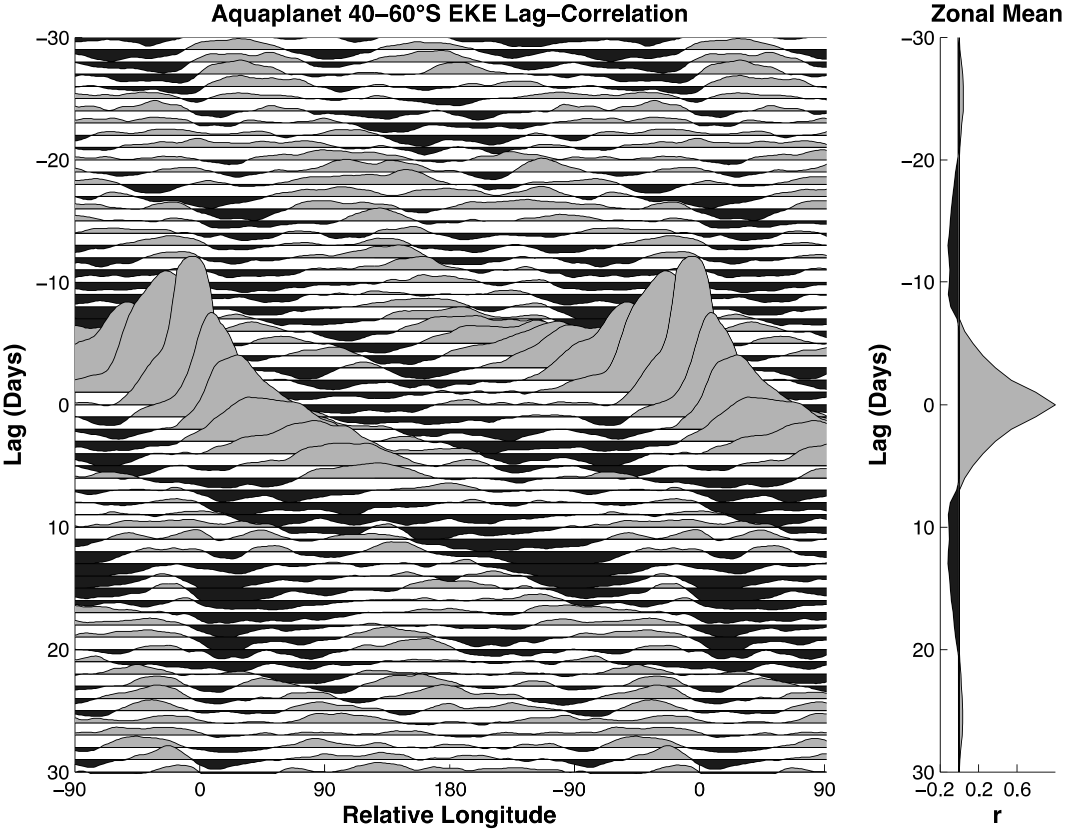

Figure 5.3. (Left panel) Lag-correlations of daily-mean 40-60°S EKE anomalies from the 3000-day run of the Aquaplanet GCM, expressed as relativistic filled curves at each individual lag. (Right panel) The autocorrelation sequence for the zonal-mean EKE anomalies.

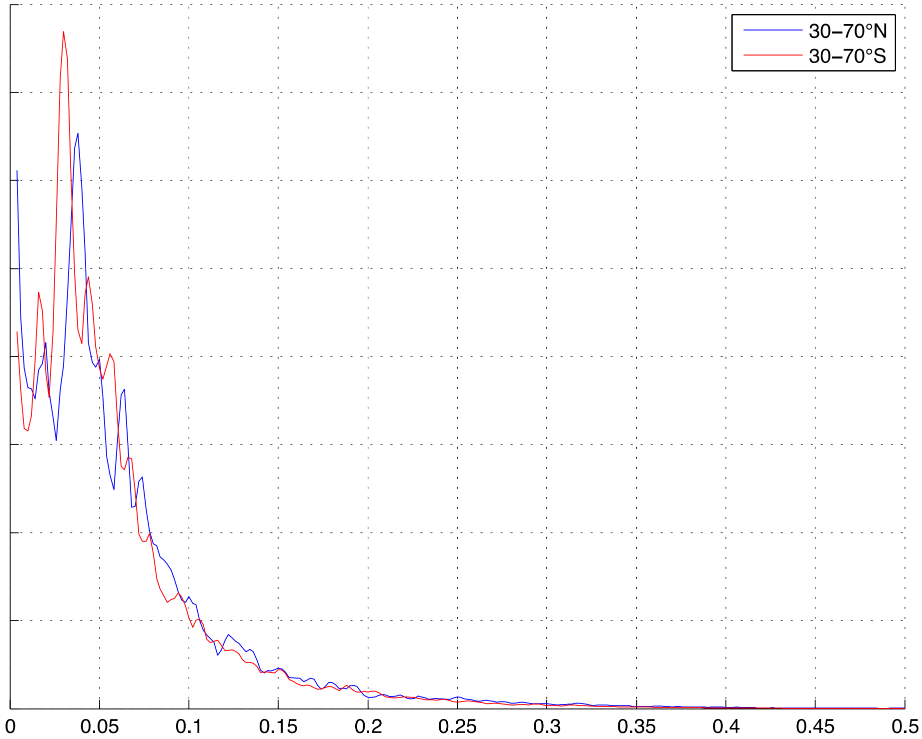

Figure 5.4. Power spectra of 324 hPa EKE anomalies from each hemisphere of the GFDL dry core model. Unlike in the aquaplanet model, both hemispheres have clear spectral peaks in the requisite 0.03-0.04 cycles per day range.

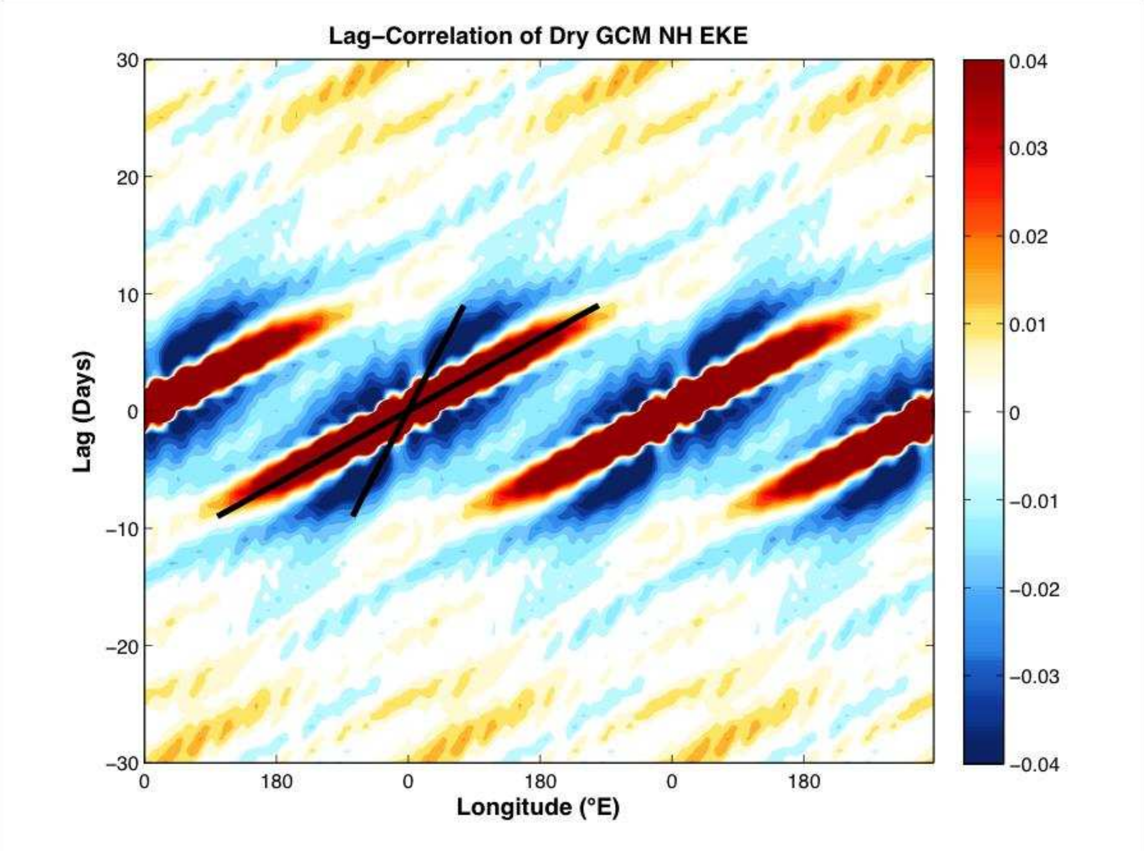
Lag−Correlation of Dry GCM NH EKE
Lag (Days)
30
20
10
0
−10
−20
−30
Longitude (°E)
0
180
0
180
0
180
0.04
0.03
0.02
0.01
0
−0.01
−0.02
−0.03
−0.04

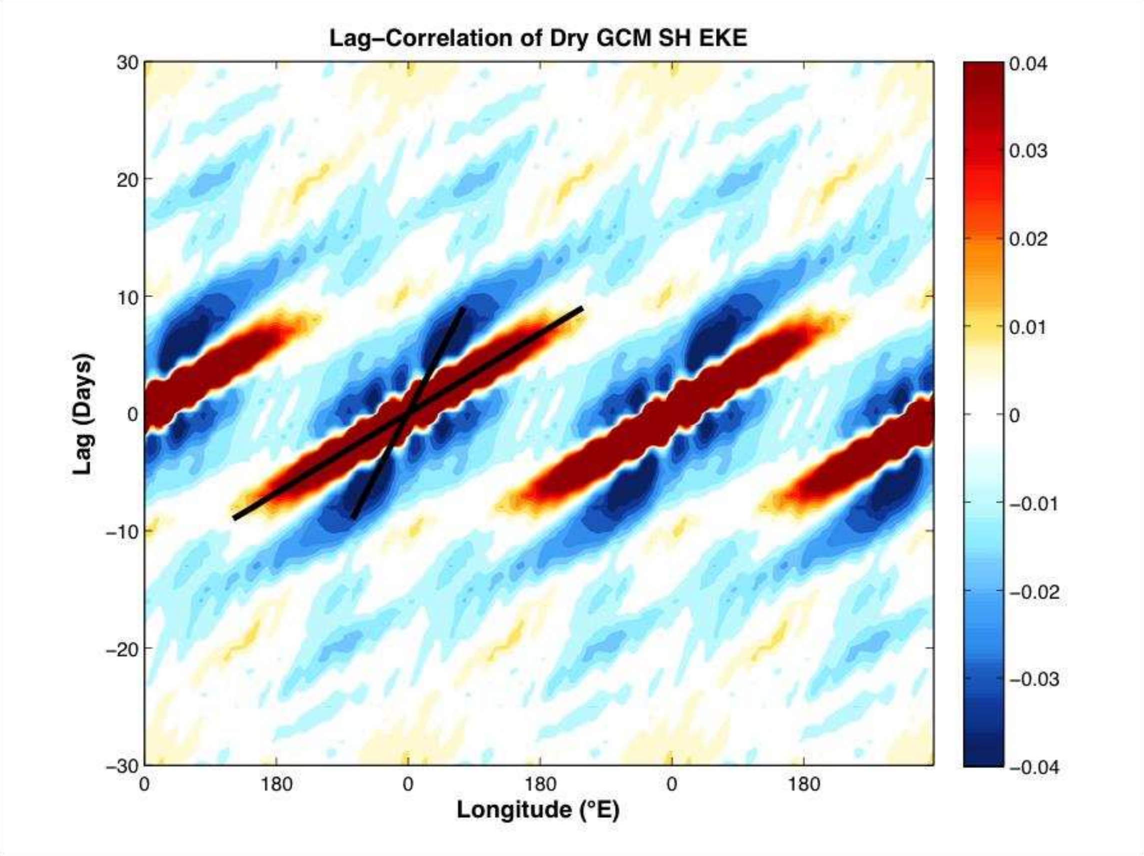
Lag−Correlation of Dry GCM SH EKE
Lag (Days)
30
20
10
0
−10
−20
−30
Longitude (°E)
0
180
0
180
0
180
0.04
0.03
0.02
0.01
0
−0.01
−0.02
−0.03
−0.04

Figure 5.5 (previous page). Top panel: Lag-correlation Hovmoeller diagram of NH EKE anomalies from the GFDL dry core model. Propagation lines correspond to 7 m/s (phase speed, steep line) and 24 m/s (group velocity, shallow line). Bottom panel: lag-correlation Hovmoeller diagram of SH EKE anomalies from the GFDL dry core model. Propagation lines correspond to 7 m/s (phase speed, steep line) and 22 m/s (group velocity, shallow line).

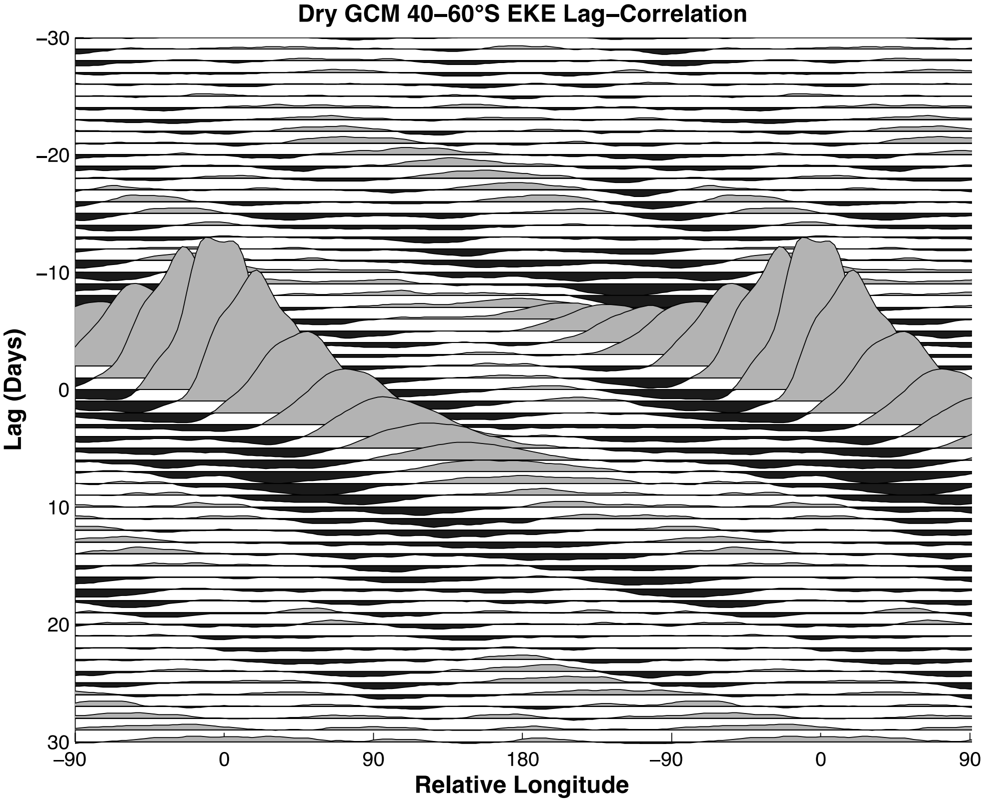

Figure 5.6. As in the left panel of Figure 5.3, but for the lag-correlation curves calculated from the GFDL dry GCM data.

CHAPTER SIX

PHYSICAL MECHANISMS OF PERIODICITY IN THE BAM

Given the periodicity and spatial patterns associated with the BAM that are apparent in observations and to a lesser extent in global climate models (see Ch. 3, 4, and 5), a hypothesis for the mechanism by which the BAM operates was proposed. This hypothesis is delineated in section 6.1, beginning with the concepts from prior studies that this thesis seeks to build upon. In order to test the hypothesis, a simple model of the extratropical storm track, which assumes two-way linear feedbacks between mid-tropospheric baroclinicity and upper-tropospheric eddy kinetic energy, was developed. Similar analyses to those presented in Chapters 3 and 4 were then repeated on the model results to test the validity of this assumption. Section 6.2 will describe the parameters used to initialize the model. Section 6.3 will then present the results of the model, and section 6.4 will analyze and compare these results to what is seen in observations and GCMs.

6.1 Hypothesized Mechanism for Periodicity in the BAM

While the analyses in prior chapters have demonstrated that there is intricacy and nuance to the BAM, the core principle is believed to be relatively simple: baroclinic eddies grow in the midlatitudes via conversion of available potential energy to eddy kinetic energy (Thompson and Woodworth 2014). The available potential energy, in turn, is driven by meridional heating gradients, which give rise to baroclinicity. The timescale for the BAM is therefore constrained by the timescales for baroclinic eddy growth (the consumption of baroclinicity) and the generation of baroclinicity (thermodynamic processes giving rise to temperature gradients).

This paradigm was originally hypothesized and tested by Thompson and Barnes (2014), who utilized a simple damped oscillator model to demonstrate that quasi-periodic behavior was driven by two-way feedbacks between baroclinicity and eddy fluxes of heat. The equations employed for this coupled oscillator are essentially linearizations of the Eady growth rate (equation 6.1) and thermodynamic energy (equation 6.2) equations (the mathematics are explained in great detail in the supplemental materials for the article):

$$(6.1)\ \frac{\partial}{\partial t}\{v^*T^*\} = -\alpha\{b\} + \varepsilon(t)$$

$$(6.2)\ \frac{\partial\{b\}}{\partial t} = \beta\{v^*T^*\} - \frac{\{b\}}{\tau}$$

where {} denote zonal-mean quantities, * denotes a difference from the zonal mean (zonal anomaly), b represents baroclinicity via the meridional temperature gradient (dT/dy), α and β are regression coefficients corresponding to the amplitude of the feedbacks between baroclinicity and eddy heat flux, τ is a damping time scale, ε is a random noise term that prevents the modeled heat fluxes from diminishing to zero.

By integrating these two equations in time, the model was able to produce oscillating behavior on a time scale commensurate with the amplitude of the feedbacks and the damping time scale. Regression coefficients and the damping time scale were calculated for all of the available pressure levels, but ultimately the 500 hPa (mid-troposphere) level provided the most similar spectral result to the observed (Figure 6.1).

Viewed from the more simplistic zonal-mean framework, there is a simple interplay of baroclinicity and EKE or EHF anomalies; it is this concept that is illustrated in the

Thompson and Barnes (2014) model. However, our analysis seeks to understand the lag-longitude structure seen in observational and model analyses. As revealed by the lag-correlation analyses from Chapters 3 and 4, these processes do not happen with regular periodicity on local to regional scales – rather, the periodic behavior of the BAM emerges only on near-hemispheric scales. Mainly this is a product of the regional nature of EKE anomalies and their eastward propagation, leaving negative anomalies (also propagating eastward) in their wake (Figure 6.2). The next section will describe how the longitudinally-varying "baroclinic conversion" model is constructed.

6.2 Model Parameters

The Thompson and Barnes (2014) model demonstrated that while the choice of damping timescale was crucial to the resulting temporal variations in eddy heat fluxes, a simple coupled oscillator can capture the same basic periodicity seen in observations of the BAM. The new model developed here is more complex than the original for two main reasons: first, the oscillation in eddy heat fluxes is not directly prescribed; second, this model varies by longitude, whereas the original simply modeled an interchange between zonal quantities of baroclinicity and eddy heat flux.

Although structured differently from its predecessor, the equations in the new baroclinic conversion model have very similar origins. The first equation is a prognostic equation for baroclinicity averaged over the 40-60°S "storm track" region. Three assumptions were made in developing the equation: first, that the magnitude of eddy heat fluxes is strongly related to the amplitude of wave activity; second, that the diffusive nature of eddy heat fluxes allows us to model the change of baroclinicity with time as being linearly proportional to the eddy fluxes; and third, the combined effects of adiabatic and diabatic processes can be collectively be modeled as linear damping of the baroclinicity (for an alternative explanation, refer to Thompson et al. 2016, submitted to JAS).

With these basic assumptions in place, the thermodynamic energy equation can be linearized about a basic state to yield:

$$(6.3)\ \frac{\partial}{\partial t}\langle b\rangle + \langle U_b\rangle \frac{\partial}{\partial x}\langle b\rangle = \beta\langle k\rangle - \frac{\langle b\rangle}{\tau_b}$$

where brackets denote quantities averaged over 40-60°S at all longitudes, *b* is the time series of baroclinicity ($[T_{40°S}-T_{60°S}]/dy$), U_b is the mean rate of advection of baroclinicity over 40-60°S, β is a regression coefficient coupling eddy heat fluxes to baroclinicity, *k* is the time series of 40-60°S mean eddy heat flux anomalies, and τ_b is the baroclinicity damping time scale.

The second equation is predicated on very similar assumptions: first, the growth rate of eddy heat fluxes is linearly proportional to the baroclinicity; second, the dissipation of eddy heat fluxes can be reasonably well modeled by linear damping. Applying these assumptions and linearizing about a basic state yields:

$$(6.4)\ \frac{\partial}{\partial t}\langle k\rangle + \langle U_k\rangle \frac{\partial}{\partial x}\langle k\rangle = \alpha\langle b\rangle - \frac{\langle k\rangle}{\tau_k}$$

where *k* and *b* are the same as in the previous equation, U_k is the mean rate of advection of the eddy heat fluxes, α is a coupling coefficient relating baroclinicity anomalies to eddy heat flux anomalies, and τ_k is the damping time scale of the eddy heat flux anomalies. Note how similar this equation is to Equation 6.1: the core equation still relates the time rate of change of eddy heat fluxes (LHS term 1) to the baroclinicity (RHS term 1) and a time damping term (RHS term 2), but with the addition of a term for zonal advection (LHS term

2). The structural parallels to the Eady growth rate equation (Thompson and Barnes 2014, equation 1) are thus apparent.

Both the time series and the regression coefficients are derived from observational data. Using the same ERA-Interim dataset as analyzed in previous chapters, eddy heat fluxes at 700 hPa are averaged over 40-60°S. The baroclinicity time series is simply calculated at the 700 hPa temperature at 40°S minus the temperature at 60°S for all longitudes, then divided by the physical distance between the two latitude circles (resulting in K/m). Both time series are put into anomaly form by subtracting out the seasonal cycle at each grid point.

In order to calculate the linear regression coefficients α and β, time derivatives of the baroclinicity and eddy heat flux anomaly time series must be taken. For α, the coefficient is calculated by regressing observed $\frac{\partial}{\partial t}\langle k' \rangle$ onto b', yielding an approximate value of -24.54 m^2 s^{-2}. For β, $\frac{\partial}{\partial t}\langle b' \rangle$ is regressed onto k', yielding a dimensionless coefficient of 3.43 x 10^{-13}. Calculating the damping time scales is even more straightforward, as each time scale is simply the approximate e-folding time scale of the observed k' and b' time series. These calculations yield damping timescales of 3.94 days for b' (rounds to 4 days) and 1.96 days for k' (rounds to 2 days).

Finally, the model integration is initialized using observational data. The b array is simply initiated by copying the first time step of the daily mean observed b. The k array is initialized with a Gaussian pulse centered at 180° longitude with a half-width of 15° longitude. Peak amplitude is simply the standard deviation of eddy heat flux at 700 hPa, approximately 28.9 K m/s. The final parameters, U_b and U_k, are the independent variables for each of the three cases under which the model is run. The model is integrated using a daily time step for 500 days, but the results are most clear during the first ~50 or so days. The following section explains each mean-wind configuration the model was run under and discusses the results of each simulation.

6.3 Simulation Results

With the relationships between the baroclinicity and eddy heat flux anomalies held steady, the three different simulations presented here are simply based on differing advection schemes. The purpose of altering the advection is to explore what gives rise to the observed periodicity of the BAM. We know from previous chapters that the periodicity is not apparent on local to regional scales, and that this is primarily due to the negative anomalies that appear at later lags occurring at different longitudes. However, the zonal-mean eddy heat flux anomaly power spectrum is identical in all three cases, with a peak periodicity in the observed ~25 day range (Figure 6.3). This principle will be illustrated best using these three cases.

6.3.1 Case 1 – no advection

The first case examined here is the simplest, but also least physically realistic: no advection. For this simulation, $U_b = U_k = 0$, and equations 6.3 and 6.4 collapse to the zonally symmetric equations given in Thompson and Barnes (2014; see equations 6.1 and 6.2) but without the noise term. In the absence of advection, the pulse of eddy heat flux stays fixed at the longitude at which it is initiated and simply undergoes damped cycles of decay and growth. This behavior is illustrated in the fill plot given by Figure 6.4. By day ~6, the initially positive EHF anomalies are replaced by negative anomalies of a lesser magnitude that then persist for several days after. Eventually, positive anomalies re-emerge around days ~20-25 (not shown).

6.3.2 Case 2 – dual advection at identical rates

The second simulation is predicated on the assumption that EHF anomalies and baroclinicity anomalies are both advected along at the same rate, the group velocity of Rossby waves in the free troposphere (~25 m/s). Since the two fields are being advected eastward at identical rates, the resulting longitudinal distribution and magnitude of the anomalies on any given day is identical to case 1; however, the wave packet can be seen to propagate rapidly eastward (Figure 6.5). Due to the identical advection rates for baroclinicity and EHF, no overlap exists between the positive and negative anomalies, in stark contrast to our observational results (see Figures 3.13, 4.9).

6.3.3 Case 3 – dual advection at different rates

The third and final configuration in which the model is run is by far the most similar to observations. Both the baroclinicity and the eddy heat fluxes are advected eastward, but at differing rates. One of our base assumptions was that eddy heat fluxes are closely tied to baroclinic wave activity; therefore, the 25 m/s Rossby group velocity is applied to U_k in this case. However, baroclinicity is generally greatest at lower altitudes, and is advected at rates closer to boundary layer wind speeds. Therefore, U_b is set to be 8 m/s for this integration. Such parameters are consistent with the idea that wave packets interact with baroclinicity, but the baroclinicity exists independently and is not a part of the wave packet.

As can be seen in Figure 6.6, this configuration yields a result that bears a strong resemblance to the observations in Figures 3.13 and 4.9. As in Case 2, the positive EHF anomalies propagate to the east rather rapidly. However, instead of negative anomalies developing along the same axis of motion, they develop to the west of the original wave packet. Notably, this also alters the time scale in which the negative anomalies develop. Negative anomalies were present by day ~6 and peaked at day ~9 in the previous cases; here they are present by day ~4 and maximize around day 7. The zonal-mean power spectrum is identical to the previous cases, but the BAM appears quite different on a regional level.

6.4 Comparison to Observations and GCMs

Despite the rather extreme simplifications made in developing the linear baroclinic conversion model, we were able to produce patterns of propagating anomalies that have similar periodicity and propagation behavior to the observed BAM. In some sense, this is not entirely surprising – the linearized equations are derived from the thermodynamic equation, and the coupling coefficients are derived from observed data. However, the actual processes by which baroclinic potential energy and eddy energy quantities are converted and exchanged are highly nonlinear. It is therefore remarkable that these processes can collectively be represented reasonably well by just a pair of linear differential equations.

Experiments in tweaking the parameters used in the model reveal that the zonal-mean periodicity can be modified, mainly by adjusting the damping time scale and the size of the initial Gaussian pulse of eddy heat fluxes. Pulses that are broader in longitude result in longer periods for the BAM, apparently due to somewhat more persistent anomalies (larger pulses take longer to decay). The model can therefore be tuned to the desired periodicity, but the parameters that were ultimately chosen are similar to those observed in the real atmosphere. Therefore, we believe this model to be a useful tool for examining how differing advection rates affect the apparent periodicity of interactions between baroclinicity and eddy quantities on a hemispheric scale.

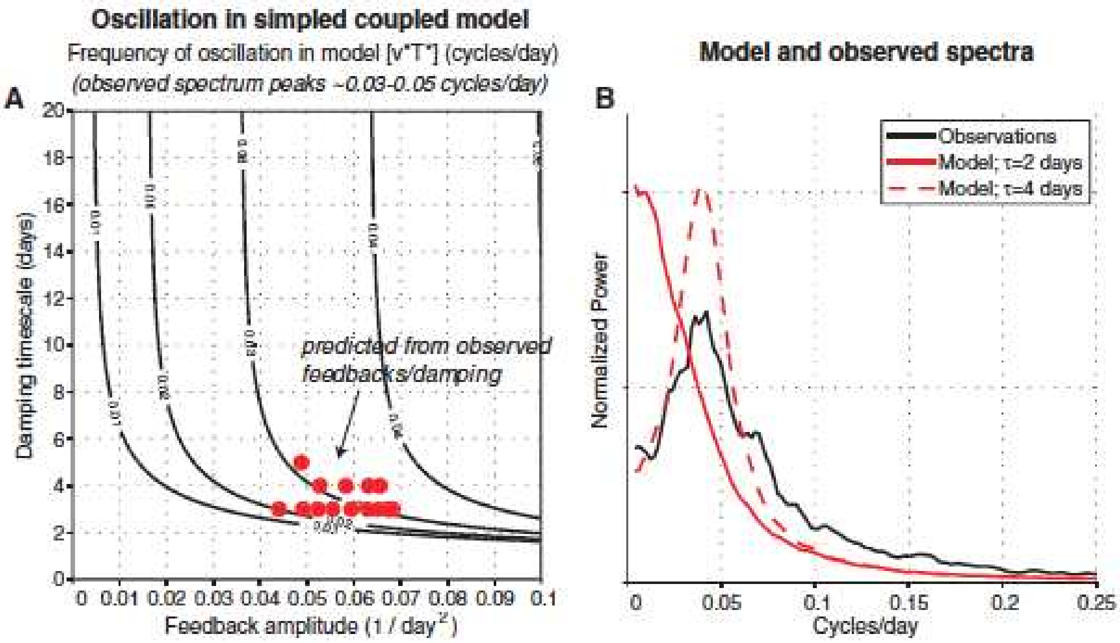

Figure 6.1. Reproduced from Figure 3 of Thompson and Barnes (2014). (Panel A) Solutions for the oscillation frequency of the model in parameter space: the x-axis denotes the value of α x β, while the y-axis gives the values of the damping time scale. The curves labeled 0.01, 0.02, etc. give the resultant frequency of oscillation in cycles per day. (Panel B) The power spectra for the modeled eddy heat fluxes based on two different choices of damping time scale, compared to the spectrum of observed 300 hPa EKE anomalies.

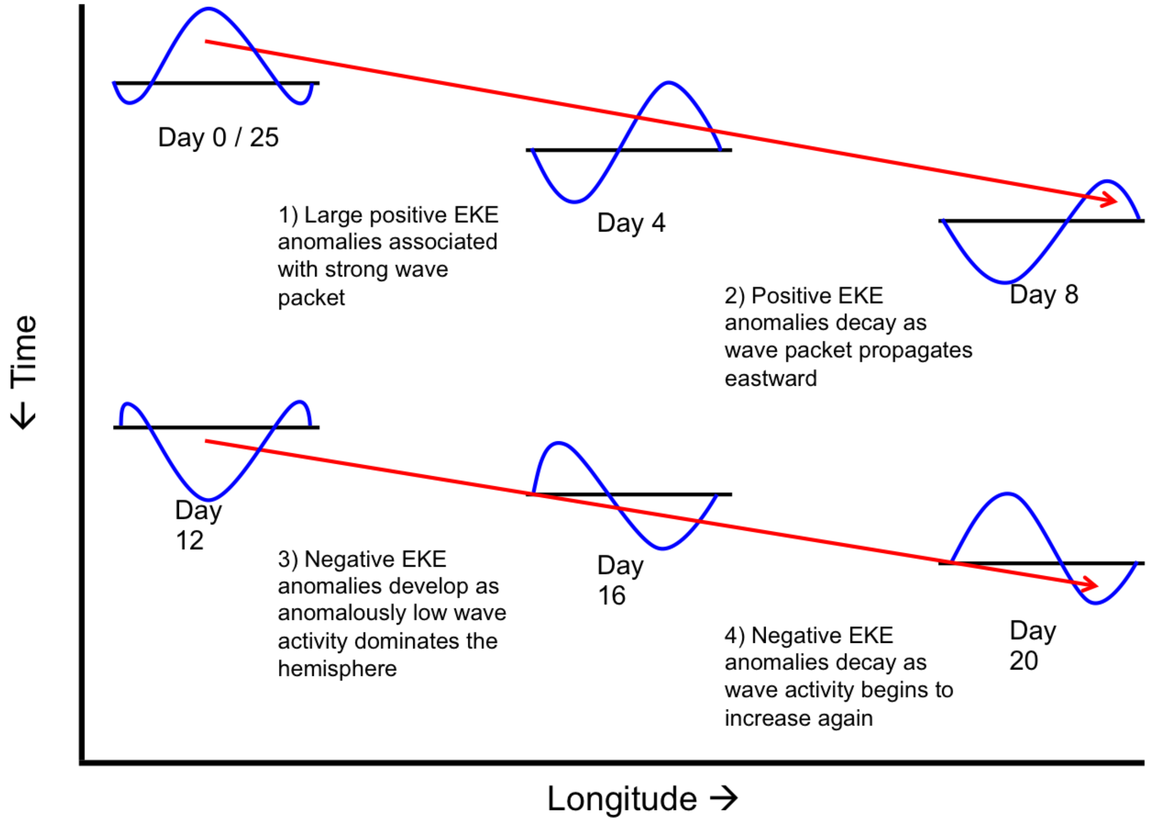

Figure 6.2. Schematic representation of anomalous eddy kinetic energy development and propagation through the approximate 25-day cycle. Curves are representative of EKE or EHF anomalies at a given longitude, and red arrows represent the propagation of the same anomalous wave packet.

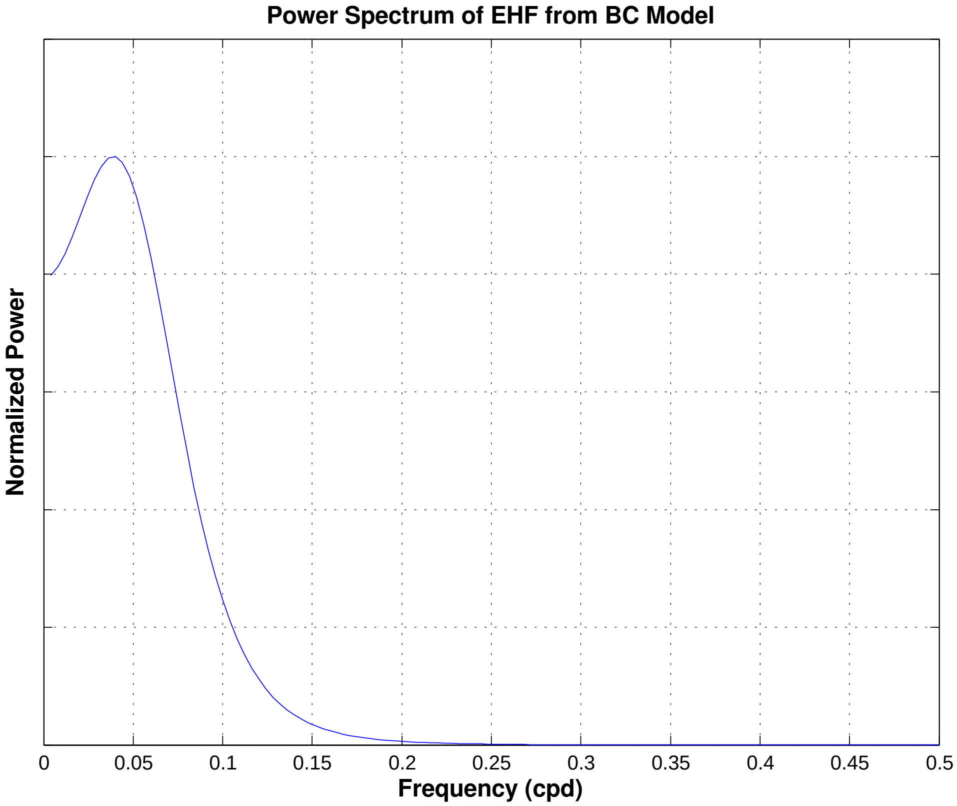

Figure 6.3. Power spectrum of daily mean zonal-mean eddy heat fluxes from the simple baroclinic conversion model. This particular plot shows the results from the Case 1 simulation; however, the spectra from all three cases are identical.

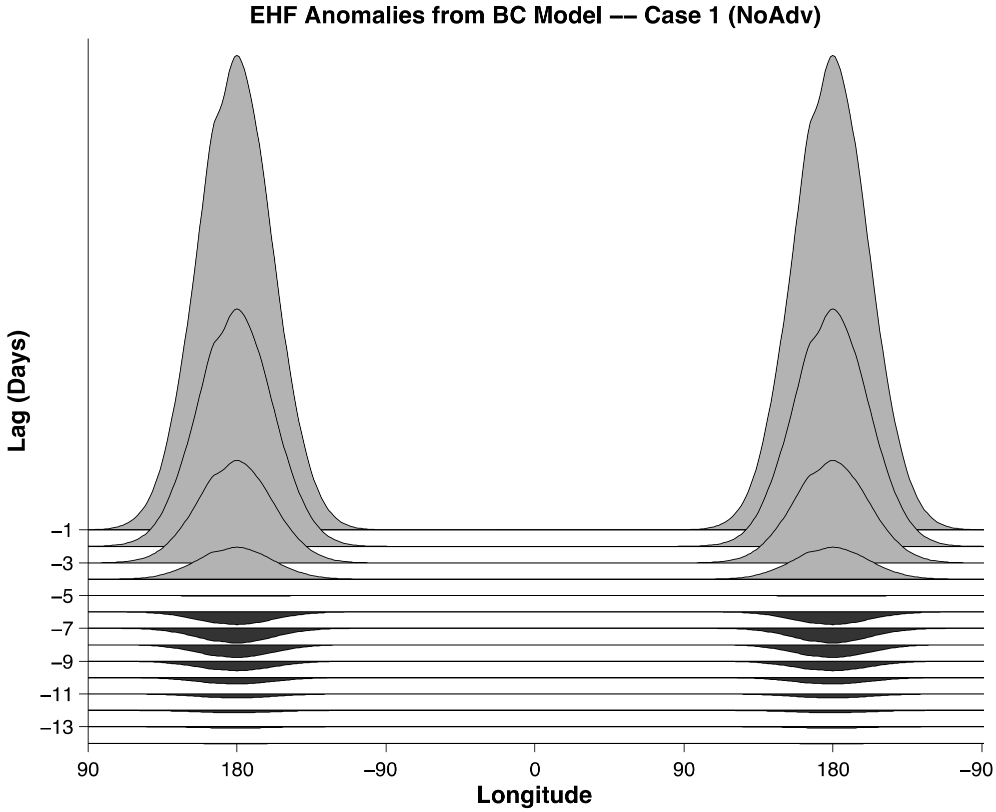

Figure 6.4. Fill plot of eddy heat flux anomalies from the baroclinic conversion model for Case 1 (no advection). The initially positive anomalies simply decay in time at their original longitude, replaced by robust negative anomalies in the day 6-11 range.

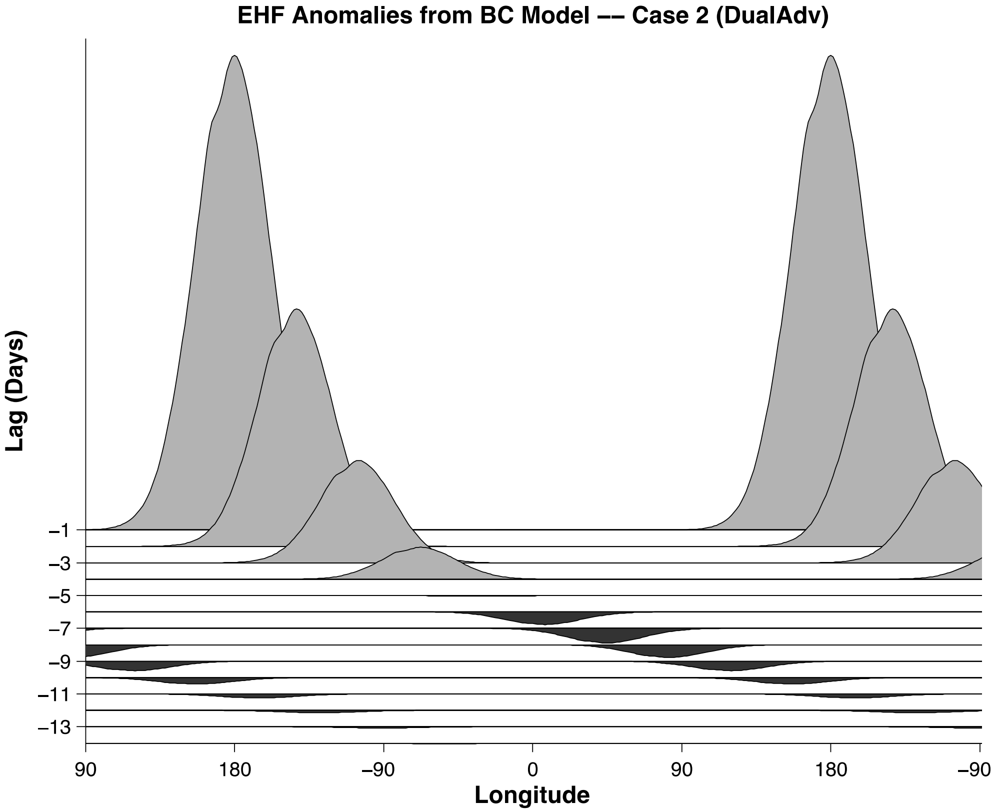

Figure 6.5. As in Figure 6.4, but for the Case 2 simulation (dual advection at the same rate, 25 m/s). Anomalies propagate rapidly to the east as they diminish in magnitude, again resulting in peak negative anomalies around days 6 to 11.

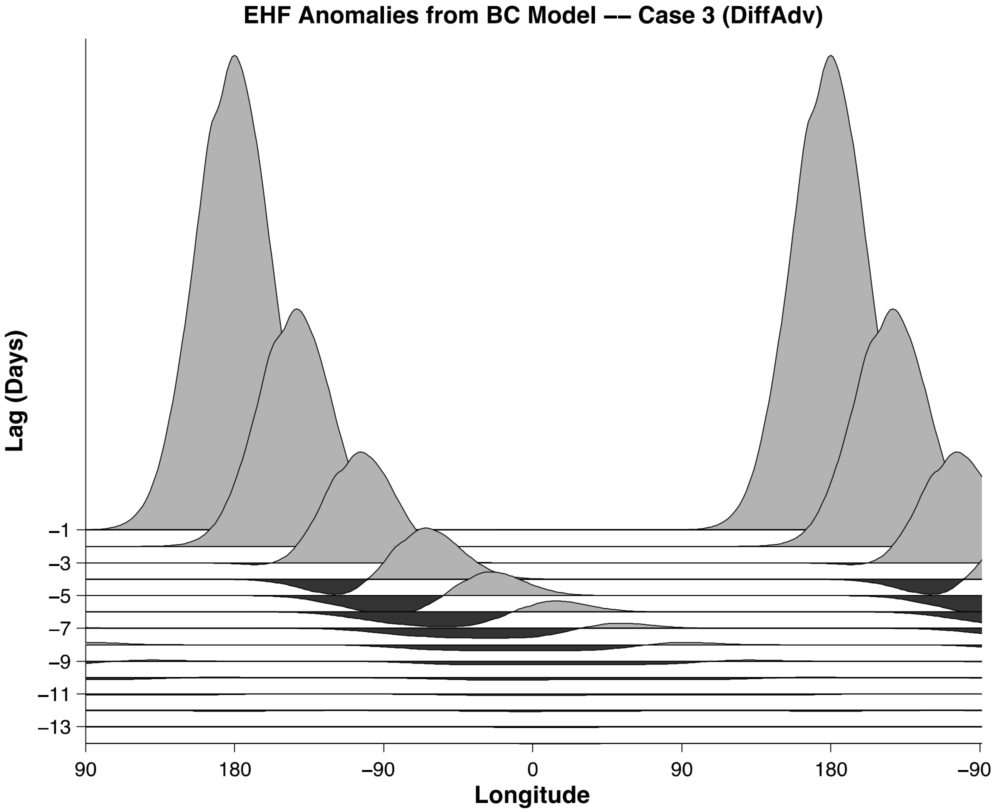

Figure 6.6. As in Figures 6.4 and 6.5, but for Case 3 (dual advection at differing rates: 8 m/s for lower-tropospheric baroclinicity, 25 m/s for eddy heat fluxes). Anomalies propagate eastward at a slower rate and diminish more slowly than in Case 2. This case most strongly resembles the observed propagation of EHF/EKE anomalies.

CHAPTER SEVEN

CONCLUSIONS

The previous chapters of this thesis have been dedicated to examining the properties of a phenomenon dubbed the baroclinic annular modes. In Chapter 1, there is an extensive review of the literature related to annular modes and wave dynamics. Chapter 2 elucidates the origins of the data analyzed in this study and explains the methods used in performing the analyses. Observational data of the Southern Baroclinic Annular Mode (SBAM) are analyzed and discussed extensively in Chapter 3. Many of the most crucial analyses are repeated on data from the Northern Hemisphere in Chapter 4. Chapter 5 explores the presence of periodic behavior in two simplified GCMs. Finally, Chapter 6 explores the physical mechanisms that may give rise to periodic behavior in the BAM. The remainder of this chapter is dedicated to synthesizing the findings described in the other chapters and delineates both the conclusions that can be drawn from our analysis and recommendations for how future researchers could expand upon this work.

7.1 Previous Work and Context

As established in the introductory chapter of this thesis, the work presented here follows from a large body of previous work examining large-scale atmospheric variability. Studies during roughly the first half of the 20th century sought to describe various patterns of spatial variability in terms of highly correlated pressure and temperature features (e.g., Walker and Bliss 1932; Namais 1950). As more complex analyses were applied in later decades, truly global patterns of variability came into recognition, including patterns that would later be described as the "annular modes" (e.g., Kutzbach 1970; Trenberth 1979; Wallace 2000). The best-known annular modes, the NAM and the SAM, essentially describe hemispherically-symmetric, equivalent-barotropic shifts in mass between higher and lower latitudes. However, a series of publications beginning in early 2014 described a new type of hemispheric variability: the baroclinic annular modes.

Quite simply, baroclinic annular modes are characterized by quasi-periodic, hemisphere-scale variations in eddy heat fluxes and eddy kinetic energy, both of which are excellent proxies for baroclinic wave activity (e.g., Thompson and Barnes 2014; Thompson and Woodworth 2014; Li and Thompson 2015). Extensive evidence for periodic behavior in the BAM on a hemispheric scale was presented in these studies, but no assessment was made of the spatial limitations of this periodic behavior. Among the goals of this thesis are to determine what spatial limits apply to the BAM, explore the longitudinal structure of midlatitude wave packets in the context of the BAM, and further develop the conceptual model of the BAM. The following sections will reflect on how these goals were accomplished, and what contributions this study has made to the existing body of knowledge of the BAM.

7.2 Observed and Modeled Periodic Behavior in the BAM

Using "observed" data from the ERA-Interim reanalysis, this thesis explored the projection of the baroclinic annular modes onto various eddy-related fields. While spectra of hemisphere-mean time series had been calculated for previous studies, this concept has been extended to examine progressively smaller spatial scales in this thesis. In the SH, the periodic behavior in the BAM appears down to longitude spans of 120° or less; in the NH, this extends only to 180° or so. Extensive use of lag-correlation analyses reveals the spatiotemporal structure of these anomalies as they evolve in time and propagate about the hemisphere. These analyses revealed the longitudinal overlap of regions of positive and negative anomalies, as eastward-advecting wave packets continuously left anomalously low baroclinicity in their wake.

Periodic behavior is most evident in spectra of zonal-mean time series and in spectra of time series constructed by following the atmospheric flow at intermediate (~5-15 m/s) speeds. The lack of complicating topographical features and zonal land-sea contrasts means that the BAM appears more robustly periodic in the Southern Hemisphere than in the Northern Hemisphere, although filtering out planetary wavenumbers helps clarify the NH signal. Power spectra calculated over temporal subsets of the 36-year analysis period hint at possible decadal variability in the BAM, but any connections to ENSO or longer-term oscillations were not clear.

Finally, it appears that some global climate models are capable of accurately capturing the BAM's periodic behavior. Spectra from the aquaplanet GCM are inconclusive due to conflicting results between this study and Thompson and Barnes (2014), most likely a result of sampling variability. In contrast, those from the GFDL dry dynamical core model indicate that the BAM is robust, even in the absence of moist processes. A far more robust examination of a wider suite of global models is required to make any generalizable conclusions about the efficacy of dynamically modeling the BAM.

7.3 Evaluation of the Hypothesized BAM Mechanism

The hypothesized mechanism for the BAM was alluded to throughout the analysis chapters of this thesis, but was most explicitly discussed during Chapter 6. There, our conceptual model of the periodic behavior in the BAM was fleshed out: an anomalous wave packet propagates eastward consistent with Rossby wave dynamics, feeding on lower-tropospheric baroclinicity that is itself being advected eastward at speeds consistent with winds at lower levels. As the baroclinic potential energy is converted into eddy kinetic energy, baroclinicity is reduced trailing the wave packet and an anomalously low eddy kinetic energy center develops accordingly. The original wave packet decays in time, but begins to re-emerge after day ~20 as the baroclinicity is recharged by thermodynamic processes.

Observing the cycle of eddy kinetic energy or eddy heat flux on local to regional scales is insufficient to observe the periodicity associated with the BAM, due in large part to regional asymmetries in wave activity and propagation. However, this periodic behavior does become apparent when examining hemispheric averages of various extratropical cyclone related fields or when following the atmospheric flow at speeds intermediate to the advection rates of the wave packet and baroclinicity. The conceptual model presented in Chapter 6 offers robust confirmation of the validity of this mechanism.

7.4 Comments on the Implications for Weather and Climate

Assessing the significance of one's findings in the broader context of the relevant disciplines is paramount to any study. In the case of this particular thesis, one of the primary goals was to identify any implications the periodic behavior of the BAM may have for regional weather forecasting. However, as the assessments of spatial robustness demonstrated, the periodic behavior appears to lack significant influence on local and regional scales. It would therefore seem that the BAM's utility as a medium- to long-range forecasting tool is quite limited. If assessed in real-time, it could perhaps serve as a useful diagnostic for the general hemispheric pattern, much like its barotropic annular mode predecessors.

Even this would serve a limited purpose, however, as the oft-mentioned periodicity associated with the BAM is really a quasi-periodicity. Despite being starkly different from the noise that dominates most geophysical time series, the frequency analyses still show significant noise and variability. In other words, the "periodic" BAM is not regular enough in its variation to constitute a reliable indicator of near-future EKE trends. At best, real-time assessment may enable those forecasting on weekly to monthly timescales to draw conclusions about broad trends – e.g., the BAM has been in its high index state for the last 8 days, so it seems likely that the next 10-15 days will see decreasing eddy activity in the hemispheric mean.

Limitations also apply to what conclusions can be drawn about the BAM's relationship with the climate system and climate change. The period of record analyzed here (36 years) is too short to be a reliable basis on which to make claims about the BAM's relationship with a changing climate, and any trends in the BAM index were minimal. As briefly alluded to in earlier chapters, it is possible that large-scale climate fluctuations (ENSO, Pacific Decadal Oscillation, Atlantic Multidecadal Oscillation, etc.) have interactions with the BAM, but once again the period of record of this study is too short to draw such conclusions. The BAM therefore appears to reside squarely in the spatiotemporal neighborhood of greatest difficulty: too long-term and large-scale to be applicable to short-term weather forecasting, but too short-term to provide insights into longer-term climate variability and change.

7.5 Potential Avenues for Future Research

As outlined in Section 1.4 of this thesis, the primary goals of this study were to determine how the BAM behaves in each hemisphere, investigate what factors affect the quasi-periodicity that emerges in the fields most strongly affected by the BAM, and explore how well represented the BAM is by both complex GCMs and a simplistic linear conversion model. Each of the seven research questions presented in the Study Objectives section were at least partially answered over the course of this thesis; however, several questions could still use further investigation and numerous new ones were raised.

Two of the most obvious ways in which this study could be expanded upon is by utilizing other datasets. Specifically, any decadal variability that may exist in the BAM could be explored by using a dataset with a longer analysis period, such as the 20th Century Reanalysis product from NOAA's Earth System Research Laboratory. Additionally, a plethora of additional GCMs are available for more in-depth analysis of model representations of the phenomenon. Highly complex modern GCMs may also be of use in dissecting the various thermodynamic processes that contribute to producing baroclinicity, thus lending insight into the factors controlling the timescale on which the BAM operates.

Parties interested in any potential operational utility of the BAM may wish to consider correlating the real-time BAM index with contemporary patterns of mid- and upper-tropospheric height and wind anomalies. Given the BAM's regional biases, particularly in the NH, it is possible that such examinations will turn up regionally robust correlations that may aid in medium- to long-range forecasting. However, as addressed previously, it is unlikely that the BAM has forecast utility on short time scales or in localized areas.

Ultimately, it is hoped that the research presented here fortifies our collective understanding of annular modes and, more generally, atmospheric dynamics. The BAM represents but one thread of many in a complicated web of modes of variability, each associated with unique patterns and implications. Little by little, this and future studies will bolster and clarify our understanding of the atmospheric extratropical circulation.

REFERENCES

Ambaum, M., B. Hoskins, and D. Stephenson, 2001: Arctic Oscillation or North Atlantic Oscillation? *J. Clim.*, **14**, 3495-3507.

Baldwin, M. P., X. Cheng, and T. J. Dunkerton, 1994: Observed correlations between winter-mean tropospheric and stratospheric circulation anomalies. *Geophys. Res. Lett.*, **21**, 1141-1144.

Baldwin, M. P., and T. J. Dunkerton, 1999: Propagation of the Arctic Oscillation from the stratosphere to the troposphere. *J. Geophys. Res.*, **104**, 30937-30946.

Baldwin, M. P., and T. J. Dunkerton, 2001: Stratospheric harbingers of anomalous weather regimes. *Science*, **294**, 581-584.

Barnes, E. A., and D. L. Hartmann, 2010a: Dynamical feedbacks and the persistence of the NAO. *J. Atmos. Sci.*, **67**, 851-865.

Barnes, E. A., and D. L. Hartmann, 2010b: Dynamical feedbacks of the southern annular mode in winter and summer. *J. Atmos. Sci.*, **67**, 2320-2330.

Barnes, E. A., N. W. Barnes, and L. M. Polvani, 2014: Delayed Southern Hemisphere climate change induced by stratospheric ozone recovery, as projected by the CMIP5 models. *J. Clim.*, **27**, 852-867.

Berbery, E. H., and C. S. Vera, 1996: Characteristics of the Southern Hemisphere winter storm track with filtered and unfiltered data. *J. Atmos. Sci.*, **53**, 468-481.

Chang, E. K. M., and I. Orlanski, 1993: On the dynamics of a storm track. *J. Atmos. Sci.*, **50**, 999-1015.

Chang, E. K. M., 1993: Downstream development of baroclinic waves as inferred from regression analysis. *J. Atmos. Sci.*, **50**, 2038-2053.

Chang, E. K. M., and D. B. Yu, 1999: Characteristics of wave packets in the upper troposphere. Part I: Northern Hemisphere winter. *J. Atmos. Sci.*, **56**, 1708-1728.

Chang, E. K. M., 1999: Characteristics of wave packets in the upper troposphere. Part II: Seasonal and hemispheric variations. *J. Atmos. Sci.*, **56**, 1729-1747.

Chang, E. K. M., 2005: The impact of wave packets propagating across Asia on Pacific cyclone development. *Mon. Wea. Rev.*, **133**, 1998-2015.

Codron, F., 2005: Relation between annular modes and the mean state: Southern Hemisphere summer. *J. Clim.*, **18**, 320-330.

Codron, F., 2007: Relations between annular modes and the mean state: Southern Hemisphere winter. *J. Atmos. Sci.*, **64**, 3328-3339.

Dee, D. P., S. M. Uppala, A. J. Simmons, P. Berrisford, P. Poli, S. Kobayashi, U. Andrae, M. A. Balmaseda, G. Balsamo, P. Bauer, P. Bechtold, A. C. M. Beljaars, L. van de Berg, J. Bidlot, N. Bormann, C. Delsol, R. Dragani, M. Fuentes, A. J. Geer, L. Haimberger, S. B. Healy, H. Hersbach, E. V. Holm, L. Isaksen, P. K ´allberg, M. Kohler, M. Matricardi, A. P. McNally, B. M. Monge-Sanz, J.-J. Morcrette, B.-K. Park, C. Peubey, P. de Rosnay, C. Tavolato, J.-N. Thepaut, F. Vitart, 2011: The ERA-Interim reanalysis: configuration and performance of the data assimilation system. *Q. J. R. Meteorol. Soc*., **137**: 553–597. DOI:10.1002/qj.828

Fischer, R. A., 1921: On the "probable error" of a coefficient of correlation deduced from a small sample. *Metron*, **1**, 3-32.

Frierson, D. M. W., I. M. Held, and P. Zurita-Gotor, 2006: A gray-radiation aquaplanet moist GCM. Part I: Static stability and eddy scale. *J. Atmos. Sci.*, **63**, 2548-2566.

Fyfe, J. C., G. J. Boer, and G. M. Flato, 1999: The Arctic and Antarctic oscillations and their projected changes under global warming. *Geophys. Res. Lett.*, **26**, 1601-1604.

Georgieva, K., B. Kirov, P. Tonev, V. Guineva, and D. Atanasov, 2007: Long-term variations in the correlation between NAO and solar activity: The importance of north-south solar activity asymmetry for atmospheric circulation. *Adv. Space Res.*, **40**, 1152-1166.

Gerber, E. P., and G. K. Vallis, 2005: A stochastic model for the spatial structure of annular patterns of variability and the North Atlantic Oscillation. *J. Clim.*, **18**, 2102-2118.

Gong, D., and S. Wang, 1999: Definition of Antarctic oscillation index. *Geophys. Res. Lett.*, **26**, 459-462.

Hall, A., and M. Visbeck, 2002: Synchronous variability in the Southern Hemisphere atmosphere, sea ice, and ocean resulting from the annular mode. *J. Clim.*, **15**, 3043-3057.

Haiden, T., M. J. Rodwell, D. S. Richardson, A. Okagaki, T. Robinson, and T. Hewson, 2012: Intercomparison of global model precipitation forecast skill in 2010/2011 using the SEEPS score. *Mon. Wea. Rev.*, **140**, 2720-2733.

Hartmann, D. L., C. R. Mechoso, and K. Yamazaki, 1984: Observations of wave-mean flow interaction in the Southern Hemisphere. *J. Atmos. Sci.*, **41**, 351-362.

Hartmann, D. L., and F. Lo, 1998: Wave-driven zonal flow vascillation in the Southern Hemisphere. *J. Atmos. Sci.*, **55**, 1303-1315.

Held, I. M., and M. J. Suarez, 1994: A proposal for the intercomparison of the dynamical cores of atmospheric general circulation models. *Bull. Amer. Meteor. Soc.*, **75**, 1825-1830.

Hendon, H. H., D. W. J. Thompson, and M. C. Wheeler, 2007: Australian rainfall and surface temperature variations associated with the Southern Hemisphere annular mode. *J. Clim.*, **20**, 2452-2467.

Hoskins, B. J., and D. J. Karoly, 1981: The steady linear response of a spherical atmosphere to thermal and orographic forcing. *J. Atmos. Sci.*, **38**, 1179-1196.

Hoskins, B. J., I. N. James, and G. H. White, 1983: The shape, propagation, and mean-flow interaction of large-scale weather systems. *J. Atmos. Sci.*, **40**, 1595-1612.

Hoskins, B. J., and P. J. Valdes, 1990: On the existence of storm-tracks. *J. Atmos. Sci.*, **47**, 1854-1864.

Hurrell, J. W., and H. van Loon, 1994: A modulation of the atmospheric annual cycle in the Southern Hemisphere. *Tellus*, **46A**, 325-338.

Hurrell, J. W., 1995: Decadal trends in the North Atlantic Oscillation: Regional temperatures and precipitation. *Science*, **269**, 676-679.

Hurrell, J. W., 1996: Influence of variations in extratropical wintertime teleconnections on Northern Hemisphere temperature. *Geophys. Res. Lett.*, **23**, 665-668.

Hurrell, J. W., Y. Kushnir, G. Ottersen, and M. Visbeck, 2003: An overview of the North Atlantic Oscillation. *Geophys. Monograph – Amer. Geophys. Union*, **134**, 1-36.

Karoly, D. J., 1990: The role of transient eddies in low-frequency zonal variations in the Southern Hemisphere circulation. *Tellus*, **42A**, 41-50.

Kidson, J. W., 1988: Interannual variations in the Southern Hemisphere circulation. *J. Clim.*, **1**, 1177-1198.

Kruger, K., B. Naujokat, and K. Labitzke, 2005: The unusual midwinter warming in the Southern Hemisphere stratosphere 2002: A comparison to Northern Hemisphere phenomena. *J. Atmos. Sci.*, **62**, 603-613.

Kutzbach, J. E., 1970: Large-scale features of monthly mean Northern Hemisphere anomaly maps of sea-level pressure. *Mon. Wea. Rev.*, **98**, 708-716.

Kwok, R., and J. C. Cosimo, 2002: Spatial patterns of variability in Antarctic surface temperature: Connections to the Southern Hemisphere annular mode and the southern oscillation. *Geophys. Res. Lett.*, **29**, doi: 10.1029/2002GL015415.

Laken, B. A., and E. Pallé, 2012: Understanding sudden changes in cloud amount: The southern annular mode and South American weather fluctuations. *J. Geophys. Res.*, **117**, D13103, DOI:10.1029/2012JD017626.

Limpasuvan, V., and D. L. Hartmann, 1999: Eddies and the annular modes of climate variability. *Geophys. Res. Lett.*, **26**, 3133-3136.

Limpasuvan, V., and D. L. Hartmann, 2000: Wave-maintained annular modes of climate variability. *J. Clim.*, **13**, 4414-4429.

Maggioni, V., M. R. P. Sapiano, and R. F. Adler, 2016: Estimating uncertainties in high-resolution satellite precipitation products: Systematic or random error? *J. Hydromet.*, **17**, 1119-1129.

Marshall, G. J., 2003: Trends in the southern annular mode from observations and reanalyses. *J. Clim.*, **16**, 4134-4143.

McGraw, M. C., and E. A. Barnes, 2016: Seasonal sensitivity of the eddy-driven jet to tropospheric heating in an idealized AGCM. *J. Clim.*, in press.

Lorenz, E. N., 1951: Seasonal and irregular variations of the Northern Hemisphere sea level pressure profile. *J. Meteor.*, **8**, 52-59.

Lorenz, E. N., 1963: The mechanics of vacillation. *J. Atmos. Sci.*, **20**, 448-464.

Lorenz, D. J., and D. L. Hartmann, 2001: Eddy-zonal flow feedback in the Southern Hemisphere. *J. Atmos. Sci.*, **58**, 3312-3327.

Namias, J., 1950: The index cycle and its role in the general circulation. *J. Meteor.*, **7**, 130-139.

North, G. R., T. L. Bell, R. F. Calahan, and F. J. Moeng, 1982: Sampling errors in the estimation of empirical orthogonal functions. *Mon. Wea. Rev.*, **110**, 699-706.

Novak, L., M. H. P. Ambaum, and R. Tailleux, 2015: The life cycle of the North Atlantic storm track. *J. Atmos. Sci.*, **72**, 821-833.

Orlanski, I., J. Katzfey, C. Menendez, and M. Marino, 1991: Simulation of an extratropical cyclone in the Southern Hemisphere: Model sensitivity. *J. Atmos. Sci.*, **48**, 2293-2311.

Orlanski, I., and J. Katzfey, 1991: The life cycle of a cyclone wave in the Southern Hemisphere. Part I: Eddy energy budget. *J. Atmos. Sci.*, **48**, 1972-1998.

Orlanski, I., and E. K. M. Chang, 1993: Ageostrophic geopotential fluxes in downstream and upstream development of baroclinic waves. *J. Atmos. Sci.*, **50**, 212-225.

Perlwitz, J., and H.-F. Graf, 1995: The statistical connection between tropospheric and stratospheric circulation of the Northern Hemisphere in winter. *J. Clim.*, **8**, 2281-2295.

Randel, W. J., and J. L. Stanford, 1985a: An observational study of medium-scale wave dynamics in the Southern Hemisphere summer. Part II: Stationary-transient wave interference. *J. Atmos. Sci.*, **42**, 1189-1197.

Randel, W. J., and J. L. Stanford, 1985b: The observed life cycle of a baroclinic instability. *J. Atmos. Sci.*, **42**, 1364-1373.

Rind, D., 2002: The sun's role in climate variations. *Science*, **296**, 673-677.

Robinson, W. A., 1991: The dynamics of the zonal index in a simple model of the atmosphere. *Tellus*, **43A**, 295-305.

Robinson, W. A., 1996: Does eddy feedback sustain variability in the zonal index? *J. Atmos. Sci.*, **53**, 3556-3569.

Rodgers, J. C., and H. van Loon, 1982: Spatial variability of sea level pressure and 500 mb height anomalies over the Southern Hemisphere. *Mon. Wea. Rev.*, **110**, 1375-1392.

Rossby, C.-G., 1939: Relations between variations in the intensity of the zonal circulation and the displacements of the semi-permanent centers of action. *J. Marine Res.*, **2**, 38-55.

Rossby, C.-G., and H. C. Willett, 1948: The circulation of the upper troposphere and lower stratosphere. *Science*, **108**, 643-652.

Simmons, A. J., and B. J. Hoskins, 1978: The life cycles of some nonlinear baroclinic waves. *J. Atmos. Sci.*, **35**, 414-432.

Simmons, A. J., and B. J. Hoskins, 1979: The downstream and upstream development of unstable baroclinic waves. *J. Atmos. Sci.*, **36**, 1239-1254.

Simmons, A. J., and B. J. Hoskins, 1980: Barotropic influences on the growth and decay of nonlinear baroclinic waves. *J. Atmos. Sci.*, **37**, 1679-1684.

Strong, C., and G. Magnusdottir, 2008: Tropospheric Rossby wave breaking and the NAO/NAM. *J. Atmos. Sci.*, **65**, 2861-2876.

Thompson, D. W. J., and J. M. Wallace, 1998: The Arctic oscillation signature in the wintertime geopotential height and temperature fields. *Geophys. Res. Lett.*, **25**, 1297-1300.

Thompson, D. W. J., and J. M. Wallace, 2000: Annular modes in the extratropical circulation. Part I: Month-to-month variability. *J. Clim.*, **13**, 1000-1016.

Thompson, D. W. J., J. M. Wallace, and G. C. Hegerl, 2000: Annular modes in the extratropical circulation. Part II: Trends. *J. Clim.*, **13**, 1018-1036.

Thompson, D. W. J., and J. M. Wallace, 2001: Regional climate impacts of the Northern Hemisphere annular mode. *Science*, **293**, 85-89.

Thompson, D. W. J., M. P. Baldwin, and J. M. Wallace, 2002: Stratospheric connection to Northern Hemisphere wintertime weather: Implications for prediction. *J. Clim.*, **15**, 1421-1428.

Thompson, D. W. J., and S. Solomon, 2002: Interpretation of recent Southern Hemisphere climate change. *Science*, **296**, 895-899.

Thompson, D. W. J., S. Lee, and M. P. Baldwin, 2003: Atmospheric processes governing the Northern Hemisphere annular mode/North Atlantic oscillation. *Geophys. Monograph—Amer. Geophys. Union*, **134**, 81-112.

Thompson, D. W. J., S. Solomon, P. J. Kushner, M. H. England, K. M. Grise, and D. J. Karoly, 2011: Signatures of the Antarctic ozone hole in Southern Hemisphere surface climate change. *Nat. Geosci.*, **4**, 741-749.

Thompson, D. W. J., and E. A. Barnes, 2014: Periodic variability in the large-scale Southern Hemispheric circulation. *Science*, **343**, 641-645.

Thompson, D. W. J., and J. D. Woodworth, 2014: Barotropic and baroclinic annular variability in the Southern Hemisphere. *J. Atmos. Sci.*, **71**, 1480-1493.

Thompson, D. W. J., and Y. Li, 2015: Baroclinic and barotropic annular variability in the Northern Hemisphere. *J. Atmos. Sci.*, **72**, 1117-1136.

Thompson, D. W. J., B. R. Crow, and E. A. Barnes, 2016: Intraseasonal periodicity in the Southern Hemisphere circulation on regional spatial scales. Submitted to *J. Atmos. Sci.*

Torrence, C., and G. P. Compo, 1998: A practical guide to wavelet analysis. *Bull. Amer. Meteor. Soc.*, **79**, 61-78.

Trenberth, K. E., 1979: Interannual variability of the 500 mb zonal mean flow in the Southern Hemisphere. *Mon. Wea. Rev.*, **107**, 1515-1524.

Trenberth, K. E., 1991: Storm tracks in the Southern Hemisphere. *J. Atmos. Sci.*, **48**, 2159-2178.

Visbeck, M., 2009: A station-based southern annular mode index from 1884 to 2005. *J. Clim.*, **22**, 940-950.

Walker, G. T. and E. W. Bliss, 1932: World weather V. *Memoirs of the R. M. S.*, **4**, 53-83.

Wallace, J. M., and D. S. Gutzler, 1981: Teleconnections in the geopotential height field during the Northern Hemisphere winter. *Mon. Wea. Rev.*, **109**, 784-812.

Wallace, J. M., 2000: North Atlantic Oscillation / annular mode: Two paradigms – one phenomenon. *Q. J. Royal Met. Soc.*, **126**, 791-805.

Wallace, J. M., and D. W. J. Thompson, 2002: The Pacific center of action of the Northern Hemisphere annular mode: Real or artifact? *J. Clim.*, **15**, 1987-1991.

Willett, H. C., 1948: Patterns of world weather changes. *Trans. Amer. Geophys. Union*, **29**, 803-809.

Woodworth, J. D., 2013: Towards understanding the processes that govern variability in the Southern Hemisphere. Thesis, Department of Atmospheric Science, Colorado State University, 125 pp.

Yu, J., and D. L. Hartmann, 1993: Zonal flow vacillation and eddy forcing in a simple GCM of the atmosphere. *J. Atmos. Sci.*, **50**, 3244-3259.